

# Ph. D. thesis

**Prepared at**

L'U.F.R. DES SCIENCES ET TECHNIQUES  
DE L'UNIVERSITÉ DE FRANCHE-COMTE

**In order to obtain the**

**GRADE DE DOCTEUR DE L'UNIVERSITÉ DE FRANCHE-COMTE**  
**Spécialité: Sciences pour l'Ingénieur**

**DEVELOPPEMENT ET CARACTERISATION DE MELANGES  
POLYMERES-POUDRES METALLIQUES POUR LE MICRO  
MOULAGE PAR INJECTION  
DEVELOPMENT AND CHARACTERIZATION OF POLYMER-  
METALLIC POWDER FEEDSTOCKS FOR MICRO-INJECTION  
MOLDING**

**by**

**Xiangji KONG**

**Defense on 7<sup>th</sup> February 2011, defense committee:**

<b>Advisor</b>	T. BARRIERE	Professor, University of Franche-Comté, Besançon
<b>Co-advisor</b>	J.-C. GELIN	Professor, ENSMM, Besançon
<b>Reviewers</b>	Y. BIENVENU	Professor, Mines ParisTech, Paris
	J.M.TORRALBA	Professor, University of Madrid, Spain
<b>Examinators</b>	F. BERNARD	Professor, University of Bourgogne, Dijon
	E. CARREÑO-MORELLI	Professor, University of Applied Sciences Western, Switzerland
	F. VALDIVIESO	HdR, Ecole Nationale Supérieure des Mines de St-Etienne
	H. BERTHIAUX	Professor, Ecole des Mines d'Albi-Carmaux



## Abstract

Micro-PIM technology is one of the key technologies to satisfy the increasing demands for smaller parts associated to miniaturization and functionalization in different application fields. The thesis focuses on the elaboration and characterization of feedstock based on 316L stainless steel powders, identification of physical material parameters associated to the sintering stage and on the numerical simulations of the sintering process.

Feedstock formulations with new binder systems composed of different polymeric binder systems have been proposed for various 316L stainless steel powders (5  $\mu\text{m}$  and 16  $\mu\text{m}$ ). Characterization of the resulting feedstocks for each group is carried out through mixing torque tests and viscosity tests. The feedstock associated to formulation with polypropylene + paraffin wax + stearic acid is well adapted for both powders and retained in the subsequent tests, due to the low mixing torque and shear viscosity. The critical powder volume loading with 316L stainless steel powder (5  $\mu\text{m}$ ) according to the retained formulation is determined at 68% using four different methods. Micro mono-material injection (with 316L stainless steel feedstock) and bi-material injection (with 316L stainless steel feedstock and Cu feedstock) are properly investigated. Homogeneity tests are performed for the feedstocks before and after injection.

A physical model well suited for sintering stage is proposed for the simulation of sintering stage. The parameters identifications of the proposed model are carried out for the sintering stages considering 316L stainless steel (5  $\mu\text{m}$ ) feedstocks with various powder volume loadings (62%, 64% and 66%). By beam-bending tests and free sintering tests through TMA in a vertical dilatometer are investigated. Three sintering stages corresponding to heating rates equal 5  $^{\circ}\text{C}/\text{min}$ , 10  $^{\circ}\text{C}/\text{min}$  and 15  $^{\circ}\text{C}/\text{min}$  are used during both beam-bending tests and free sintering tests.

On basis of the results obtained from dilatometry measurements, the shear viscosity module  $G$ , the bulk viscosity module  $K$  and the sintering stress  $\sigma_s$  are identified using Matlab<sup>®</sup> software. Afterwards, the sintering model is implemented in the Abaqus<sup>®</sup> finite element codes, the element that are used correspond to R3D4 and C3D8R for the support and the four micro-specimens, respectively. The physical material parameters resulting from the identification experiments are used to define the 316L stainless steel feedstock, together with the identified  $G$ ,  $K$  and  $\sigma_s$ . Finally, the sintering stage at 1200  $^{\circ}\text{C}$  with three heating rates (5  $^{\circ}\text{C}/\text{min}$ , 10  $^{\circ}\text{C}/\text{min}$  and 15  $^{\circ}\text{C}/\text{min}$ ) are also simulated corresponding to the four types of micro-specimen (powder volume loading of 62%, 64% and 66%). The simulated shrinkages and relative densities of the sintered micro-specimens are compared to the experimental results and the agreement is good.

**Keywords:** Micro-Metal Injection Molding, Bi-material injection, Sintering, 316L Stainless Steel, Material modeling, Numerical Simulation

<b>ABSTRACT .....</b>	<b>I</b>
<b>ACKNOWLEDGMENTS .....</b>	<b>IV</b>
<b>INTRODUCTION.....</b>	<b>1</b>
<b>CHAPTER 1. STATE OF THE ART .....</b>	<b>5</b>
1.1. POWDER METALLURGY .....	5
1.1.1. <i>Brief introduction of powder metallurgy</i> .....	5
1.1.2. <i>Powder metallurgy history</i> .....	5
1.1.3. <i>Industry of powder metallurgy</i> .....	6
1.1.4. <i>Advantages of powder metallurgy</i> .....	6
1.2. POWDER INJECTION MOULDING .....	7
1.2.1. <i>Powder injection moulding market</i> .....	8
1.2.2. <i>Raw material for metal powder injection moulding process</i> .....	10
1.3. METAL POWDER INJECTION MOLDING PROCESS .....	13
1.3.1. <i>Bi-material metal powder injection moulding process</i> .....	18
1.3.2. <i>Micro metallic powder injection moulding process</i> .....	18
1.3.3. <i>Biomedical metallic powder injection moulding process</i> .....	19
1.3.4. <i>Limitations of metal injection moulding process</i> .....	20
1.3.5. <i>Advantages of powder injection moulding process</i> .....	20
1.4. RESEARCHES IN METAL POWDER INJECTION MOULDING PROCESS .....	22
1.4.1. <i>The scientific papers and associated patents in the area of MIM</i> .....	22
1.4.2. <i>The principal research centers in MIM processing</i> .....	22
1.4.3. <i>Research centers concentrated on modeling and simulation of Metal Injection Moulding Process</i> .....	23
1.4.4. <i>Researches about MIM process in France</i> .....	23
<b>CHAPTER 2. DEVELOPMENT AND CHARACTERIZATION OF FEEDSTOCKS BASED ON FINE POWDERS WITH HIGH VOLUME FRACTION LOADING .....</b>	<b>25</b>
2.1. POWDERS, PROCESSING AND CHARACTERISTICS .....	25
2.1.1. <i>Main powders type</i> .....	25
2.1.2. <i>Powders used in the previous Ph. D. theses carried out at FEMTO-ST</i> .....	26
2.1.3. <i>Powders used in the related experiments and analyses</i> .....	26
2.2. BINDER .....	29
2.2.1. <i>The role of binder in MIM processes</i> .....	29
2.2.2. <i>Choice of a proper binder</i> .....	29
2.3. MAIN PROPERTIES OF FEEDSTOCKS .....	31
2.3.1. <i>Involved equipment to investigate the characteristics and properties of the feedstock</i> .....	31
2.4. FEEDSTOCK FORMULATION .....	35
2.5. CHOICE OF THE APPROPRIATE FEEDSTOCK FORMULATION THROUGH PHYSICAL TESTING .....	36
2.5.1. <i>Mixing Torque Tests</i> .....	36
2.5.2. <i>Viscosity Tests</i> .....	38
2.6. DETERMINATION OF CRITICAL POWDER LOADING .....	40
2.6.1. <i>Mixing tests by continuously increasing powder loading</i> .....	40
2.6.2. <i>Mixing tests by batch powder loading</i> .....	41
2.6.3. <i>Rheological tests</i> .....	42
2.6.4. <i>Feedstock viscosity model</i> .....	42
2.7. HOMOGENEITY TESTS FOR THE FEEDSTOCKS .....	45
2.8. SELECTED FEEDSTOCK FOR THE SUBSEQUENT EXPERIMENTS .....	47
SUMMARY .....	48
<b>CHAPTER 3. MICRO-MIM PROCESS FOR MINIATURIZATION AND FUNCTIONALIZATION.....</b>	<b>50</b>
3.1. EQUIPMENT USED FOR INJECTION MOLDING STAGE .....	50
3.1.1. <i>Arburg 220-S injection moulding equipment</i> .....	50
3.1.2. <i>Battenfeld Microsystem 50 injection moulding equipment</i> .....	51
3.1.3. <i>Mould design and micro machining</i> .....	52
3.2. MONO INJECTION FOR THE PHYSICAL IDENTIFICATIONS OF THE FEEDSTOCKS .....	53
3.3. MICRO INJECTION OF THE SPECIMENS USED FOR VALIDATION OF THE SIMULATIONS .....	54
3.4. HOMOGENEITY TESTS OF THE INJECTED SPECIMENS FROM MICRO INJECTION .....	55
3.5. BI-MATERIAL INJECTION MOLD WITH TWO-PLATE MOLD .....	57
3.6. BI-MATERIAL INJECTION WITH THREE-PLATE MOLD .....	59
SUMMARY .....	60



<b>CHAPTER 4. DEBINDING AND SINTERING STAGES OF MIM PROCESS FOR THE COMPONENTS OBTAINED BY BI-MATERIAL AND MICRO-INJECTION.....</b>	<b>61</b>
<b>4.1. THERMAL DEBINDING STAGE .....</b>	<b>61</b>
4.1.1. <i>Equipment used for thermal debinding stage.....</i>	<i>61</i>
4.1.2. <i>Debinding cycles and atmosphere.....</i>	<i>62</i>
<b>4.2. SINTERING STAGE BY SOLID STATE DIFFUSION .....</b>	<b>64</b>
4.2.1. <i>Equipment used for sintering stage.....</i>	<i>65</i>
4.2.2. <i>Sintering cycles for bi-material injected specimens.....</i>	<i>65</i>
4.2.3. <i>Sintering cycles for micro-injected specimens.....</i>	<i>68</i>
4.2.4. <i>Physical properties of the resulted micro-parts at the end of the processing stage.....</i>	<i>69</i>
SUMMARY .....	71
<b>CHAPTER 5. IDENTIFICATION OF CONSTITUTIVE MATERIAL PARAMETERS AND NUMERICAL SIMULATION OF THE SINTERING STAGE IN MICRO-MIM.....</b>	<b>73</b>
<b>5.1. CONSTITUTIVE SINTERING MODEL .....</b>	<b>73</b>
<b>5.2. SINTERING PARAMETERS IDENTIFICATION .....</b>	<b>77</b>
5.2.1. <i>Identification tests in vertical dilatometer .....</i>	<i>78</i>
5.2.2. <i>Numerical identification of the sintering model.....</i>	<i>84</i>
<b>5.3. FE SIMULATION OF THE SINTERING STAGE FOR THE COMPONENTS FROM MICRO-MIM WITH 316 L STAINLESS STEEL FEEDSTOCK .....</b>	<b>91</b>
5.3.1. <i>Prediction of shrinkages for micro- injected specimens with 316L stainless steel feedstock (<math>D_{50}=3.4\ \mu\text{m}</math>, formulation F3).....</i>	<i>93</i>
5.3.2. <i>Prediction of relative density for the micro-injected specimens with 316L stainless steel feedstock (<math>D_{50}=3.4\ \mu\text{m}</math>, formulation F3) .....</i>	<i>95</i>
SUMMARY .....	98
<b>CHAPTER 6. CONCLUSIONS AND PERSPECTIVES .....</b>	<b>99</b>
<b>6.1. CONCLUSIONS .....</b>	<b>99</b>
<b>6.2. PERSPECTIVES.....</b>	<b>101</b>
6.2.1. <i>Experiments and processing .....</i>	<i>101</i>
6.2.2. <i>Computational developments.....</i>	<i>101</i>
<b>APPENDIX I: SIMULATED SHRINKAGES AND COMPARISONS BETWEEN THE NUMERICAL AND EXPERIMENTAL RESULTS.....</b>	<b>102</b>
<b>APPENDIX II: SIMULATED RELATIVE DENSITY DISTRIBUTIONS.....</b>	<b>108</b>
<b>BIBLIOGRAPHY .....</b>	<b>110</b>

## Acknowledgments

I would like to express my appreciation and thanks to my thesis advisors, Professor Thierry Barriere (Université de Franche-Comté France) and Professor Jean-Claude Gelin (ENSMM, France), for their kindly advice, clear guidance and helpful assistance during the whole research course. Their rich experiences on powder injection moulding process, advanced knowledge on material forming technology and valuable notions on numerical simulation are indispensable for the progress of my dissertation, which strengthen the foundation of my professional and scientific career in the future.

Special thanks go to the reviewers Pr. Yves Bienvenu (Mines ParisTech, France) and Pr. Jose Manuel TORRALBA (University of Madrid, Spain), their valuable suggestions are incorporated in the final thesis.

I would like to appreciate Gérard Michel (ENSMM, France) and Camille Garcin (FEMTO-ST/Applied Mechanics, France) for their works on manufacturing of injection molds employed in my thesis, also for Guillaume Larsen (Ph. D. student in the research team) for the design of the bi-material injection mold. I am obligated to thank Jiupeng Song (Doctor, China) for the kindly help on the simulation with Matlab® and Abaqus®. I am thankful to Huibin Ou (ENSMM, France) for his assistance on my experimental and numerical works. Still many thanks to my colleagues in office 43H for their company: Elie Gibeau, Cédric Quinard, Cyrille Barbier, Frédéric Thiebaud, Gang Cheng, Edouard Falconnet and Belgacem Mamen.

I would like to thank the French government for the scholarship that affords my three years' study in France. Finally I especially express my great respect to my family for the continuous supports. I especially thank my girlfriend Caomeng Sun for her precious encouragement throughout the entire duration of my thesis.

## Introduction

Powder injection molding of metals (MIM) process is adapted from polymer injection molding techniques, and it has already been focused and developed for several decades. Now this process draws more and more attention due to its ability to reduce the waste of metal, increasing economic efficiency, expanding the utilization of the hard metals and refractory metals, realizing the manufacturing of intricate structure and advancing the miniaturization [1].

The MIM process consists of sequential stages [2]: mixing of metallic powders and thermoplastic binders to get the feedstock, injection of powder/binder mixtures into the mould die cavities, debinding to mostly remove the binder and finally sintering stage by solid state diffusion to densify the metallic powder particles. The resulting components exhibit proper physical and mechanical properties. Examples of the parts resulting from MIM process are related in the **Figure 1**.



**Figure 1.** Parts and components with complex shape produced from the metal injection molding process, courtesy of EPMA

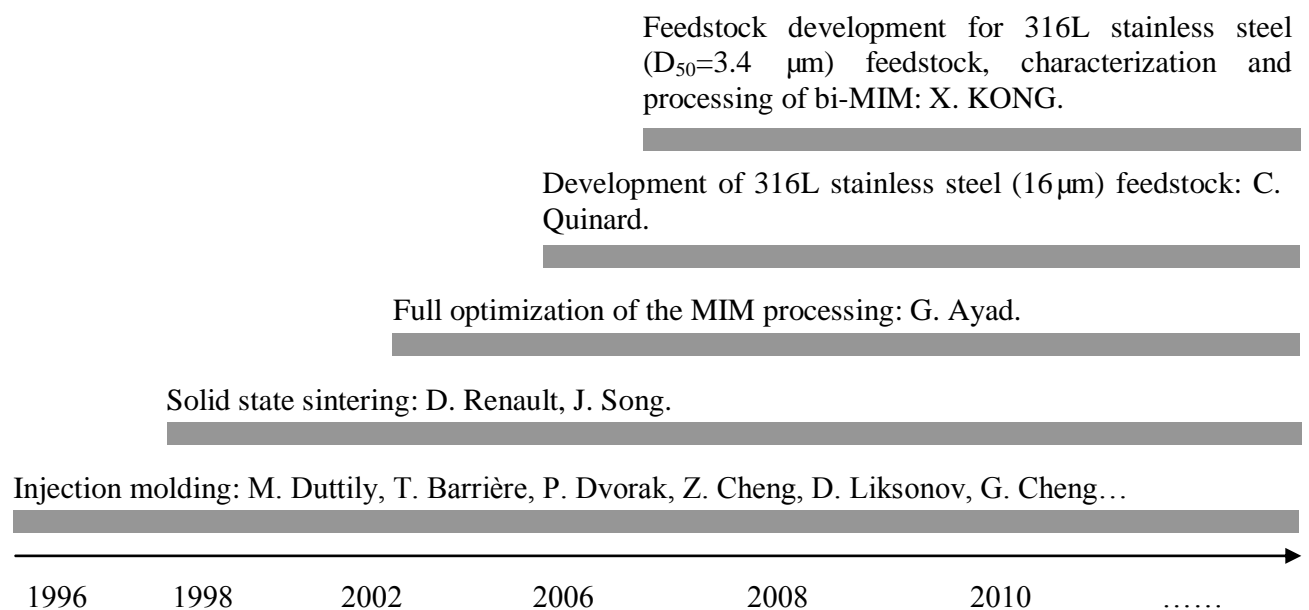
The development of the feedstock is necessary to complete the MIM process, since all the following stages should be designed and operated according to the prepared feedstock. The feedstock properties determine the injection and debinding stage in a large part. For instance, the injection parameters during the molding process, the mold design, the choice of method for the debinding stage: thermal, solvent, catalytic, supercritical, etc. As long as the feedstock is chosen and prepared, the injection stage and the debinding one can be consequently studied and established. So then the focus is shifted to the sintering stage.

The sintering stage is the key point that leads the MIM process to be successful [3]. The properties of the final components are sensitive to various factors in the sintering process. The sintering atmosphere environment, heating, holding and cooling kinetic, as well as the design of the sintering cycle, the maximum sintering temperature, the support plate to hold the component are all the elements that should taken into account to ensure the required demands from the customer, such as the shape, the final geometry and tolerance, the final density as well as the mechanical properties of the components from the MIM process.

Actually, even if this process has been industrialized for several years and if there are already hundreds of firms active in this domain, the MIM process is still a recent one, with a large variety of problems not yet resolved. In terms of feedstock, the metal powder are evolving with a tendency to decrease; the chemical composition of the powder remains to be qualified; the binder system could be deficient and its adaptability to proceed with different powder is not clear; the homogeneity of feedstock largely varies with different factors. For the sintering stage, the understanding of the densification behavior is not totally described, the determination of the size and density changes after sintering is time consuming and the cost is too high; unexpected defects also appear often during the sintering stage.

In the material processing and micro-manufacturing process managed by Professor Jean-Claude Gelin and Professor Thierry Barriere, the activities associated to PIM have concerned experiments, modeling, simulation and optimization for more than 15 years. A chronology of the Ph. D. theses processed in our laboratory in the last years is given in the **Figure 2**.

The related studies are carried out in our powder injection molding research team at the Applied Mechanics department of FEMTO-ST laboratory linked to University of Franche-Comte, ENSMM and UTBM in Besancon city. The relevant works in the same domain have been done from 1995.



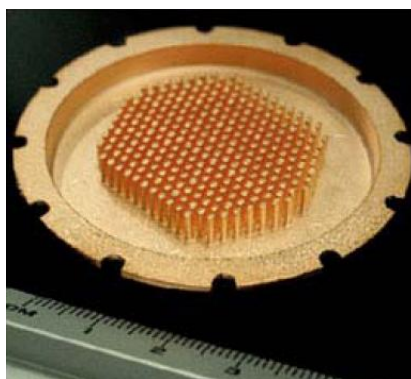
**Figure 2.** Chronology of the Ph. D. theses processed in the Powder Injection Moulding research group

Compared with the powders used in the past Ph. D. theses in the research team, the 316L stainless steel powder with  $D_{50}=3.4 \mu\text{m}$  is much finer, such micro powder satisfies the increasing demands for smaller components and miniaturization in different applications fields, such as sensors, medical devices, micro devices and so on [4] [5]. That is why very fine powders are manufactured today.

In addition, there are the rising markets for the multifunctional components composed of two parts made of different materials, as example it could be a combination of magnetic and non-magnetic parts, conductive and insulating parts or hard and soft materials in the same components [6]. However, little

work has been developed in this domain, especially in micro bi-material injection area, there are few papers in the literature in that field. The MIM process is a proper way to produce such kind of parts. In fact, our research team accumulated lot of knowledge about the bi-material injection and micro bi-material injection, including the associated mold design. However, there are some problems have not been overcome in practice, especially in the domain of micro bi-material injection molding. Thus, the main part of the proposed thesis is concentrated on that field.

To answer some of the questions mentioned above in the present MIM process, the preliminary topics of the present Ph. D. thesis are focused on the new feedstock with the fine 316L stainless steel powder ( $D_{50}=3.4\text{ }\mu\text{m}$ ) to get high powder volume fraction, the mono-injection and bi-material injection using the micro mold cavities, the modeling and numerical simulations of the sintering stage by solid state diffusion by involving the micro-components and the identified parameters. Two topics have been focused for PIM in the same time: miniaturization and multi-functionalization, a functional micro-component realized from the PIM process is related in **Figure 3**.



**Figure 3.** Example of functional micro-component, courtesy of Acelent Technologies

In the first chapter, the state of the art in the areas of powder metallurgy, powder injection molding and metal powder injection molding are introduced. In addition, the relative scientific researches are summarized for European, Asian and America regions.

In the second chapter, the development of the new feedstock based on fine stainless steel powders and fine copper powders with the binder systems composed of the different polypropylene, polyethylene, acid and wax are detailed with high powder volume content. These mixing conditions and rheological characterizations are investigated by various methods. The homogeneity of the feedstock is also examined by SEM and TGA analysis. Different methods to determine the critical powder volume fraction have been proposed and compared for fine 316L stainless steel powders.

In the third chapter, both mono-material injection and bi-material injection are tested on the basis of the elaborated feedstock from the previous steps. Several molds have been designed and manufactured in our research team and employed in the injection tests; these include the traditional injection molds and micro injection molds. Consequently, the tensile and beam-bending test specimens in specific size are

injected with high powder volume loading (i.e. 66%). Besides, the bi-material injected specimens combining the feedstock with varied powder volume loadings or with different metal powder have been realized.

In the fourth chapter, the thermal debinding and sintering stage are analyzed. The topics are the manufacturing of the sintered components to obtain the data base for the identification of the behavior laws and validate the simulation of the sintering stage. The components previously manufactured are debinded and sintered, and observations of the components after each stage are carried out, the shrinkages and the density change are related.

Meanwhile, the sintering is used to get the final parts formed of powder materials. The specimens are thermally treated at temperatures below the melting point of the main constituent to increase the strength of the parts by bonding particles together. Many ceramic materials and high temperature metals can be sintered and this process allows getting parts using a sintering temperature below their melting point depending on the materials. A powder compact before sintering is a porous packing of powders that is held together by weak surface bonds. During sintering the individual particles diffuse together to create a dense, strong monolithic part [7]. In consequence, the components may be out of the designed tolerances or, in some worse cases; they may be cracked, excessively warped or chemically incorrect with a very small density.

To avoid these defects, numerical simulations are employed to predict the process accuracy and repeatability by simulating the shape and relative density of the final component [8] in the last chapter, different identifications of the parameters employed in the sintering model are realized, through the use of these parameters in numerical simulations by the appropriate finite element software are processed in order to predict the shrinkage and relative final density for these feedstock used in the injection stage, without suffering from the repeated sintering experiments.

In conclusion chapter, the experimental and numerical results are all summarized, and the resulting different perspectives are proposed at the last part of the Ph. D. memory.

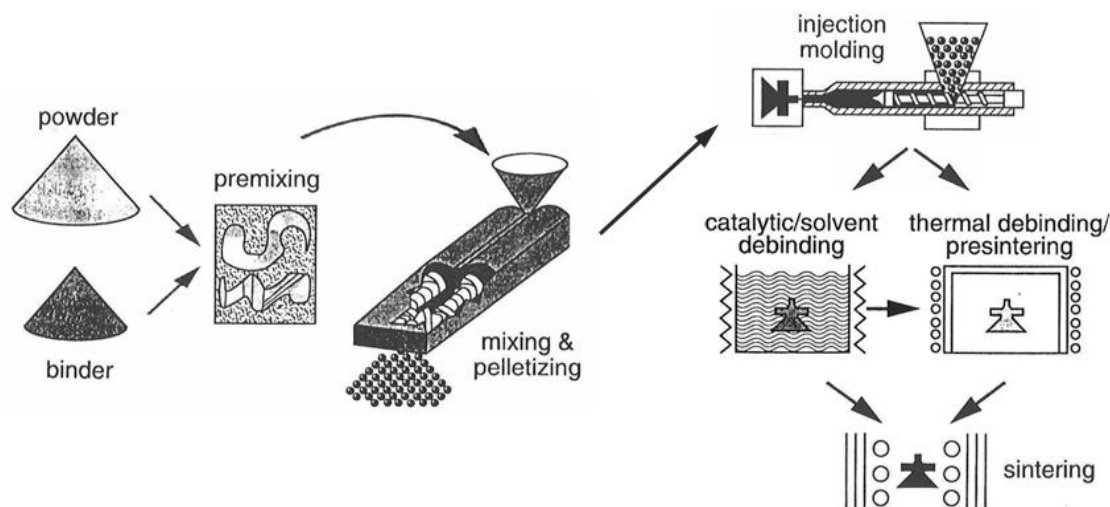
## Chapter 1. State of the art

One needs a good understanding of the evolution of the relevant technologies to know well the metal powder injection molding process, which stems from the powder metallurgy. In this chapter, the history of the powder metallurgy and the MIM process is reminded. Moreover, the latest developments in industry as well as research center concerned as well.

### 1.1. Powder metallurgy

#### 1.1.1. Brief introduction of powder metallurgy

Instead of manufacturing the metal objects by casting from molten metal or forging at softening temperatures, MIM is a more economical, more flexible and more environmentally friendly technology. Powder metallurgy process can be used to manufacture parts of simple or complex shape from a wide variety of metals and alloys in the required shape by replication of the die cavity by injection moulding under pressure, then debinding and sintering in some certain atmospheres and high temperatures to lead to a solid by coalescing the powder particles together, the production flow chart is given in **Figure 4**.




**Figure 4.** Sketch diagram of powder injection molding process [2]

#### 1.1.2. Powder metallurgy history

The history of powder metallurgy process can be traced back to 3000 B.C when the Egyptians made iron tools using this technique. In **Figure 5**, the development of powder metallurgy is recapitulated, and the origins of each period have been demonstrated as well. In the 21st century, based on the micro

powder injection molding process, the nanotechnology has been developed and will continuously increase in the new decade [9].



Date	Form	Origin
3000 AC	Iron tools	Egypt, Africa, India
1200s	Platinum pellets	Inca, South America
1878~1900	Incandescent lamp	USA
1915~1930	Carbide (die, wire drawing die, cutting tools)	Germany
1920s	Sintered oil-impregnated bearing	USA
1940s	Sintered components in steel	Central Europe
1960s	CIM- lost-wax casting	USA
1970s	HIP- steel tools- superalloys	USA
1980s	MIM- various components	USA
1990s	Nano-powder MIM in Europe	USA Europe
2000s	Micro PIM	Japan, Europe

**Figure 5.** History of the powder metallurgy

### 1.1.3. Industry of powder metallurgy

The products issued from powder metallurgy are today widely used in automotive and aerospace applications for power tools and household appliances. PM is international and related to grow industries in all of the major industrialized countries [9].

Global sales of powder metallurgy components were over (US) \$21 billion in 2006, which is expected to reach about \$23 billion in 2007 and about \$30 billion by 2012, at an average annual growth rate (AAGR) of about 5% [10].

The North American PM business was worth about \$5 billion in 2007, which is expected to increase to \$5.5 billion in 2012 [10]. The European PM market is estimated at around \$9.5 billion in 2007, which is expected to reach \$11.6 billion in 2012 [10]. The powder metallurgy market in developing Asia will show growth at around 9%; some Asian countries will see even higher growth [10].

In addition, to proceed with each stage of powder metallurgy process, certain special developed equipments are appearing. The global market for powder metallurgy equipment and tooling will be worth about \$700 million till 2012 [10].

### 1.1.4. Advantages of powder metallurgy

To explain the important prospect and the trend of rapid growth for powder metallurgy, the following advantages of this technology compared with the other process should be taken into account:

- A cost-effective processing technology;



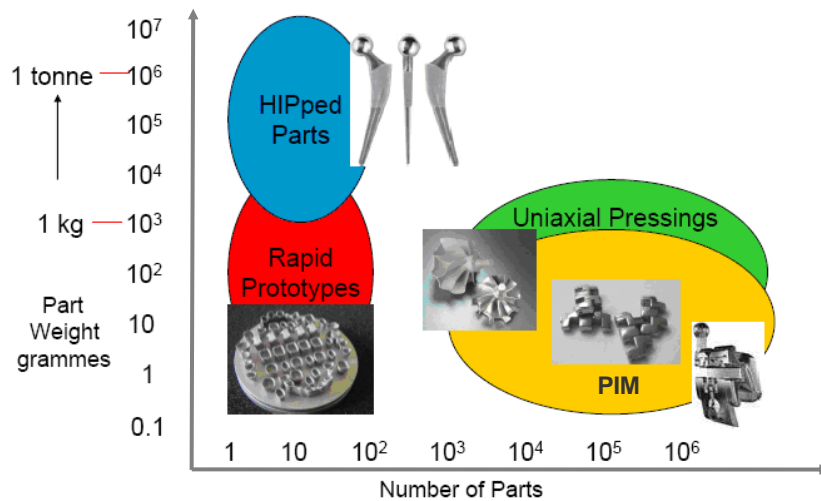
- Facilitate the manufacturing of components with irregular shapes, or eliminate machining for the one that are hard to be machined;
- Saves valuable raw materials through recycling and elimination of costly secondary machining operations through net and near-net shape design;
- Unique way to proceed with high performance and advanced particulate materials and alloys such as superalloys, tool steels, PM wrought aluminum alloys, dispersion-strengthened metals, thermally sprayed materials and intermetallics;
- On the leading edge of new manufacturing processes for improved product quality and productivity;
- Improves industrial productivity by eliminating manufacturing steps and proper adaptation to automation will be adapted to get accuracy and special properties such as self-lubrication and controlled filtration;
- Only way of processing vital metals such as tungsten carbide, dispersion-strengthened materials, high speed tool steels, superalloys and self-lubricating bearings;
- Saves natural resources through recycling and conservation of critical raw materials;
- Strategically important to complex systems such as automotive engines and transmissions, aircraft turbine engines, riding lawn mowers, surgical instruments, auto segments, electronic parts, core assets, scalpels, dilators, power tools, oil/gas well drilling equipment and off-road tractors.

## 1.2. Powder injection moulding

Based on powder metallurgy technologies, different processes have been developed, such as metallic or ceramic powder-injection molding (MIM or CIM, respectively), hot isostatic pressing (HIP), hot pressing, and hot extrusion (to name a range of processing technologies), spray forming, rapid prototyping and rapid manufacturing. Meanwhile, one ideal for producing near-net-shape components is powder-injection molding (PIM), which has the ability to process advanced metals into complex-shaped parts, just like in thermoplastic molding process [11].

PIM technology was first used in the 1930s for injection molding ceramic sheaths entering in spark plug insulators production. The process was adopted by the investment casting industry due to the better ability for manufacturing ceramic cores. This process is well devoted to achieve mass production thanks to the ability of producing complex geometries which are impossible to get with the other technologies, especially for the very small components in large batches corresponding to the case where PIM process is usually applied, as shown in **Figure 6**. However, PIM attracted little other interest until it was used for the molding of metal powders in the mid 1970s. This novel application of what was considered a

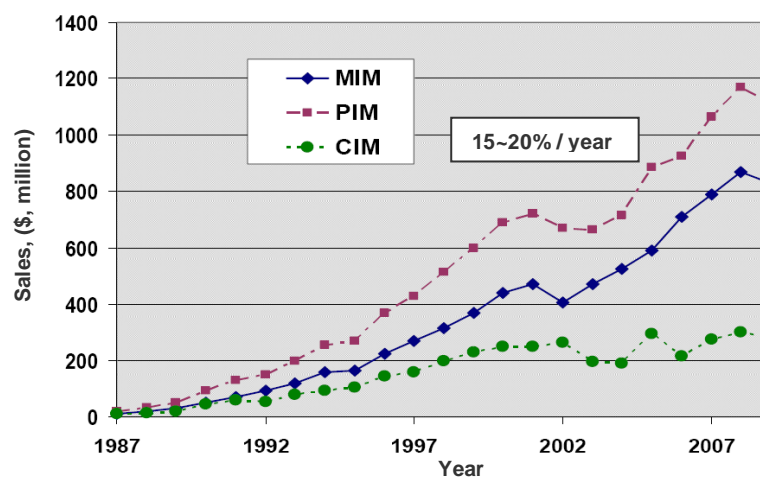
low tech process to a diverse range of particulate systems initiated considerable worldwide research in the following years. The research strengthened the science, technologies and knowledge base in PIM, and it is now recognized as a sophisticated, interdisciplinary technology [12].



**Figure 6.** Characterization of different processes in terms of production volume vs. part weight [13]

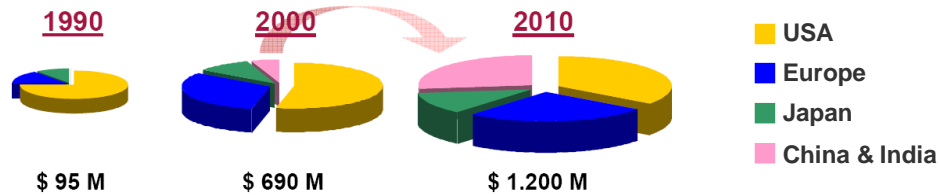
### 1.2.1. Powder injection moulding market

In comparison to metals, ceramics and carbides PIM sales in the domain of powder metallurgy are smaller and not yet closing the gap on metals. Among nearly 330 firms identified in PIM, over two-thirds report participation in MIM market. From a sales value perspective, MIM portion of PIM is over 75%. Since MIM is the dominant actor in PIM, attention was directed to understand the changes taking place in that field [14]. A general resume of the sales for PIM, MIM and CIM has been indicated in **Figure 7**.



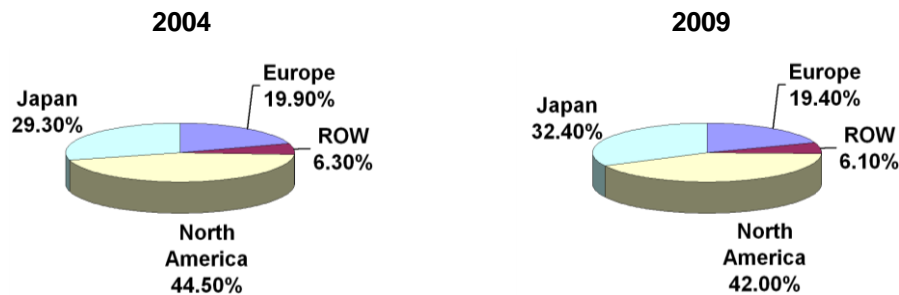
**Figure 7.** Annual sales of powder injection molding (PIM), ceramic powder injection molding (CIM) and metal powder injection molding versus calendar year till 2009

It is shown that an average rise of 15~20% per year has been presented by PIM and MIM regardless of a few years of drop. Compared with these two processes, CIM has given a relatively low growth rate. Considering the sales of the firms identified in PIM, a survey from 1990 to 2010 gives variations in **Figure 8** according to geographical origin. The number of firms has grown from about 50 to about 350. It can be clearly observed that China and India have rapidly developed in the last decades and this tendency will continue in the coming years.



**Figure 8.** Survey of the global sales of the firms according to the geographical regions (1990 to 2010)

In terms of sales from metal powder injection molding process, one report of the worldwide sale fractions of the metal powder injection molding market has been detailed by Patil Balaji [15] and related in **Figure 9**.



**Figure 9.** Worldwide sale parts of metallic powder injection molding market

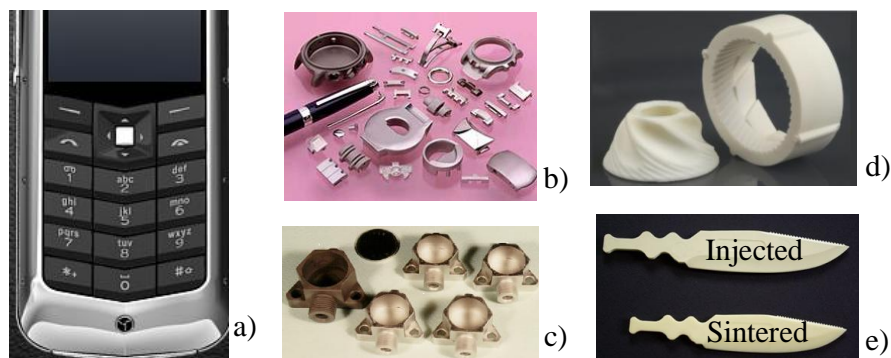
**Table 1** gives the summary of sales in the past and the forecast by 2014 of MIM components. Inside, ROW includes S. America, Australia and non-NATO Europe inc. Russia (Courtesy Sandvik Osprey/ BCC Research).

Region	USD in 2009, Million	Share in 2009,%	USD in 2014, Million	Share in 2014	CAGR 2009-14
Asia	460.8	48	959	51	15.8%
Europe	279.7	28	484	25	11.6%
N America	231	23	424	22	12.9%
ROW	13.4	1	33	2	19.8%
<b>Total</b>	<b>984.9</b>	<b>100</b>	<b>1900</b>	<b>100</b>	<b>14%</b>

The development of the different markets has been summarized in reference [17]:

The global Metal powder injection molding market will expand at an Average Annual Growth Rate (AAGR) of 8.4% from \$382 million in 2004 to healthy \$571 million in 2009. The market in Japan is the fastest growing, at an AAGR of 10.6%, and it has reached \$185 million in 2009; The U.S. market is

the largest, but will grow more slowly at an AAGR of 7.2% to \$240 million by 2009; The rest of Asia (including China) and European markets will both rise at AAGRs of 7.9% to \$35 million and \$111 million, respectively. After exceptionally high growth rates of between 10 and 15%, due to the negative influences of the economic crisis, the global 2009 MIM markets have significantly declined, however, a slight recovery is still expected for 2009~2014. Some examples of the metallic or ceramic components from the powder injection molding technology are given in **Figure 10**.



**Figure 10.** Examples from the PIM process, a) luxury mobile phone with the keypads manufactured from zirconia powder, courtesy of Alliance; b) MIM components, courtesy of Alliance; c) sensor manufactured from 316L stainless steel powder, courtesy of Rise; d) 3D wheel, courtesy of Ets Griffond and e) knife tool manufactured from alumina powder, courtesy of Ets Griffond

## 1.2.2. Raw material for metal powder injection moulding process

### 1.2.2.1. Metal powders

The most common metals available in powder form are iron and steel, tin, nickel, copper, aluminum and titanium, as well as refractory metals such as tungsten, molybdenum and tantalum [9]. The powder shipments of North America for the year of 2007 and 2008 are detailed in **Table 2**.

**Table 2.** North American Metal Powder Shipments [9]

	2007	2008
<b>Iron &amp; Steel</b>	404,650	327,272
<b>Stainless Steel</b>	9,676 (E)	7,750 (E)
<b>Copper &amp; Copper Base</b>	19,992	17,400
<b>Aluminum</b>	50,000 (E)	42,500 (E)
<b>Molybdenum</b>	2,800 (E)	2,000 (E)
<b>Tungsten</b>	4,650 (E)	4,000 (F)
<b>Tungsten Carbide</b>	7,394	5,103
<b>Nickel</b>	9,190 (E)	8,650 (E)
<b>Tin</b>	785	752
<b>(E) estimate (short tons)</b>	509,137	415.427

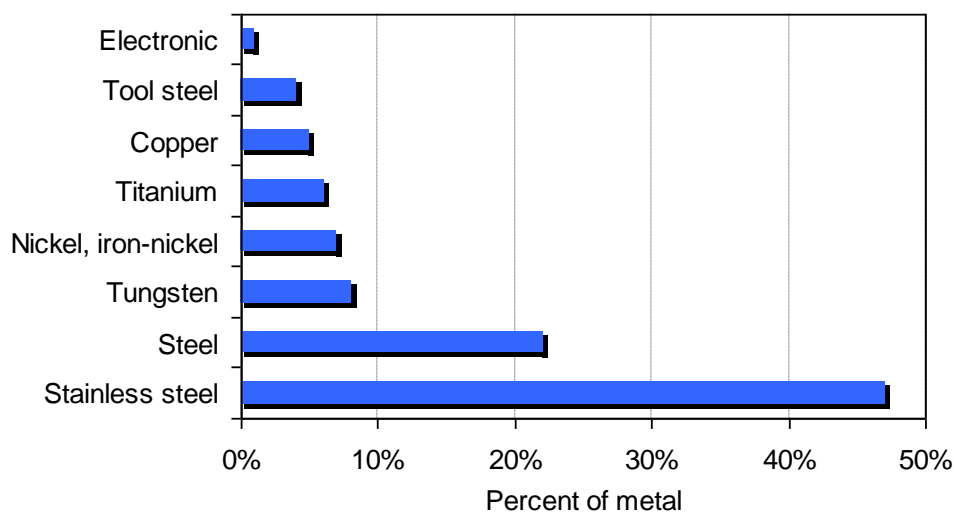
However, European shipments of metal powders for PM applications fared much better than North America, increasing by over 8% in 2006 compared with the previous year, to reach around 192,000 tons.

In Asia, Japanese shipments of metal powders for PM represented about 139,000 tons in 2006, with a similar amount in China [9]. Figure 11 shows some metal powders dedicated for MIM process.



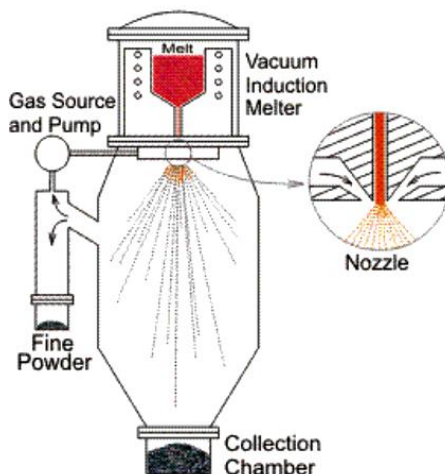
**Figure 11.** Examples of the metal powders used for MIM process [9]

In 2008, stainless powder was still the most used compared with the others metal powders in MIM industry, as shown in **Figure 12**, it had taken almost 50% of the whole powder utilization in this domain. In 2010, the same tendency has been reported by Sandvik-Osprey<sup>®</sup> from January to September. In USA, the components injected with stainless steel and steel account for 60% and 30% of the global products respectively. These steels are used in orthodontic (35%) and biomedical (30%) applications, such as chisels, cutting tools, clamps and clip applications. Besides, the application of firearms indicates 20%. The world PIM market reaches about \$ 112 billion and the European PIM medical market represents \$ 112 million (2010, data of World PM, A. Bose and R. M. German). Some new feedstock developments have been recently proposed in the market such as molybdenum [18] or 18 carat gold alloy in order to develop some new application fields [19]. Actually, there are some new developed Ti feedstocks concerning watches, surgical tools, aerospace and biomedical implants. But the corresponding sales remain from 1 to 2% of global sales and only 7% of firms proposed to sell Ti-PIM components. Otherwise, certain developments have focused on super alloy compacts as inconel 718 in order to achieve high corrosion, high oxidation resistance and high temperature strength [20].



**Figure 12.** Global relative use of metal powders in MIM process [21]

Numerous techniques which can be used to manufacture metal powders have been applied. For instance, gas atomization, water atomization, oxide reduction, fine grinding, reaction, etc. For 316L stainless steel powder, one method has been used often is gas or water atomization. The principle of gas atomization is sketched in **Figure 13**.



**Figure 13.** Gas atomization process for production of metal powders from liquid metal melts [22]

The molten material is fed into a gas expansion nozzle to form the droplets that solidify before impact with the chamber wall. The molten stream is disintegrated by rapid expansion out of the fluid nozzle. Atomization by high-pressure water is used to make rounded, prealloyed particles for PIM applications, the process is conceptually similar to gas atomization, except for the rapid quenching and differing fluid properties [23]. Gas atomization gives some advantage in contrast to the water atomization applied to the manufacturing of fine stainless steel powders, the sintered components from fine powders by gas atomization are superior to those from water atomization. The same tendencies are observed after HIP treatment [2].

#### 1.2.2.2. Binders

A primary requirement of the binder is to allow the flow of the particles into the mold die cavity, it is mandatory that the binder wets the powder surface, to aid mixing and molding, so various chemicals phenomena that modify wetting behavior are widely employed. Some important attributes of an ideal binder are reported in **Table 3**.

Based on the requirements for a binder, a simple binder design philosophy emerges. The binder usually has three components a backbone polymer that provides strength, a filler phase that is easily extracted in the first phase of debinding, and a surfactant to bridge between the binder and powder. The new tendency is to propose proper environmental friendly binder rather than to manufacture them by chemical process. For instance, Torralba et al. used polysaccharides binder to replace classical PP or PE ingredient binders [24] [25]. Some developments have been realized since some recent years with a



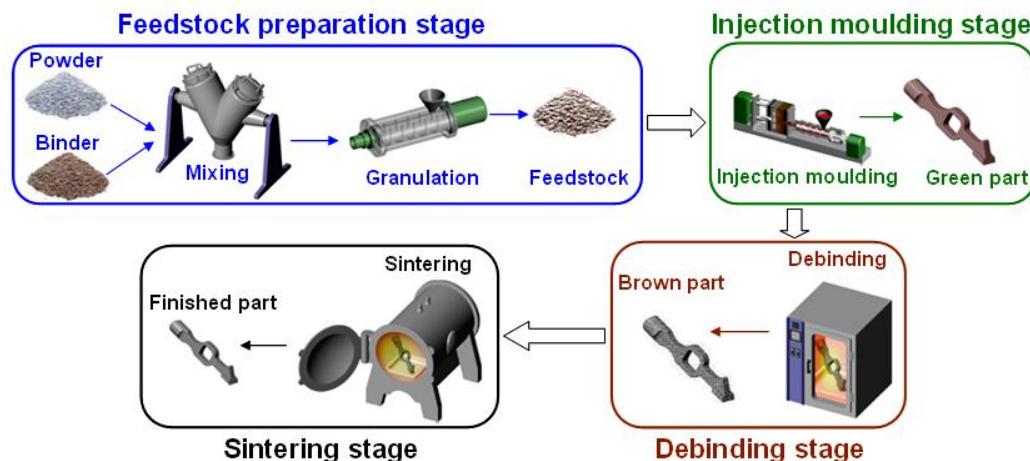
special aqueous sugar to develop large PIM components. The license is used by example by Belgium Metal SA to produce large 316L firearms.

**Table 3.** The important attributes of an ideal binder [23]

<b>Flow characteristics</b>	<ul style="list-style-type: none"> <li>· Viscosity below 10 Pa.s at the molding temperature</li> <li>· Low viscosity change of temperature during molding</li> <li>· Rapid change in viscosity during cooling</li> <li>· Strong and rigid after cooling</li> <li>· Small molecule to fit between particles and avoid orientation during flow</li> <li>· Minimum flow orientation</li> </ul>
<b>Powder interaction</b>	<ul style="list-style-type: none"> <li>· Low contact angle</li> <li>· Adherence to powder</li> <li>· Chemically passive, even under high shear and high temperature</li> <li>· Thermally stable during mixing and molding</li> </ul>
<b>Debinding</b>	<ul style="list-style-type: none"> <li>· Multiple components with differing characteristics</li> <li>· Noncorrosive, nontoxic decomposition product</li> <li>· Low ash content, low metallic content</li> <li>· Decomposition temperature above molding and mixing temperatures</li> <li>· Decomposition before sintering temperature</li> <li>· Complete removal as the powder attains structural rigidity</li> </ul>
<b>Manufacturing</b>	<ul style="list-style-type: none"> <li>· Inexpensive and available</li> <li>· Safe and environmentally acceptable</li> <li>· Long shelf life, low water absorption, no volatile components</li> <li>· Not degraded by cyclic heating (reusable)</li> <li>· High lubricity</li> <li>· High strength and stiffness</li> <li>· Low thermal expansion coefficient</li> <li>· Soluble in common solvents</li> <li>· Short chain length, no orientation</li> </ul>

### 1.3. Metal powder injection molding process

The metallic powder injection molding process is somewhat similar to plastic-injection molding as shown in **Figure 14**.



**Figure 14.** Sketch of metal powder injection molding process [26]

However, there are some additional steps in MIM: mixing the powders with an organic binder (feedstock preparation) and, then the feedstock are shaped in injection molds, then the binders are removed and finally the porous debinded components are sintered to get high density and required mechanical properties.

Meanwhile, in the first stage the ratio powder to binder is a fundamental parameter for MIM process. This ratio  $\Phi$  is often expressed on a volume percentage as in equation (1):

$$\Phi = \frac{\frac{W_p}{\rho_p}}{\frac{W_p}{\rho_p} + \frac{W_B}{\rho_B}} \quad (1)$$

but in practice the measurement of volume is much more difficult than weight, so the ratio expressed by weight should be given, the theoretical feedstock density  $\rho_M$  is given in equation (2):

$$\rho_M = \Phi \rho_p + (1 - \Phi) \rho_B \quad (2)$$

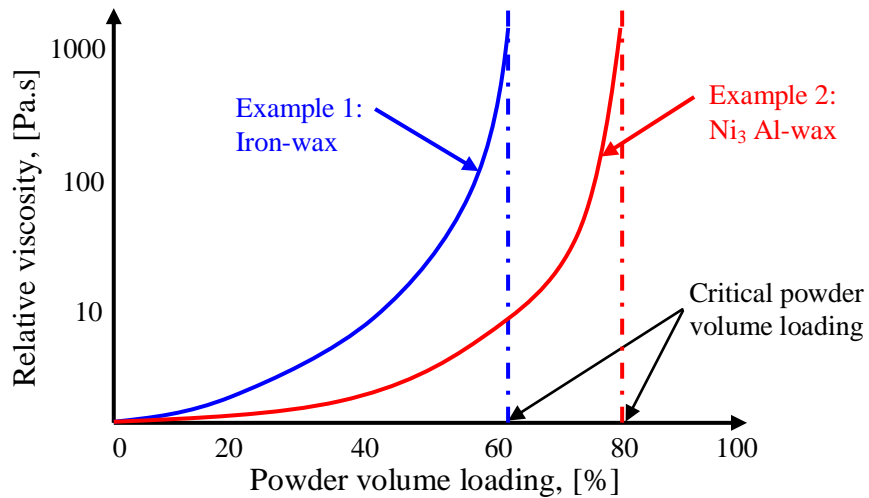
with  $\rho_p$  and  $\rho_B$  are the theoretical powder density and theoretical binder density respectively. Therefore, the weight fraction of powder  $W_p$  is expressed in equation (3):

$$W_p = \frac{\rho_p \Phi}{\rho_p \Phi + \rho_B (1 - \Phi)} \quad (3)$$

the weight fraction of binder  $W_B$  is accordingly obtained by equation (4):

$$W_B = 1 - W_p \quad (4)$$

Note that the above fractions are only used when the powder volume loading is below the critical condition (as shown in **Figure 15**, the two examples indicate different binder systems) which means there is no excess of binder in the feedstock [23].

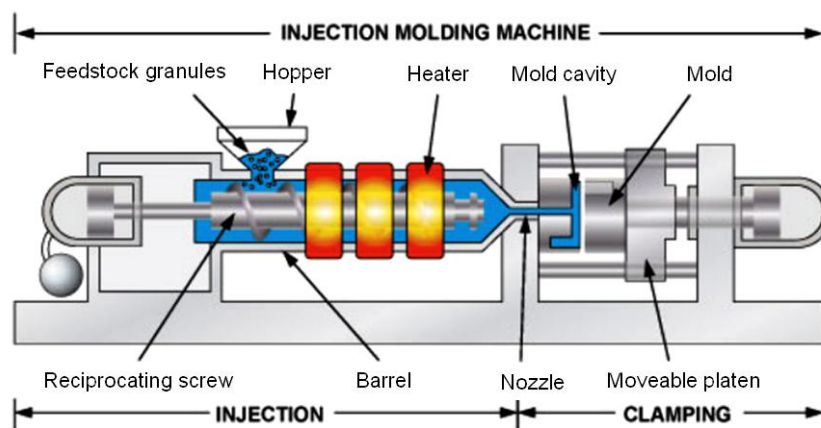


**Figure 15.** Evolution of relative viscosity vs. powder volume loading and the consequence on the fluidity



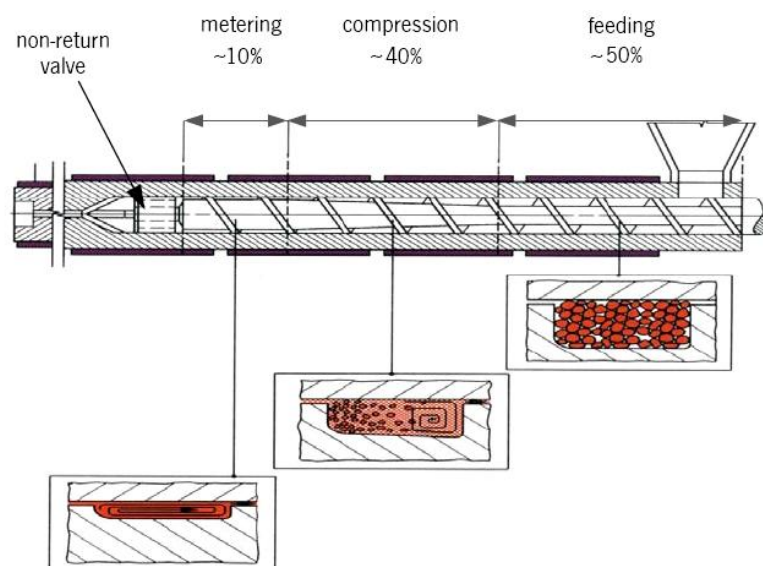
This is because the abrupt increase of viscosity appears near the critical powder loading (indicated in **Figure 15**) which may cause problems at the injection molding stage, and the powder volume loading that issued is usually slightly less than the critical value.

As shown in **Figure 16**, in the injection molding stage, the feedstock is fed into the equipment as polymer-powder granules. A screw-type plunger transports the granules through a heated barrel towards the nozzle; this plunger is used to decrease the living time in the barrel/ screw system. Along the barrel there are typically three heating zones called rear, center, and front. The front zone next to the nozzle is the hottest zone. On the way to the nozzle the feedstock granules soften and become a homogenous mass, which is forced under high pressure into the mold cavity, where it quickly cools and hardens. The mold is then opened to remove the molded part and to prepare the mold for the next cycle.



**Figure 16.** Principle sketch of the injection molding equipment [27]

Moreover, the morphology of the feedstock in the barrel is detailed in **Figure 17**.



**Figure 17.** Screw functional sections of the injection equipment during the injection stage (courtesy of Arburg) [28]

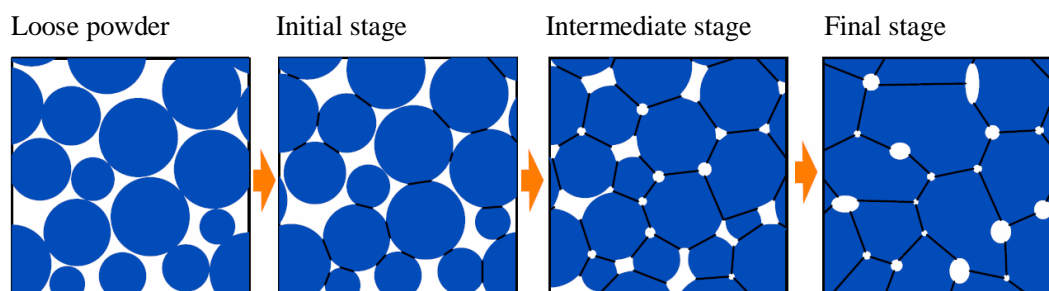
The screw acts as a mixer to ensure uniform heating during plasticizing. The screw has a check ring behind the tip that acts as a non-return valve that allows feedstock flow into the front of the cylinder during plasticizing and seals against a seat ring on the screw during mould filling and force flow through the cylinder nozzle [29].

Typical set of parameters is given in the **Table 4** [23]. The parameters of injection stage are linked to feedstock, injection moulding equipment and mold cavities.

**Table 4.** Typical molding parameters

<b>Barrel temperature, °C</b>	100 to 200
<b>Nozzle temperature, °C</b>	80 to 200
<b>Mold temperature, °C</b>	20 to 100
<b>Screw rotation speed, rpm</b>	35 to 70
<b>Injection pressure, MPa</b>	0.1 to 130
<b>Packing pressure, MPa</b>	0 to 10
<b>Fill time, s</b>	0.2 to 3
<b>Packing time, s</b>	2 to 60
<b>Cooling time, s</b>	18 to 45
<b>Cycle time, s</b>	8 to 360

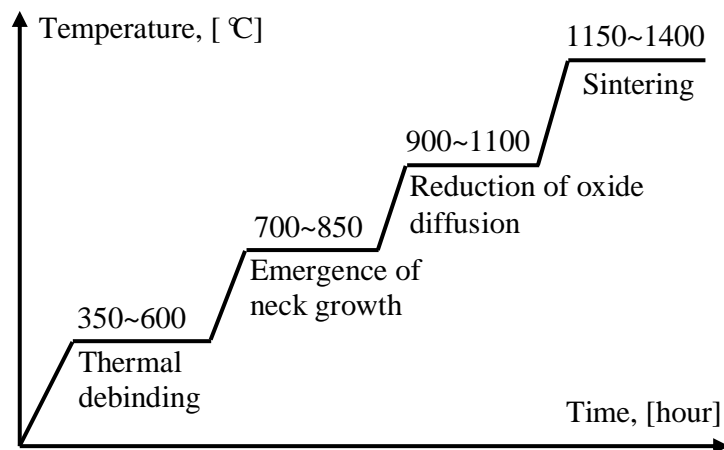
The debinding stage consists in removing a large part of the binder from the molded component in the shortest time possible by employing solvent, catalyst, thermal or other techniques, in keeping the debinding influence on the component as low as possible [30]. This process is a complex combination of chemical and physical degradation of the binders under thermal conditions. At present, different debinding techniques have been developed categorized as solvent and thermal process. In the solvent debinding process, the injected components are placed in a solvent fluid or vapor to dissolve the binders. The other debinding technique is thermal debinding consisting in removing the binders by heating the compacts. Meanwhile, the thermal debinding is time-consuming. Actually, lots of researches have been carried out concerning the supercritical debinding method to decrease debinding time and then to obtain the homogenous structure [23]. During the supercritical debinding, the binders are dissolved into the fluid by heat and pressure applied on the components. In the catalytic debinding, the compacts are heated in atmosphere containing catalyst to sweep away the polymers that are contained inside [23]. The different stages during the sintering process are sketched in **Figure 18** [23]. The debinded components are sintered by solid state diffusion.



**Figure 18.** Illustration of the microstructure evolution during the solid state diffusion sintering stage

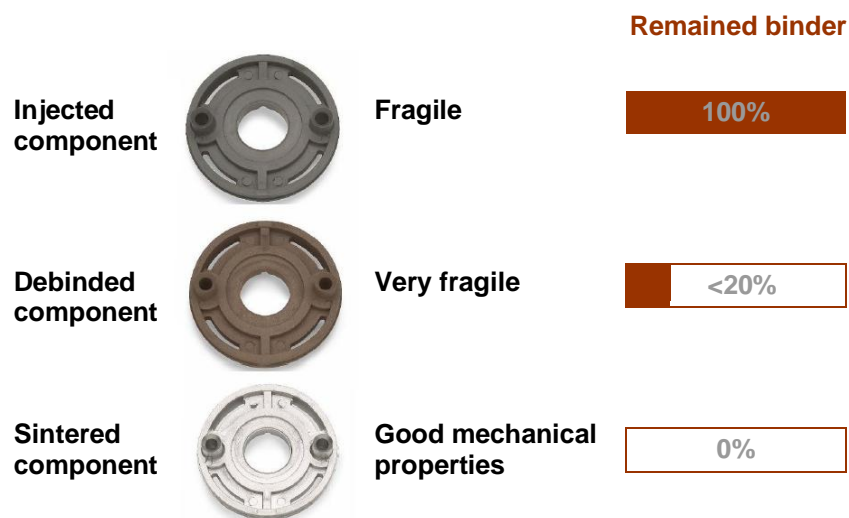
Three main kinds of diffusion can occur to form the necks between the neighbor particles: volume diffusion, grain boundary diffusion and surface diffusion. Many factors influence the sintering cycle, the determination of the kinetic cycle vary according to different feedstocks, component size and shape, sintering atmosphere, etc.

A typical sintering cycle by solid state diffusion for stainless steel feedstock is given in **Figure 19**, which is composed by four main steps: thermal debinding, emergence of neck growth, reduction of oxide diffusion and sintering. Meantime, the thermal debinding step can be carried out separately in another oven.



**Figure 19.** Typical (solid state diffusion) kinetic sintering cycle for stainless steel feedstock with four segments

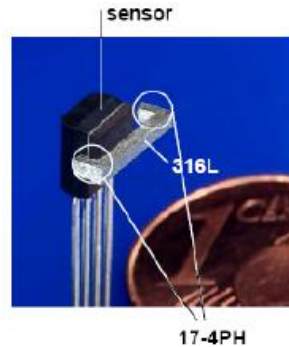
The components after such sintering stage reveal high relative density about 98%, which ensure the proper mechanical characteristics and corrosion properties. A shrinkage about 10~20% is obtained corresponding to the binder and porosity elimination as shown in **Figure 20**.



**Figure 20.** Remained binder in the component from different stages of the MIM process

### 1.3.1. Bi-material metal powder injection moulding process

Beyond single micro components or micro-structure, a micro system is usually obtained by assembling several components elaborated with different materials for special functionality or properties as shown in **Figure 21**.

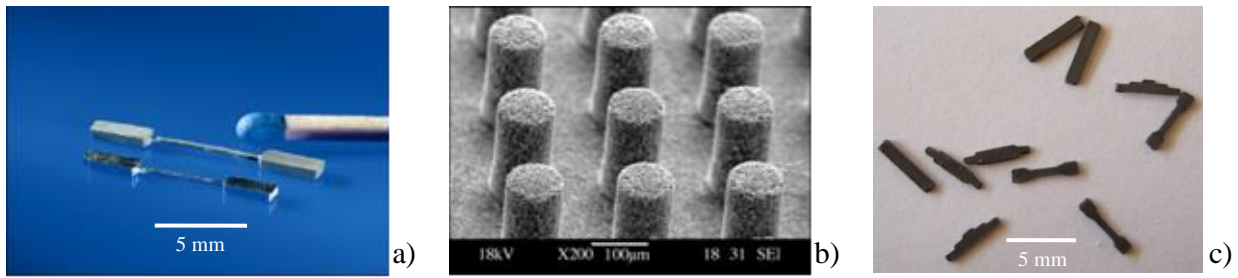


**Figure 21.** Component composed of 316L and 17-4PH manufactured by the MIM process [31]

In practice such approach is not successful due to the difficulty of bonding properly together the components of different material by forming a microstructure. However, there is still demand for parts that contain two segments made of materials with different properties. The requirements for such objects could be magnetic properties in one area of the object and non-magnetic properties in another part of the object. Other properties to be altered could be thermal conductivity and electrical conductivity, Young's modulus, hardness, reflectivity and so on [32]. Bi-injection equipment differs from general injection molding equipment mainly in the injection unit element and movable mold plate design. Firstly, bi-injection equipment has two independent injection units, much more deployments of two injection units for bi-injection (such as horizontal parallel, horizontal Y uni-direction, horizontal L type, vertical L and vertical Y, even in horizontal parallel contra-direction arrangement for two plates clamping structure) have been used than for general injection; secondly, as to movable mold plate design, a rotating mechanism for bi-injection moulding [33] whose reciprocal rotating function to allow cycling alternate motion.

### 1.3.2. Micro metallic powder injection moulding process

The global trend towards miniaturization demands manufacturing processes suitable for both micro devices and economic cost. Generally, the parts from micro metallic powder injection moulding process (micro-MIM) have sizes of several micrometers up to millimeters with three-dimensional microstructures located on one or more surface areas [34]. One promising process for the replication of metallic microstructures is micro-MIM that has reached an industrially state. Several micro components for different applications are shown in **Figure 22**.



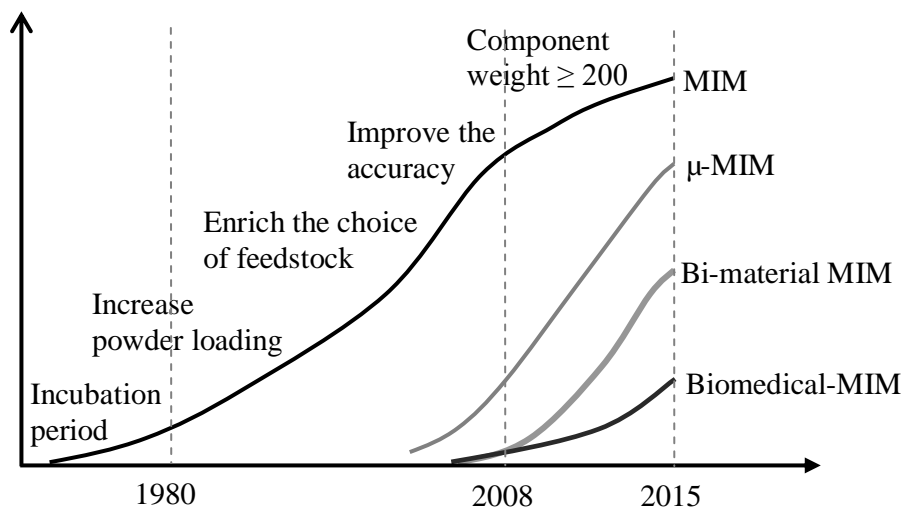
**Figure 22.** Examples of component from micro metal powder injection moulding process, a) micro-component [35]; b) plate with micro-structure [36]; c) Micro specimens manufactured FEMTO-ST

Compared with the standard MIM process widely used in industry, some process specialties have to be considered for micro-MIM. These include powder particle size, which is significantly reduced in contrast to standard MIM, and binder composition, which needs to be adjusted for safe ejection of small structures. Due to these variations, debinding and sintering routes also have to be adjusted accordingly [31]. For example, the surface finish of injection molded metallic micro-component ( $R_{\max}=8 \mu\text{m}$ ) is worse than its counterpart made from polymers ( $R_{\max}=100 \text{ nm}$ ) or ceramics ( $R_{\max}=2 \mu\text{m}$ ) [34]. It specially concerns micro-MIM where proper surface finishing is required [37].

Furthermore, special equipments have been manufactured for micro-injection stage. However, the most important strength of micro MIM lies in the great economic efficiency realized when producing medium and large series. A crucial advantage of the process is that its near-net-shape capability means that very few finishing work is required.

### 1.3.3. Biomedical metallic powder injection moulding process

From 2005, three new MIM processes have been introduced in laboratory. Meanwhile, micro injection molding and bi-material injection molding have been introduced above. The third one is biomedical-MIM. **Figure 23** gives a general view of the development of the MIM process.



**Figure 23.** General view of the evolution of MIM process

Powder Injection Moulding is an established process for manufacturing of medical products from biocompatible materials. Processing innovations have, however, enabled a wider range of functional products to be considered than ever before [38].

Biomaterials must simultaneously satisfy many requirements and exhibits properties such as non-toxicity, corrosion resistant, thermal conductivity, strength, fatigue durability, biocompatibility and sometimes aesthetics [39]. Actually, some micro-components with Ti feedstock have been injected [40], in parallel, some tests about the biocompatibility are also under examination for the components from biomedical-MIM in order to verify its ability to be implanted into the body. As example, the studies with different cell growth have been realized by Imgrund et al. for steel implant or micro functional injected surface [41].

#### **1.3.4. Limitations of metal injection moulding process**

As it is known, the main disadvantages of MIM process are listed below [23]:

- Size – The proper part size is typically limited to less than 200 grams due to the cost of the fine metal powders in comparison to classical commercial feedstocks used for MIM parts;
- Section Thickness – The maximum section thickness is generally kept to less than 6.25 mm to be able to effectively remove the thermoplastic binder from the part without damage, as well as to control distortion during sintering;
- Tolerances – Typically +/- 0.3 percent, less to +/- 0.001 mm for very small dimensions [42]. Tighter tolerances require secondary machining or grinding operations. The tolerances and surface roughness in the case of 316L stainless steel decrease when the powder particle size, with a very fine size powder ( $D_{50}=4\text{ }\mu\text{m}$ ), the surface roughness about  $R_a=0.4\text{ }\mu\text{m}$  has been obtained compared with  $1.6\text{ }\mu\text{m}$  for  $D_{50}=12\text{ }\mu\text{m}$ ;

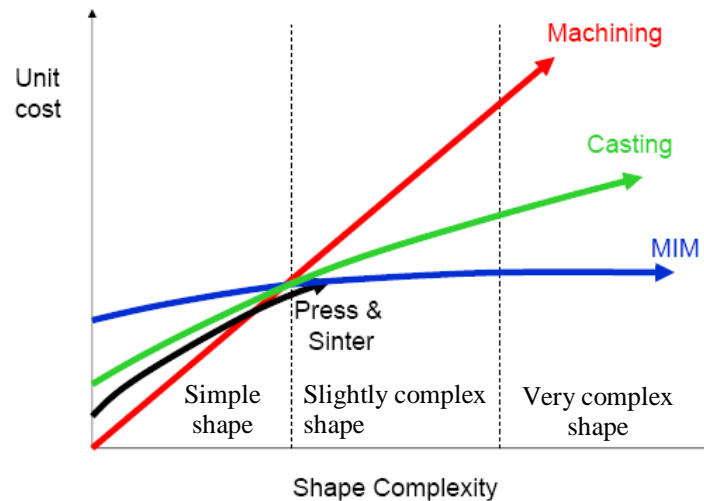
Even though MIM process has these limitations, it has been rapidly developed and applied for more and more parts, related to the advantages mentioned before.

#### **1.3.5. Advantages of powder injection moulding process**

Metal injection moulding has to be considered since the initial design stage for parts and assembly [23]:

- Parts design - MIM offers design flexibility similar to plastic injection molding. Geometrically complex parts that cannot be processed by using the conventional metallic powder processes without secondary machining operations are possible using MIM process.

- Enhanced Details - MIM provides possibilities for intricate features such as dovetails, slots, undercuts, threads, and complex curved surfaces. MIM can produce cylindrical parts with greater length-to-diameter ratios. And all of these advantages are accompanied with the lower unit cost. A comparison of the unit cost from some different processes has been illustrated in Figure 24.



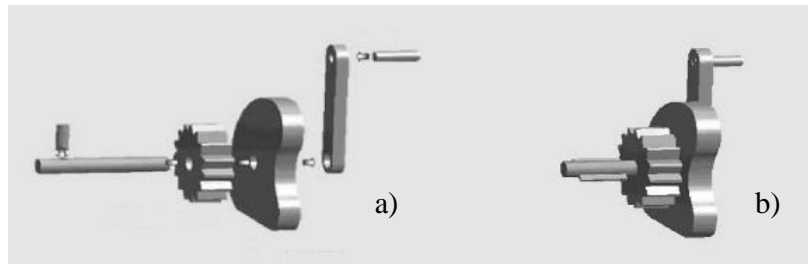
**Figure 24.** Component cost from different processes vs. the shape complexity [13]

- Improved Properties - MIM parts are typically 95% to 98% dense (vary from different materials), approaching wrought material properties. MIM parts achieve greater strength compared with conventional powder metallurgy processes.
- Reduced Waste/Machining - MIM's capability to provide net shape components eliminates many secondary machining operations. An example is given in Figure 25, Alliance<sup>®</sup> has produced a complex shaped backing case for a luxury watch [43], the 24 individual blades and the support has been firstly injected, then all the injected blades have been assembled onto the support, after debinding, the sinter-joining has been carried out during the sintering stage, proper tolerances and join quality have been achieved (see **Figure 25 c**)).



**Figure 25.** Production process for the aerospace turbine engine themed watch case realized by Alliance<sup>®</sup> (courtesy of EPMA), a) injected individual blade and support; b) 24 injected blades and injected support and c) sintered component

- Reduced Assemblies – MIM process can be used to combine two or more simpler shapes into a single, more complex component to minimize assembly costs, as shown in **Figure 26**.



**Figure 26.** Capability of reducing assemblies of MIM process, a) conventional process with 4 manufacturing processes and assembly, b) MIM process with one near-net shape molding [44]

## 1.4. Researches in metal powder injection moulding process

### 1.4.1. The scientific papers and associated patents in the area of MIM

Before 1970, there were only 10 papers related to MIM process, and even more generally in the domain of PIM, then the number increased to 100 in 1980 and more than 1000 scientific articles were published at the end of 1999 [45]. In the later 8 years, 3120 papers have been issued of which 1810 were about MIM process. Till 2007, the number of the related scientific papers raised twice [46]. Up to now, there are some journals which have been widely distributed, such as Powder Metallurgy, Powder Injection Moulding International, International Journal of Powder Metallurgy, Journal of the American Ceramic Society, and Journal of the European Ceramic Society etc. Besides, 400 patents have been registered in the USA from 1990s [46].

### 1.4.2. The principal research centers in MIM processing

In America, Pr. R.M. German research team has focused on the MIM process for long time [23] [47] [48]. In Europe, some centers focus on the micro-manufacturing, such as University of Cranfield (Dr. J. Alock [49]), University of Delft (Dr. L. Kowalski [50] [51] [52]). In Switzerland, the application of NiTi shape memory materials has been studied with powder injection moulding process (Pr. Efraín Carreño-Morelli [53]). In Germany, several technical research centers concentrate on the elaboration of components by MIM process, they are Fraunhofer (FhG-IFAM: Dr. Fr. Petzoldt [54]; FhG-IWM: Dr. T. Kraft [55] [56]) and KIT Karlsruhe (Dr. V. Pötter, R. Ruprecht [57]). In United Kingdom, there are the MIM researches at Brunel university and especially in Pr. M.J. Edirisinghe team related to the elaboration of the large ceramic components [58]. Some research centers focus on only one single stage of MIM process, as example the characterization of feedstock and its components at Chalmers university (Pr. L. Nyborg [59]), the modeling of debinding and sintering at Catholic University of Leuven (Pr L. Froyen [60], Pr. Van der Biest O. [61]) and at MTM department of the university of KUL



(Pr. Angermann H.H). In Spain, two research groups are developing some new feedstocks, especially for M2 HSS (High Speed Steel) in University of Castilla La Mancha, large activities in PIM are also developed by JM Torralba team (university of Madrid, Carlos III) [62]. As example, some new feedstocks have been developed with different 316L stainless steel powders, varying powder particle contents and shapes. T Vieira has developed special coating method to ameliorate the fluidity of the feedstock (at Coimbra university) [63] in Portugal. In Austria, a set of modern equipments has been set to build a large center in MIM fields regrouping a lot of equipment providers. In Japan, several types of very fine powders dedicated to micro-MIM or the other nanotechnologies applications have been developed. As example, iron, stainless steel, zircon, nickel and so on, have been used to develop proper feedstocks and processes for large varieties of applications [36] [64] [65]. In Korea, the development of MIM process with the titanium, copper, tungsten powders and several alloys have been developed through collaborations with the research centers in USA [66] [67] [68].

### **1.4.3. Research centers concentrated on modeling and simulation of Metal Injection**

#### **Moulding Process**

At present, the proposed commercial software to simulate MIM process is Moldflow<sup>®</sup> and moldex 3D<sup>®</sup> which is dedicated to the simulation of the injection molding stage in 2D or 3D [69]. But the interaction of the binder and powder particles cannot be investigated clearly. In addition, there is not yet the particular software for the other stages of MIM process. Professor Hetu [70] and his colleagues at IMI in Canada and Professor J.C. Gelin and his colleagues in our laboratory have developed modeling methodologies and software tools. The first team model and simulate the filling of mold cavity by using a viscous law [71]. The second team has used a biphasic approach. The COMSOL<sup>®</sup> software package has been used in the simulation of micro or nano injection moulding processes. ABAQUS<sup>®</sup> has also been employed in our team to perform the numerical simulation of the sintering stage. These analyses have been firstly carried out for the conventional MIM process with the medium size powders [72], and then these similar tests have been done in the micro-injection molding process with the fine powder (316L stainless steel powder,  $D_{50}=3.4 \mu\text{m}$ ) as related in the thesis, the involved components are about 5 mm in the length direction and 0.5 mm in thickness.

#### **1.4.4. Researches about MIM process in France**

In France, the researches related to MIM process have been carried out since 1985; meanwhile, the moulding stage (Arnaud Poitou [73]), the debinding one (Agnès Manguin [74]) and segregation analyses (Béatrice Lantéri [75]) related to this process have been studied at Ecole des Mines de Paris.

Since five years, an increasing number of laboratories are involved in PIM activities. As the ECAM laboratory that develops a feedstock with biodegradable polymer for biomedical applications. Some studies have been also done about the spark plasma sintering (SPS) by Pr. Frédéric BERNARD [76] for Ni powder. Especially, in FCE (Fonctionnalisation et Chimie pour les Microsystèmes) there are some BioPIM projects supervised by CEA LITEN (Grenoble, France). In Charleville-Mézières, a platform has been developed for pre-industrialization PIM production. Since one year, POUDR'INNOV platform starts activities with large investments in Rhône-Alpes, in order to diffuse and promote PIM opportunities. Since two years, almost twenty partners from industries and research centers are participating to GFPIM group in order to promote PIM potentialities for industries. In our laboratory FEMTO-ST/Applied Mechanics, the research team on micro processing and loaded polymers processing has developed researches on PIM since 1995 [77] [78]. The conventional MIM and PIM have been carried out using various metallic or ceramic powders and powder particles. Moreover, the micro-MIM and bi-material MIM have been investigated as well. Concerning the simulation of PIM, the FeaPIM<sup>®</sup> software has been adopted a bi-phasic model to predict the segregation of powder particles during the mould cavities filling [79]. In the same research group, studies have also been developed concerning solid state sintering, based on extensive experiments, identifications, modeling and simulations [72].

## **Chapter 2. Development and characterization of feedstocks based on fine powders with high volume fraction loading**

The content of this chapter is related to the development of new feedstocks based on the fine 316L stainless steel powders, in order to optimize the powder loading content through different methods. The same methodology has been adapted to copper feedstock. The final objective is the injection of micro components with bi-material that are investigated both from experiments and simulations.

All the subsequent processing stages are significantly affected by the feedstock characterization, in other words, the feedstock attributes have a definitive effect to one MIM process, therefore, the preparation and the characterization of the feedstock should be properly investigated and seriously controlled [23], so different experiments have been set up and carried out to characterize the developed feedstocks.

### **2.1. Powders, processing and characteristics**

So far, different elaboration techniques have been developed and applied in PIM processing to process metallic and ceramic powders, as example, gas atomization, water atomization, oxide reduction, precipitation, milling and so on. The resulting powders from different techniques exhibit different characteristics due to the different procedures related to each technique, for instance, gas atomization provide generally spherical powder shapes, while the morphology of the powders resulting from water atomization is rounded or shows ligaments, however, the cost of water atomization compared with gas atomization is smaller. The resulted particle sizes are also in different ranges.

#### **2.1.1. Main powders type**

As final components resulting from MIM process are formed by the powders contained in the feedstock, thus, it is important to characterize the powder. To describe the powder, certain aspects should be taken into account as related following: 1) particle size and its distribution, 2) particle shape, 3) specific surface, 4) interparticle friction as measured by packing and flow characterization tests [23]. It is necessary to select a proper powder for MIM process, since there are lots of factors to account, so a balance between these factors should be reached. In general, the chosen powder should be able to facilitate molding, raising the powder loading in feedstock; the powder should also limit the distortion during debinding, and offer the possibility to carefully control the sintering stage.

### 2.1.2. Powders used in the previous Ph. D. theses carried out at FEMTO-ST

A summary of the feedstocks developed in FEMTO-ST from 2002 to 2005 are related in **Table 5**, the powders and equipments are detailed as well.

<b>Table 5.</b> The feedstocks developed during the Ph. D. and the employed equipment in our laboratory				
<b>Powder</b>	<b>316L stainless steel</b>		<b>Fe</b>	<b>FeNi (8%)</b>
<b>Particle size</b>	16 $\mu\text{m}$	5 $\mu\text{m}$	30 $\mu\text{m}$	30 $\mu\text{m}$
<b>Powder volume loading (max.)</b>	62%	62%	58%	62%
<b>Powder volume loading of feedstock used for injection, debinding and sintering stage</b>	60%	60%	58%	60%
<b>Equipment for preparation of feedstock</b>	Z blades (FEMTO-ST) Twin-screw mixer (FEMTO-ST) Twin-screw extruder (Germany)		Twin-screw mixer (FEMTO-ST)	

For the two feedstocks based on 316L stainless steel, the maximum powder volume loading reached to 62%, but for the injection, debinding and sintering stage, only the feedstocks loaded at 60% (in volume) was employed in the early Ph. D. theses.

### 2.1.3. Powders used in the related experiments and analyses

As mentioned above, the feedstocks based on the same 316L stainless steel for different powder loading are related in the present study.

#### 2.1.3.1. 316L stainless steel powder

During the last recent years, 316L stainless steel powders are the most common one employed in injection molded alloys, either gas atomized or water atomized. The fact that these powders are largely used results from their capabilities to be sintered to high density and the material's corrosion resistance [80], so numbers of investigations concerning MIM process have been focused on 316L stainless steel powders. Imbaby et al. have studied the manufacturing of micro-parts by soft lithography and powder metallurgy with 316L stainless steel powder of 1.8  $\mu\text{m}$  ( $D_{50}$ ) size [81]. The involved powder volume loading is about 62%. Liu et al. [36] have carried out different analyses consisting to mix and characterize micro-powder injection molding with 316L stainless steel feedstock, composed of powder particles with size equal 2.37  $\mu\text{m}$  ( $D_{50}$ ). During last decade, important research works have been carried out at FEMTO-ST. Gelin, Barriere et al. used a commercial feedstock provided by Advanced Metalworking Practices (Advamet<sup>®</sup>) composed of 316L stainless steel powders that has been used for various injection and sintering tests [79]. Afterwards, Quinard et al. have investigated the development

and identification of 316L stainless steel feedstock with mean powder particles size equals  $5\text{ }\mu\text{m}$  and  $16\text{ }\mu\text{m}$  ( $D_{50}$ ) [82]. In reference [75], 316L stainless steel powder ( $D_{50}=3.4\text{ }\mu\text{m}$ ) provided by Osprey<sup>®</sup> with spherical particle shapes has been studied to prepare new feedstock with the objective to increase the powder volume loading and by consequence to reduce shrinkage during the sintering stage. **Table 6** gives the powder size distribution and the chemical composition.

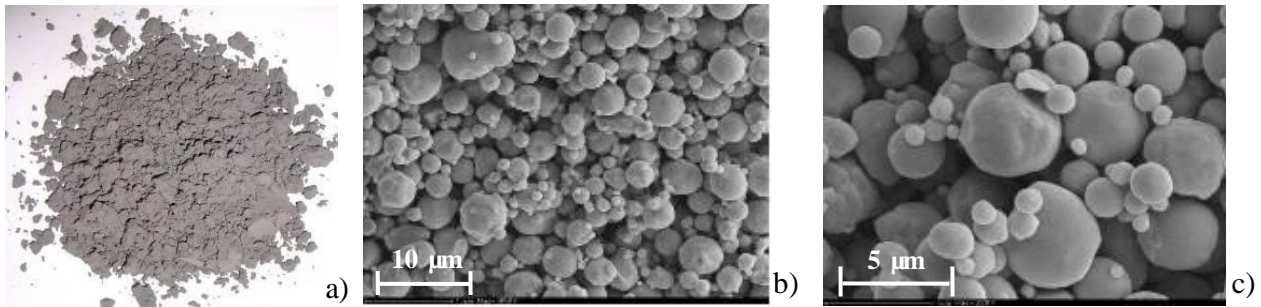
**Table 6.** Characterization of 316 L stainless steel powders used in the related investigations

Powder size and density					
Powder	Size	$D_{10}$	$D_{50}$	$D_{90}$	Density
316L Low Ni - Osprey	$5\text{ }\mu\text{m}$	$1.8\text{ }\mu\text{m}$	$3.4\text{ }\mu\text{m}$	$6.0\text{ }\mu\text{m}$	$7.9\text{ g.cm}^{-3}$
316L Low Ni - Osprey	$16\text{ }\mu\text{m}$	$4.1\text{ }\mu\text{m}$	$10.5\text{ }\mu\text{m}$	$21.9\text{ }\mu\text{m}$	$7.9\text{ g.cm}^{-3}$

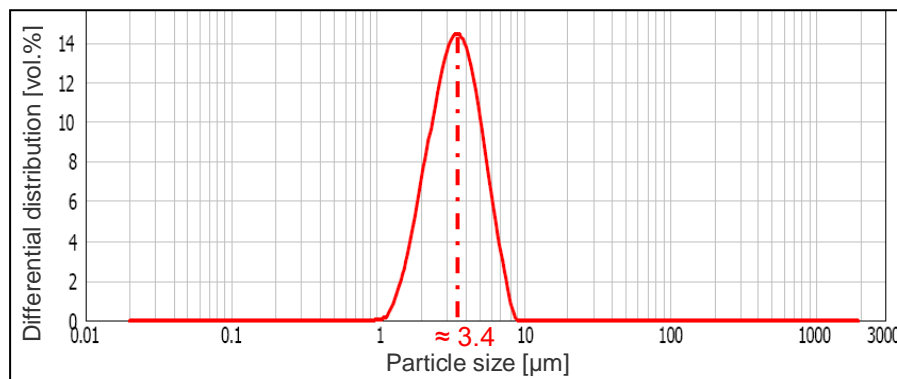
  

Powder chemical composition									
Element	Cr	Ni	Mo	Mn	Si	C	P	S	Fe
Content (%)	17.4	10.9	2.5	1.2	1.64	0.021	0.015	0.006	Bal.

One of the proper tools to observe the particle characterization of the powder is the scanning electron microscopy (SEM). **Figure 27** gives the photographs of the 316L stainless steel powder used for micro-PIM and the corresponding distribution of powder particle are indicated in **Figure 28**.



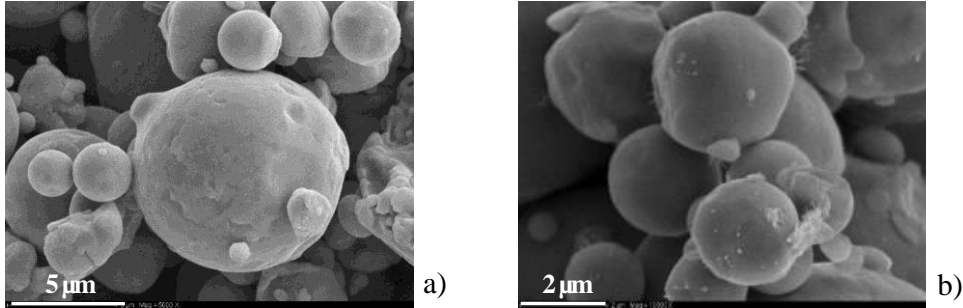
**Figure 27.** 316L stainless steel powders ( $D_{50}=3.4\text{ }\mu\text{m}$ ) used in the proposed investigations



**Figure 28.** Particle size distribution for 316L stainless steel powders ( $D_{50}=3.4\text{ }\mu\text{m}$ ) used in the related investigations

A broad particle size distribution provides a higher packing density and as a consequence, a higher amount of binder would not be necessary to produce the feedstock [83]. It is extremely necessary to

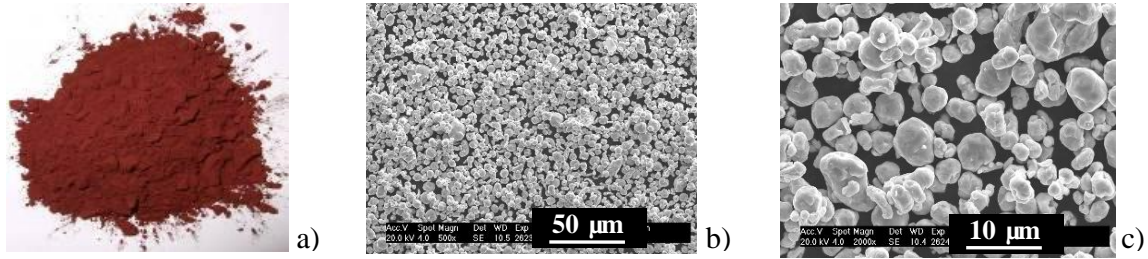
determine the particle sizes and their distribution of the employed powder, because these strongly affect the different stages of the PIM process. Furthermore, another 316L stainless steel powder with a mean powder particle equals 16  $\mu\text{m}$  has been used as well in our researches to test and compare different formulations in PIM process; the related micrographs are shown in **Figure 29**.



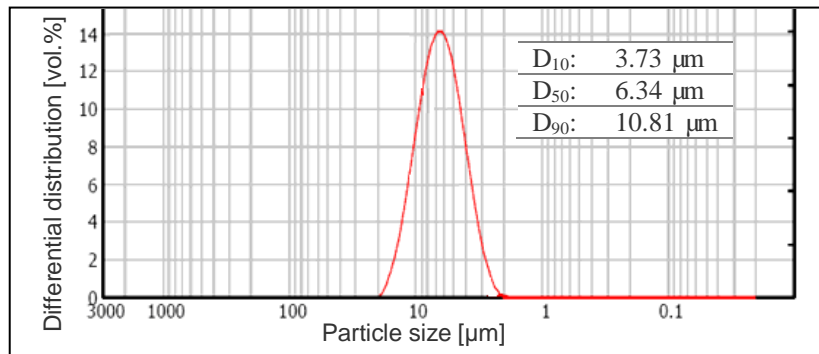
**Figure 29.** Scanning electron micrographs of 316L stainless steel powders ( $D_{50}=10.5 \mu\text{m}$ ) used in the related investigations

### 2.1.3.2. Copper powders

In order to realize the bi-material-injection experiment, a copper powder ( $D_{50}=6.34 \mu\text{m}$ ) has been used for one of the injection units. **Figure 30** shows the micro details of the powder. One can remark that, the copper particles have nearly spherical shapes that are well appropriated to obtain feedstocks with low viscosity. The melting and evaporation temperature of this copper powders are respectively 1083  $^{\circ}\text{C}$  and 2567  $^{\circ}\text{C}$ , and the density is 8.93  $\text{g.cm}^{-3}$ . The particle size distribution is given in **Figure 31**.



**Figure 30.** Copper powder ( $D_{50}=6.34 \mu\text{m}$ ) used in the proposed investigations



**Figure 31.** Particle size distribution of copper powder ( $D_{50}=6.34 \mu\text{m}$ ) used in the proposed investigations

## 2.2. Binder

### 2.2.1. The role of binder in MIM processes

Even though the binder has not to remain in the final components, it has an important influence in the MIM process, because this is the binder that transports the metallic powder particles in the mold cavity during the injection stage, and holds the required shape of the components during the ejection, debinding stage and the beginning of the sintering stage by solid state diffusion.

### 2.2.2. Choice of a proper binder

At present, there are many of possibilities to choose the binder, but no binder is perfect. For this choice, it is very important but difficult to select an appropriate one between different possibilities. Two main requirements are required for the binder: the first one is to provide an easy flow of the particles into the die cavity during molding, wax polymers which generally have low viscosity meet well this demand; the second one is to avoid separation of the powder during the preparation of feedstock and molding, and pure waxes are not sufficient with this respect. For this reason, most of binder systems contain at least two components; the added polymeric components lead to increase the viscosity in order to hold the component shape after cooling. Besides, some additives polymers like surfactants are generally employed in the binder system to coat the powder [23]. **Table 7** relates some examples of binder systems that have been related in the literature.

**Table 7.** Examples of binders for PIM

72% polyethylene glycol, 24% polyethylene, 4% tritolyl phosphate [84]
45% polyamide, 25% ethylene-bis-laurylamide, 30% N,N-diacetylpiperazine [85]
58% polystyrene, 30% mineral oil, 12% vegetable oil [86]
44% polystyrene, 44% oil, 6% polyethylene, 6% stearic acid [87]
62% paraffin wax, 33% polypropylene, 5% stearic acid [88]
80% microcrystalline wax, 20% stearic acid [89]
79% paraffin wax, 10% ethylene vinylacetate copolymer, 10% high density polyethylene, 1% stearic acid [90]
60% paraffin wax, 10% high density polyethylene, 10% polypropylene, 5% liquid paraffin, 5% dioctylphthalate, 5% ethylene propylene diene monomer, 5% stearic acid [91]
53% low density polyethylene, 26% ethylene-acrylic acid block copolymer, 21% paraffin wax, 5% stearic acid [92]

Consequently, polypropylene and polyethylene have been tested as the primary binder system to keep the component shape after injection molding and debinding; waxes have been chosen as the secondary binder in order to decrease the feedstock viscosity and to increase the replication ability of the feedstock; the additive surfactant stearic acid and oleic acid have been added to facilitate powder wetting by

lowering the surface energy of the binder-powder interface. The physical characteristics of the binders used to elaborate the feedstocks have been developed in **Table 8**.

<b>Table 8. Characteristics and contents of the proposed binder system</b>				
<b>Binder</b>	<b>Melting temperature [ °C]</b>	<b>Density [g.cm<sup>-3</sup>]</b>	<b>Linear Formula</b>	<b>Comments</b>
<b>Polypropylene (PP_G)</b>	140	0.90	$[\text{CH}_2\text{CH}(\text{CH}_3)]_n$	$M_w \approx 304940$ $M_n \approx 46832$
<b>Polypropylene (PP_A)</b>	160~165	0.90	$[\text{CH}_2\text{CH}(\text{CH}_3)]_n$	$M_w \approx 250000$ $M_n \approx 67000$
<b>Polyethylene (LDPE_G)</b>	130	0.91	$\text{H}(\text{CH}_2\text{CH}_2)_n\text{H}$	low density
<b>Polyethylene (LDPE_A)</b>	125~140	0.95	$\text{H}(\text{CH}_2\text{CH}_2)_n\text{H}$	low density
<b>Paraffin Wax (PW_G)</b>	58~60	0.91	$(\text{C}_n\text{H}_{2n+2})_m$	$M_w \approx 754$ $M_n \approx 721$
<b>Carnauba Wax (CW_A)</b>	83~91	0.99	$\text{CH}_3(\text{CH}_2)_{n+1}\text{COO}(\text{CH}_2)_{n+1}\text{CH}_3$	
<b>Stearic acid (SA)</b>	70.1	0.86	$\text{CH}_3(\text{CH}_2)_{16}\text{COOH}$	$M_w \approx 484$ $M_n \approx 475$
<b>Oleic acid (OA)</b>	16.7	0.91	$\text{CH}_3(\text{CH}_2)_7\text{CHCH}(\text{CH}_2)_7\text{COOH}$	
Note: Mw: the weight average molecular weight; Mn: the number average molecular weight.				

Here the PP\_G and PP\_A, LDPE-G and LDPE\_A are two types of polypropylene and polyethylene with different characteristics. **Figure 32** are some examples of the binders which have been taken into account in our investigation.



**Figure 32.** Examples of binder used in the feedstock, a) PP\_A, granular of 3~4 mm; b) LDPE\_G, powder of 1 mm; c) SA, powder of 0.2~0.3 mm ; d) LDPE\_A, granular of 2.5~3.5 mm; e) CW\_A, lamellar; f) OA, liquid



## 2.3. Main properties of feedstocks

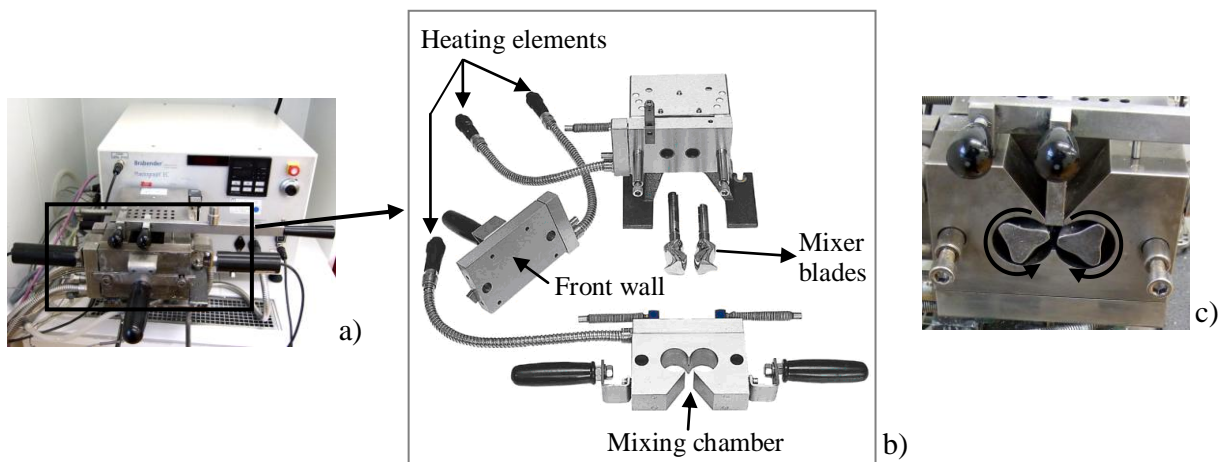
The quality of the feedstock injected into the mold cavity is one of the main aspects in the micro-PIM technology. It largely influences the final properties of the resulting micro-components associated to the process. The determination of proper feedstock formulation becomes important to satisfy the requirements. To describe exactly one feedstock, the following aspects should be correctly investigated: 1) value of mixing torque during the mixing process, 2) critical powder loading to ensure the possibility to mix the powder and the binder, 3) viscosity behavior of the mixture, 4) homogeneity of the mixture. All these four points should be properly specified, because they strongly influence the success of the injection molding stage.

### 2.3.1. Involved equipment to investigate the characteristics and properties of the feedstock

The tests concerning mixing torque tests have been realized in a Brabender<sup>®</sup> twin-screw mixer, the rheological shear viscosity has been measured by using a capillary rheometer.

#### 2.3.1.1. Twin-screw mixer

As shown in the **Figure 33**, the mixer consists principally in two mixing screws. During the mixing process, the powder and binder are put into the mixer bowl, the two blades made of special steel turn reversely towards each other at different speeds to provide excellent compounding and mixing characteristics to achieve a maximal shear rate ( $955\text{ }^{\circ}\text{s}^{-1}$ ), leading to the proper homogeneity of the feedstock.



**Figure 33.** Brabender<sup>®</sup> twin-screw mixer W 50 EHT, a) general view of the mixer; b) assembly of mixing towel; c) the two mixer blades and their counter-rotation towards each other

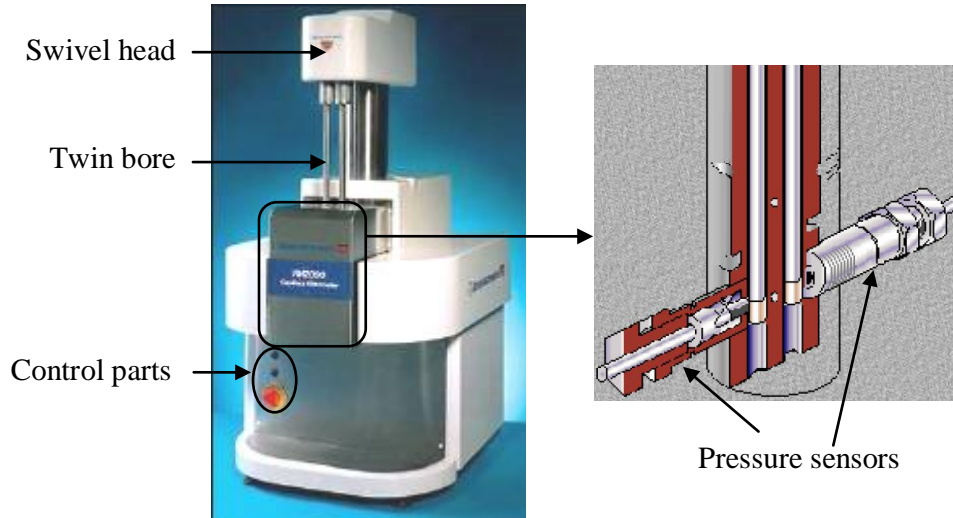
A data recording is connected with the mixer in order to get the mixing torque. The main parameters of this mixer are indicated below:

- mixing temperature: 20 to 500 °C;
- mixing speed: 0 to 120 rpm;
- maximal mixing torque: 150 N.m;
- volume of mixer bowl: 55 cm<sup>3</sup>.

### 2.3.1.2. Capillary rheometer

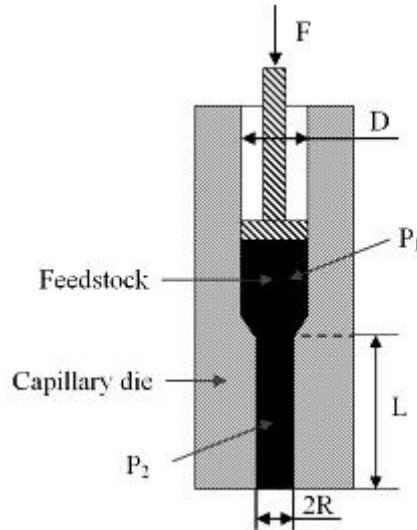
Actually, the feedstock filling into the mold cavity is a viscoplastic behavior, it means two properties: viscosity and plasticity. Meanwhile, the viscosity is the more important one that should be clearly specified. If the viscosity is too high, mold filling will be very difficult and sometimes lead to failure of injection stage may be probably caused. On the contrary, low viscosity is acceptable for MIM process which can facilitate filling the whole mold cavity. However, certain consequences can be involved by too low viscosity, such as the segregation of powder particle in the feedstock, defects like distortion, crack and fracture during and after the debinding stage, the inhomogeneous shrinkage of the sintered components, etc. The viscosity presented in this chapter is an apparent viscosity. No corrections like Rabinowitsch correction [93] to correct the shear rate at the wall and Bagley correction to correct the pressure drop (particularly for stress due to funneling effect at the entrance) [94] [95] have not been done for our viscosity results. The feedstock viscosities have to be evaluated to qualify their injection abilities, so the viscosity should be carefully measured and analyzed. A useful technique that is used to measure the viscosity over some range of shear rate or temperature instead of a single fixed point is the capillary rheometer. In our laboratory, a RH2000 Capillary rheometer (**Figure 34**) has been used to characterize the feedstock viscosities. For our investigation, most attention has been paid to the shear viscosity of our studied feedstock, thus, only single bore (the left one in the **Figure 34**) has been use to carry out the measurement. The right bore has not been introduced in our tests due to its main role is to study the elongation flow behavior. This is a double-bore rheometer, its main technical specifications are mentioned below:

- Driving load: 20 kN;
- Maximal temperature: 500 °C;
- Shear rate range: 20 s<sup>-1</sup> to 20000 s<sup>-1</sup>;
- Pressure transducer range: 30000, 20000, 10000, 5000, 1500, 500 psi (1 psi=0.00689 MPa);
- Capillary die diameter: from 0.5 to 3 mm (in 0.5mm increments) with the length/die diameter (16mm/1mm) ratio equals always 16.



**Figure 34.** RH2000 Capillary rheometer used in our laboratory for the measurement of viscosity

The determination of the viscosity can be simply described as: during a measurement in the capillary rheometer, as shown in **Figure 35**, where the P1 and P2 can be measured through the pressure sensors (see **Figure 34**).



**Figure 35.** Schematic description of the principle of the capillary rheometer in our tests

The fluid is forced by a piston with a force  $F$  through the capillary and the velocity is  $V$ , the volumetric flow rate  $Q$  and the pressure drop  $\Delta P$  are expressed in equation (5) and (6), respectively:

$$Q = \frac{\pi D^2}{4} V \quad (5)$$

$$\Delta P = \frac{4F}{\pi D^2} \quad (6)$$

Based on the non-Newtonian fluid mechanics, the apparent shear rate  $\gamma_{ap}$  and the flow rate  $Q$  through the capillary tube with  $L$  in length can be directly expressed in equation (7):

$$\gamma_{ap} = \frac{\Delta PR}{2\mu_m L}, Q = \frac{\pi \Delta PR^4}{8\mu_m L} \quad (7)$$

where  $\mu_m$  is the viscosity of the feedstock under consideration. The apparent shear rate  $\gamma_{ap}$  and the shear stress  $\tau_w$  can be obtained according to the following equation (8) and (9):

$$\gamma_{ap} = \frac{D^2}{R^3} V \quad (8)$$

$$\tau_w = \frac{2RF}{\pi D L} \quad (9)$$

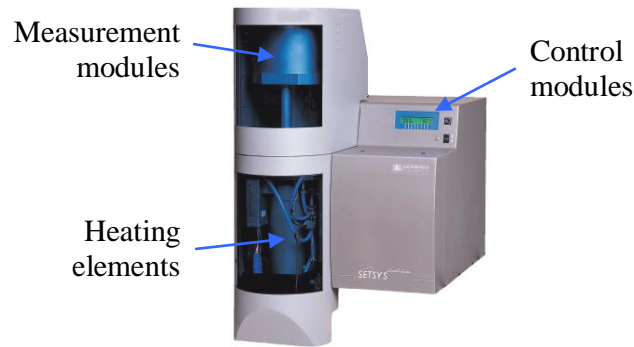
The shear viscosity  $\mu_m$  is finally given in equation (10) by the ratio between  $\tau_w$  and  $\gamma_{ap}$ :

$$\mu_m = \frac{\tau_w}{\gamma_{ap}} \quad (10)$$

The rheometer is mainly used to characterize the viscosity of the feedstock.

### 2.3.1.3. Vertical dilatometer

In order to determine the behavior of the feedstocks during the sintering stage, and then to identify the physical parameters dedicated to numerical simulation, a vertical SETSYS<sup>®</sup> dilatometer (as shown in **Figure 36**) has been set up in our laboratory to carry out the thermal and dilatometric analysis in middle of my Ph. D. thesis.



**Figure 36.** Vertical SETSYS<sup>®</sup> dilatometer used in the investigation

This SETSYS<sup>®</sup> dilatometer offers a measurement range from ambient temperature to 2400 °C. It is equipped with a carrier gas circulation where flow can be adjusted and controlled by a mass flow controller (MFC). A large variety of gas is acceptable for this equipment, such as nitrogen, hydrogen, helium, etc. A "gas mixture" option comprises the auxiliary gas circuit. The carrier and auxiliary gas circulation are linked by a three-way control valve that mixes the required gas in proportions ranging from 50/50 to 1/99. Moreover, the main feature of this dilatometer is its modularity. Different measurement modules (DTA, DSC, TGA and TMA) can be interchanged around the same structure

comprising the furnace, electronics, gas circuits, atmosphere control, etc. The TGA (Thermogravimetry analysis) and TMA (Thermomechanical analysis) modules have been used for the present study.

TGA allows measuring the variation of mass of a sample when it is subjected to a temperature program in a controlled atmosphere. This variation of mass can be a loss (vapor emission) or a gain (fixing of absorbed gases). TMA is a technique to measure the deformation of a sample under non-oscillating stress when subjected to a temperature program in a controlled atmosphere. The stresses applied can be compression, tensile or bending stresses. The associated specifications for the two modules are detailed in **Table 9**. The choice of the temperature range and atmosphere depends on the thermocouples and the furnaces which vary with the material under consideration.

<b>Table 9.</b> Specifications for TGA and TMA modules of the SETSYS <sup>®</sup> thermo analyzer		
<b>Module</b>	<b>TGA</b>	<b>TMA</b>
<b>Temperature range ( °C)</b>	20 ~ 1700	20 ~ 1700
	20 ~ 2400	20 ~ 2400
<b>Crucible volume (µl)</b>	50 to 3000	-
<b>Max. size of the sample (mm)</b>	L: 20, Φ:14	L: 20, Φ:10
<b>Resolution</b>	0.03 µg	0.2 nm
<b>Measuring range</b>	± 200 mg	± 2 mm
<b>Atmosphere</b>	Primary vacuum (10 <sup>-3</sup> mbar), secondary vacuum (10 <sup>-5</sup> mbar), pure H <sub>2</sub> , pure N <sub>2</sub> , pure He, 95% N <sub>2</sub> +5% H <sub>2</sub> ...	

## 2.4. Feedstock formulation

Based on the physical properties of binders above mentioned, three typical feedstock formulations have been developed, based on polymer + wax (Group #1), polymer + wax + acid (Group #2) and polymer + acid (Group #3) respectively. A typical powder volume loading range of 58% to 62% has been proposed for iron and steels, therefore, the powder volume loading has been initially fixed at 60% for our investigations. The typical ratios between the binders have been adapted to the 316L stainless steel powder [2], and the same ratios will be kept for the corresponding formulations even though higher powder volume loadings are involved. **Table 10** gives more details of the different feedstock formulations.

<b>Table 10.</b> Components and related contents used for the proposed feedstock formulations			
<b>Formulation</b>		<b>Compositions and Contents (in volume, %)</b>	
		<b>Powder</b>	<b>Binders</b>
<b>Group #1</b>	<b>F1</b>	316L stainless steel (60)	LDPE_G(16) + PW_G(24)
	<b>F2</b>	316L stainless steel (60)	LDPE_A(16) + PW_G(24)
<b>Group #2</b>	<b>F3</b>	316L stainless steel (60)	PP_G(16) + PW_G(22) + SA(2)
	<b>F4</b>	316L stainless steel (60)	PP_G(16) + CW_A(22) + SA(2)
	<b>F5</b>	316L stainless steel (60)	PP_A(16) + PW_G(22) + SA(2)
	<b>F6</b>	316L stainless steel (60)	PP_A(16) + CW_A(22) + SA(2)
<b>Group #3</b>	<b>F7</b>	316L stainless steel (60)	LDPE_G(38) + OA(2)

To prepare the feedstocks according to the formulations related above, the following conditions have been set for formulations F1, F2, F3, F4 and F7:

- mixing temperature: 160 °C;
- mixing rotation speed of the mixer blades: 30 rpm;
- mixing time: 30 min.

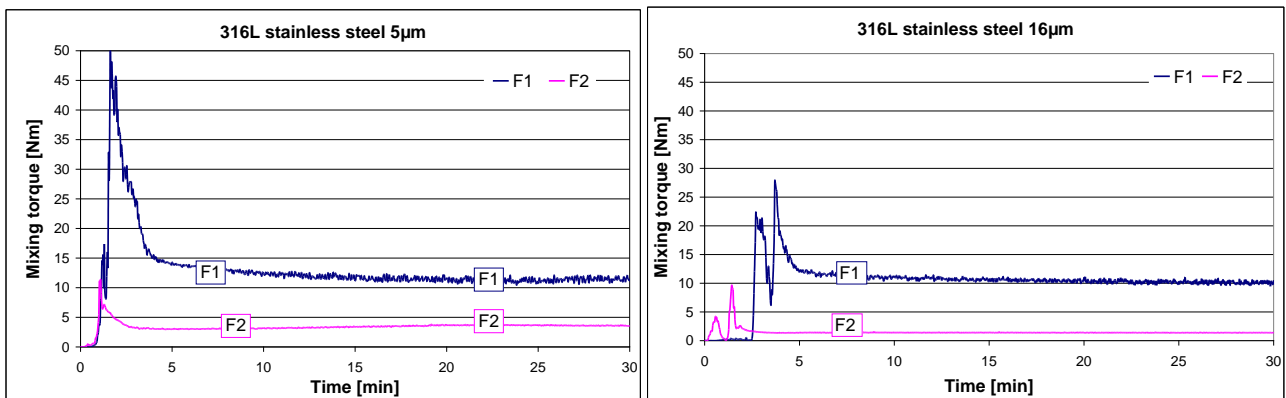
These mixing conditions have already been determined during the previous studies in our laboratory [96] [97]. Due to the high melting point of PP\_A involved in formulation F5 and F6, the mixing temperature has been increased to 180 °C for these two feedstock formulations, but the same mixing rotation speed (30 rpm) and mixing time (30 min) have been retained.

## 2.5. Choice of the appropriate feedstock formulation through physical testing

As discussed above, different tests have been carried out with the twin-screw mixer and the bi-bore capillary rheometer to select the appropriate feedstock formulations. Both 316L stainless steel powders with  $D_{50}=10.5\ \mu\text{m}$  and  $3.4\ \mu\text{m}$  have been used to do these tests.

### 2.5.1. Mixing Torque Tests

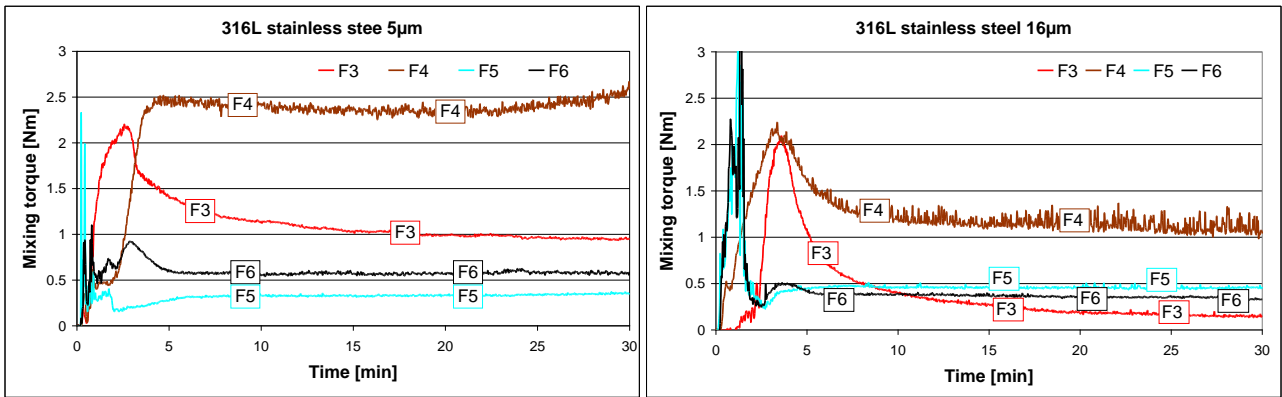
The metallic powder and the polymer in form of granules or powder is fed in the heated mixing chamber, fused and milled by the two rotating blades at a fixed rotor speed, while the torque is recorded as a function of time [98]. The curves of the mixing torque as a function of time have been shown in **Figure 37** to **Figure 39**.



**Figure 37.** Mixing torques vs. time for 316L stainless steel powder ( $D_{50}=3.4\ \mu\text{m}$  and  $10.5\ \mu\text{m}$ ) feedstock according to F1 and F2 (group #1)

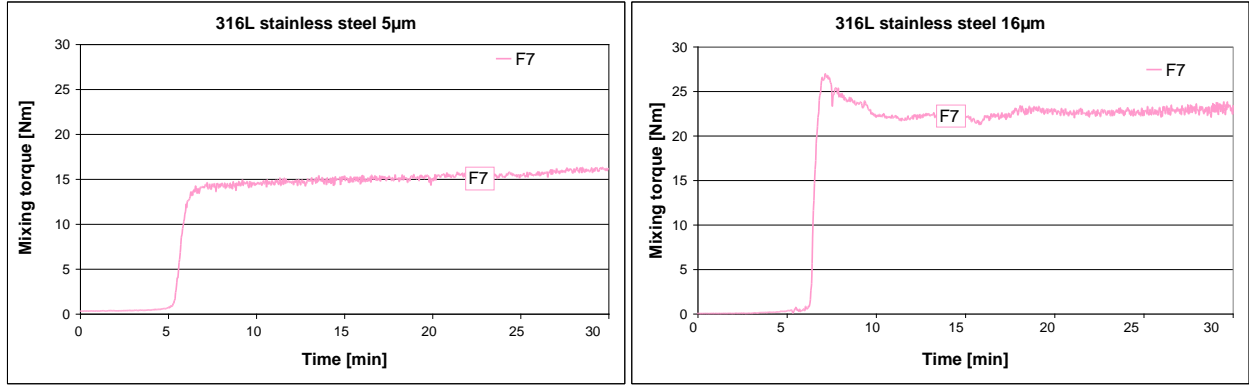
When the binder and metallic powder are introduced in the mixing chamber, they offer a certain resistance to the free rotation of the blades and therefore the torque increases. When the heat transfer is sufficient to completely melt the core of the particles, one obtains a macroscopic continuum easier to mix, the torque required to rotate the blades at the fixed speed decreases and reaches a steady state regime, and these relatively low values are the final mixing torques for each formulation [98].

From the above curves **Figure 37**, it can be observed that the mixing torques of formulations are in the same levels (about 10 Nm for F1 and about 1.5 to 3.5 Nm for F2) for both powders. The mixing torque according to formulation F1 are about 8 Nm higher than those according to formulation F2. The replacement of PE\_G by PE\_A decreases the mixing torque for these feedstocks corresponding to group #1. Some fluctuant values can be found out in the curve of formulation F1 during the end mixing stage, which means this formulation is less homogeneous than formulation F2 giving quite few disturbance considering the mixing torque curve.



**Figure 38.** Mixing torques vs. time for 316L stainless steel powder ( $D_{50}=3.4 \mu\text{m}$  and  $10.5 \mu\text{m}$ ) feedstock according to F3, F4, F5 and F6 (group #2)

A calibration of the employed twin-screw mixer with an identified polymer given by the equipment supplier has been introduced into between the mixing tests for powder of  $5 \mu\text{m}$  and  $16 \mu\text{m}$ , in order to ensure the reliability of the very low mixing torque for this group #2. As shown in **Figure 38**, it can be seen that these final mixing torques corresponding to the formulations related to group #2 are distributed in a relatively closer range from 0.2 to 2.5 Nm, the mixing torques in the same level have been presented in the other researches on 316L stainless steel powder [83]. One can observe that the mixing torque curve in the case of formulation F4 is noisier in the steady state for both powders which indicates a lower homogeneity, so this formulation is eliminated from group #2 due to this fact. Compared with the final values of the two previous tests, the mixing torques corresponding to formulation F7 shown in **Figure 39** is much higher for both powders, and the steady mixing torque for powder of  $16 \mu\text{m}$  is about 7 Nm higher than the one for powder of  $5 \mu\text{m}$ .



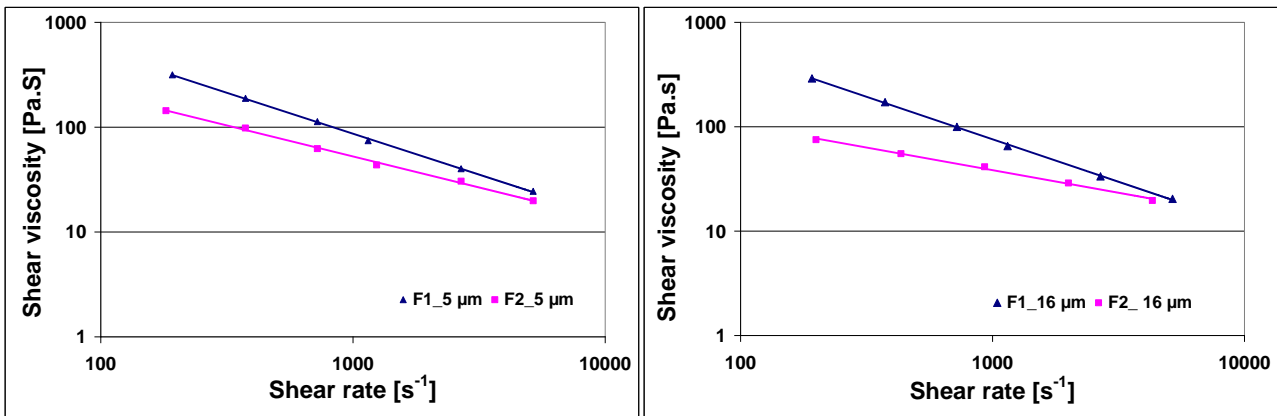
**Figure 39.** Mixing torques vs. time for 316L stainless steel powder ( $D_{50}=3.4 \mu\text{m}$  and  $10.5 \mu\text{m}$ ) feedstock according to F7 (group #3)

Through these mixing torque tests for these three groups of feedstock formulation, it is found out that the final mixing torques corresponding to F1 and F7 are much higher than these corresponding to the other formulations; the mixing temperature according to F5 and F6 formulation has to be raised about  $20\text{ }^{\circ}\text{C}$ ~ $30\text{ }^{\circ}\text{C}$  more than the other formulations in order to completely melt the binders. So formulations F2 and F3 have been retained to compose the adaptive options in terms of these mixing torque tests.

### 2.5.2. Viscosity Tests

In the related tests, the diameter of the capillary die is 1 mm. The shear rate range is  $100\text{ s}^{-1}$  to  $10000\text{ s}^{-1}$  which is usually the shear rate range occurring during the injection molding stage, and the temperature is set at  $160\text{ }^{\circ}\text{C}$  ( $180\text{ }^{\circ}\text{C}$  for formulation F5 and F6) corresponding to the mixing temperature. The feedstocks (from F1 to F7, 316L stainless steel powder,  $D_{50}=3.4 \mu\text{m}$  and  $10.5 \mu\text{m}$ ) prepared in the previous mixing tests have been tested here. The results from the capillary rheometer have been related in **Figure 40**, **Figure 41** and **Figure 42**.

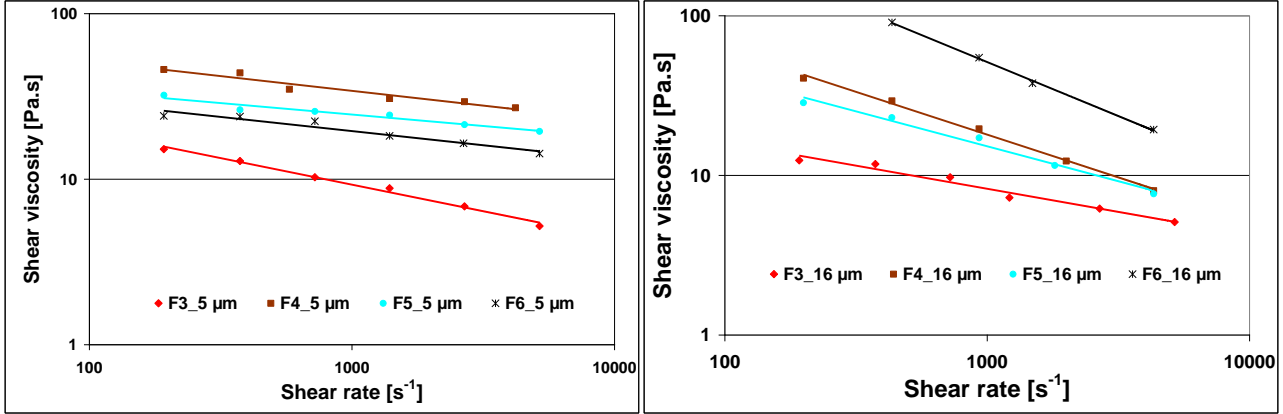
According to the curves related in **Figure 40**, the formulations F1 and F2 in group #1 give generally the same viscosity for both powders.



**Figure 40.** Shear viscosity vs. shear rate corresponding to feedstock formulations F1 and F2 (group #1)

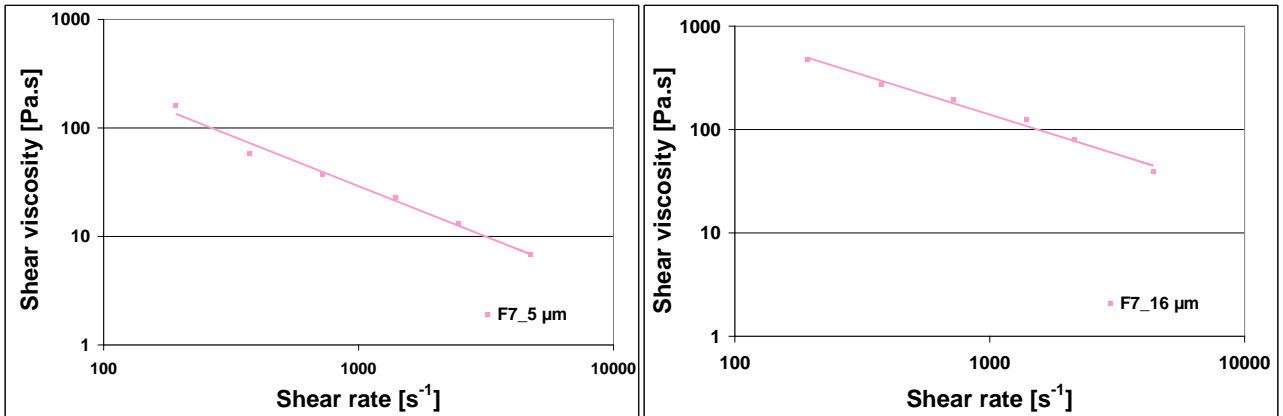


For group #2 (see **Figure 41**), the viscosities are mostly distributed in the range of 10 to 100 Pa.s (except for few individual points) considering the two powders and, the linear relationship of shear rate to shear viscosity (in logarithmic coordinate) for powder of 16  $\mu\text{m}$  is more clear compared to powder of 5  $\mu\text{m}$ . According to formulation F3, the feedstocks with the two powders gives viscosities in a close range; the feedstock prepared with the powder of 16  $\mu\text{m}$  is more viscous than these prepared with powder of 5  $\mu\text{m}$  according to formulation F4 and F5, but it has been conversely presented for formulation F6.



**Figure 41.** Shear viscosity vs. shear rate corresponding to feedstock formulations F3, F4, F5 and F6 (group #2)

The viscosities of group #3 (see **Figure 42**) are higher than the two other groups. One can observe that a lower shear viscosity has been obtained for the powder of 5  $\mu\text{m}$  in contrast to powder of 16  $\mu\text{m}$  according to formulation F7.



**Figure 42.** Shear viscosity vs. shear rate corresponding to feedstock formulations F7 (group #3)

In terms of these rheological results, one can clearly remind that the feedstock corresponding to formulation group #2 exhibits the lowest viscosities compared with the two other series considering to the same shear rates and formulation F3 is less viscous than the other formations within group #2.

Finally, combining the conclusions from the mixing torque and viscosity tests, formulation F3 has been retained for the subsequent tests by employing 316L stainless steel powder with  $D_{50}=3.4 \mu\text{m}$ .

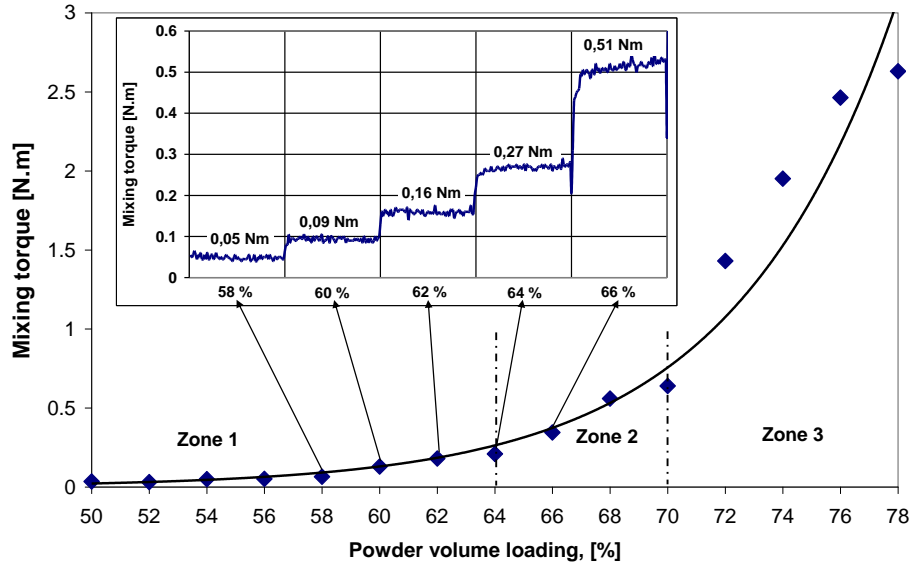
## 2.6. Determination of critical powder loading

In powder injection molding, higher powder loading is benefic for the resulting properties of the component. But the powder loading cannot be increased in an unlimited range [99]. Too high powder content means there is not sufficient binder to completely fill the desired geometry with the powder particles. So it means that undesirable voids will result from injection molding, which leads to difficulties during molding stage. Therefore, a critical powder loading can be determined, that could be associated to the possibility of filling the mold cavity. Generally, the feedstocks are loaded slightly lower than the critical value. A feedstock with optimal powder loading will exhibit proper rheological properties for injection molding, small distortion during debinding and sintering and thus appropriate mechanical properties after debinding and sintering [99]. Four different methods are compared in this analysis. The first two ones consist in mixing tests that are carried out by continuously rising powder loading or by rising separately powder loading in the two-screw mixer using the same conditions as in the tests to select the feedstock formulation. The parameters are the same ones like in the previous mixing torque tests: 160 °C for the mixing temperature and 30 rpm as the mixing rotation speed, but the weight of the powders are different. In order to determine the power law for characterizing the rheological behavior, the same capillary rheometer has been used.

### 2.6.1. Mixing tests by continuously increasing powder loading

For the first test, the powder volume loading has been increased gradually from 50% to 78% by adding the powders with an increment equals 2% for each level. This methodology has been also used in the past by T. JARDIEL et al. to determine the critical solid loading [100]. The mixing torque vs. mixing time is related in **Figure 43**. Three different zones appear looking to this curve. In zone 1, there is mainly binder in the mixture and the torque remains almost at the same low level. In zone 2 (64% to 70%) the torque begins to slightly increase starting from powder loading equal to 64%, in zone 3, the torque increase rapidly from 70% to the maximal powder loaded feedstock corresponding to 78%. So in relation with this incremental test, the critical powder volume loading has been selected from 64% to 70%. This test can provide a way to get the critical solid loading in a simple way just using one testing cycle. The complete heating cycle is around 225 min (14 steps to increases of powder loading) with intensive shearing that leads to the decomposition of the stearic acid. In order to ensure that the final quantity of feedstock will not excess the maximal content of the mixer, 70 g (about one fourth of the maximal content of the mixer) of powder has been added into the mixer cavity at the beginning of the test. It results that the mixing torques are smaller than the ones of the next test according to the same powder volume loading as shown in the small chart (in the left upper corner in **Figure 43**), especially

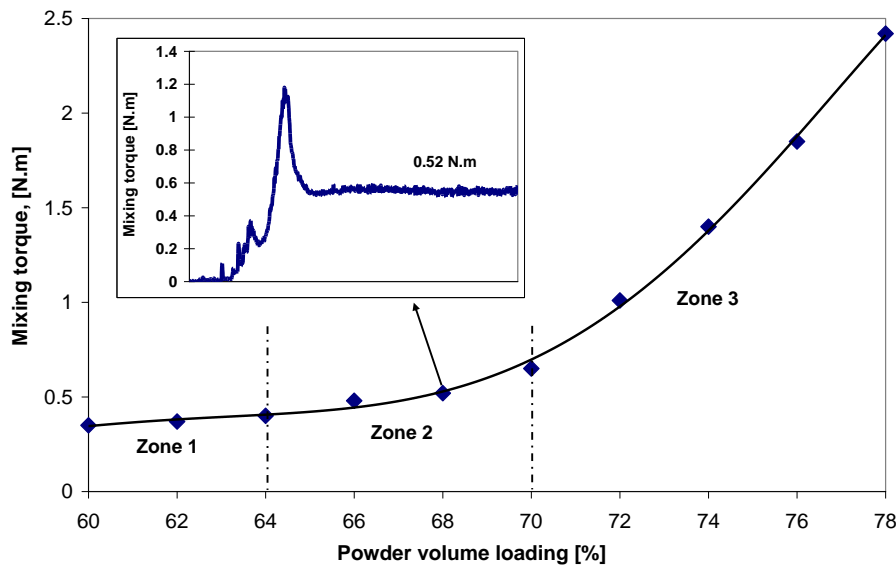
for the powder volume loading lower than 66%, this is due to the fact that always 160 g powders are involved in the subsequent mixing tests.



**Figure 43.** Mixing torque vs. powder volume loading obtained through the continuously rising powder loading technique (316L stainless steel powder,  $D_{50}=3.4\ \mu\text{m}$ , feedstock formulation F3, mixing temperature=160 °C, mixing time=30 min)

### 2.6.2. Mixing tests by batch powder loading

Instead of increasing continuously powder loading, other tests have been carried out with a different method for the second test. The mixtures have been prepared one by one with different powder loadings from 60% up to 78%. **Figure 44** shows the three different domains in the curve.

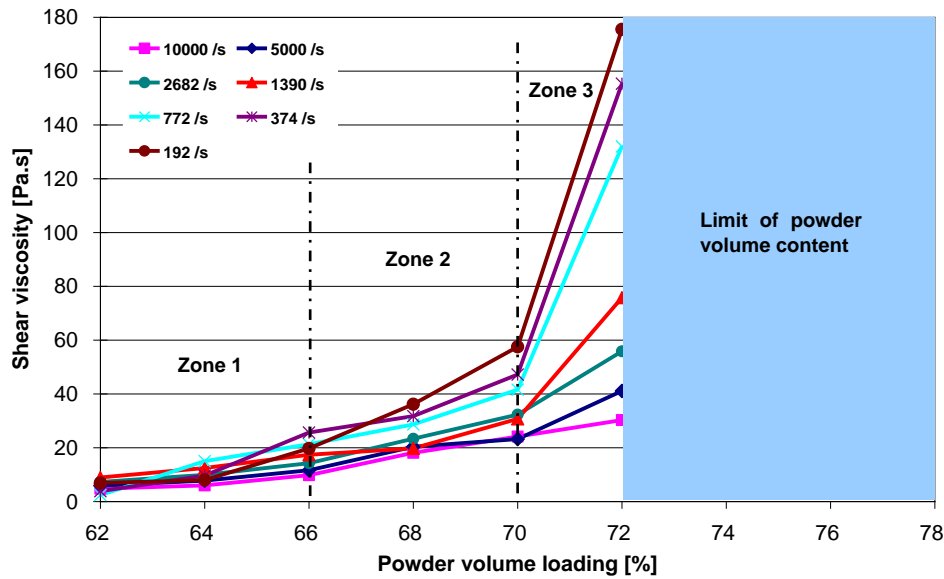


**Figure 44.** Mixing torque vs. powder volume loading related to the mixing tests by separately rising powder loading (316L stainless steel powder,  $D_{50}=3.4\ \mu\text{m}$ , feedstock formulation F3, mixing temperature=160 °C, mixing time=30 min)

From 60% to 64%, the torque remains almost stable; above 64% it begins to increase slowly; from 70%, the torque goes up fast since there are no more enough binders to properly mix the powders. One can remark that the critical powder loading is located in the range of 64% to 70%. This test proves well the conclusion of the first test.

### 2.6.3. Rheological tests

Feedstock loaded from 62% to 78% (except for 74%, 76% and 78% due to the excess content of the powder) have been sequentially tested using a capillary rheometer, considering different shear rates with the same capillary dies diameters (1 mm) and the same temperature. According to the results related in **Figure 45**, nearly the same phenomena are observed. The related viscosities corresponding from 62% to 66% (zone 1) increase slowly. In zone 2 (from 66% to 70%), these viscosities start to progressively increase, but above 70%, an abrupt rise appears. So one can observe from these shear viscosity measurements, the critical powder loading vs. powder loading is located in the range of 66% to 70%. In addition, the viscosities of the feedstock corresponding to formulation 2 are always less than 180 Pa.s, it results that these feedstock are well adapted to be injected.



**Figure 45.** Shear viscosities vs. powder volume loading obtained from the rheological tests for the feedstock loaded from 62% to 78% (shear rates from  $192 \text{ s}^{-1}$  to  $10000 \text{ s}^{-1}$ , measured at  $160 \text{ }^{\circ}\text{C}$ , 316L stainless steel powder,  $D_{50}=3.4 \text{ }\mu\text{m}$ , feedstock formulation F3, mixing temperature= $160 \text{ }^{\circ}\text{C}$ , mixing time=30 min)

### 2.6.4. Feedstock viscosity model

From the previous tests, the critical powder loading could be fixed from 66% to 70%. In order to get more accurate rheological behavior, a complementary test has been carried out to define more accurately

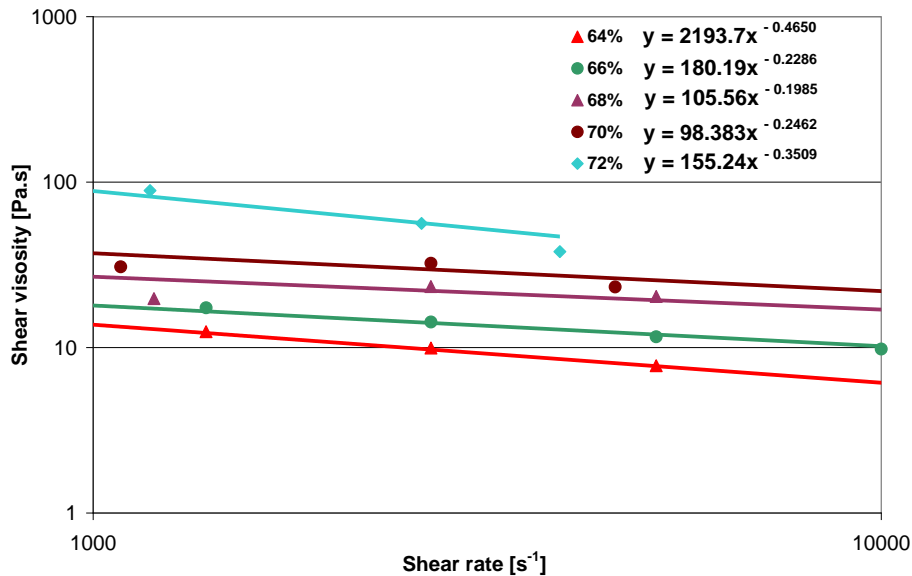
define the critical powder loading based on the previous rheological results, the related powder volume loading range is from 64% to 72%. This model has been proposed by Aggarwal et al. [101], and it expresses the viscosity as a power law temperature dependent model as [102] [103], see equation (11):

$$\eta(\dot{\gamma}, T) = B \exp\left[\frac{E}{RT}\right] \dot{\gamma}^{n-1} \quad (11)$$

where  $\eta$ ,  $\dot{\gamma}$ ,  $n$ ,  $B$ ,  $E$ ,  $T$  and  $R$  correspond to the viscosity, the shear rate, the power-law exponent, a material specific reference factor (some authors call this factor the reference viscosity), the flow activation energy for the Arrhenius temperature dependence of the viscosity, the absolute temperature and the gas constant, respectively. The value of  $n$  indicates the degree of sensitivity of viscosity against shear rate. The lower the value of  $n$  the more sensitive is the viscosity versus shear rate [83].

The values of the parameters according to equation (11) for different powder volume loading have been calculated (by using the method proposed by Aggarwal et al. [101]) and indicated in **Table 11** and the viscosities are revealed in **Figure 46**. These results are in good agreement with the studies realized by Aggarwal et al. with 316L stainless steel powder having the same spherical particle.

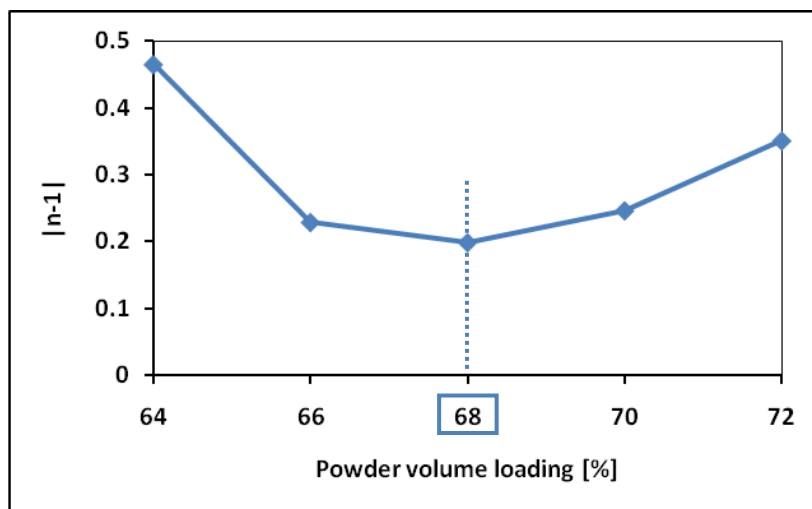
<b>Table 11.</b> Values of the different factors according to different powder volume loading			
<b>Powder volume loading, [%]</b>	<b><math>B</math> [Pa.s]</b>	<b><math>E</math> [kJ/mol]</b>	<b><math>n - 1</math></b>
64	0.154360	34.43	0.4650
66	0.012141	34.59	0.2286
68	0.002542	38.30	0.1985
70	0.000197	47.24	0.2462
72	0.061651	28.20	0.3509



**Figure 46.** Shear viscosities (expressed by power law model) vs. shear rate for the feedstocks (powder loadings varying from 64% to 72%)

Afterwards, the power-law exponent is then plotted in **Figure 47** (the viscosity has not been obtained for 72% corresponding to high shear rate range), which provides the way to determine a critical powder

loading zone corresponding to the minimal value of the exponent, and 68% has been retained for the critical powder volume solid loading.



**Figure 47.** Determination of critical powder volume loading through feedstock viscosity model

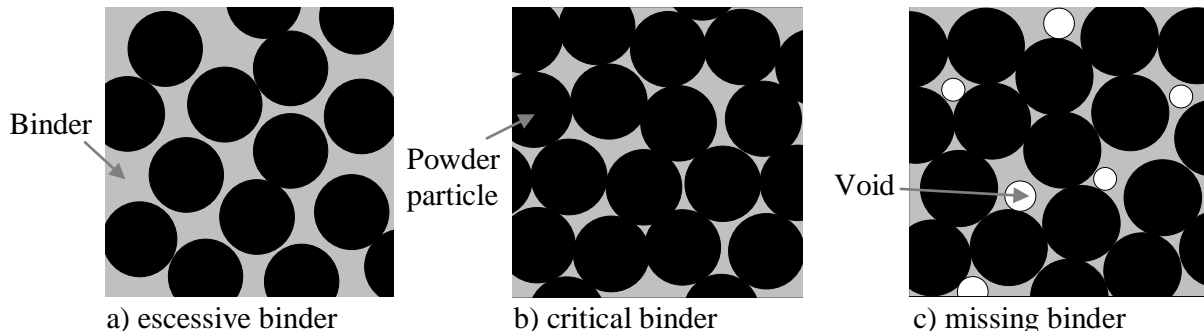
Therefore, according to the tests carried out with the appropriate formulation, the critical powder solid loading for 316L stainless steel powders ( $D_{50}=3.4\ \mu\text{m}$ ) has been fixed to 68%. In addition, from the results of the rheological tests, the viscosities of the feedstock correspond to a relatively small level.

**Table 12** summarizes the proposed methods for the determination of the critical powder volume loading of the 316L stainless steel feedstock ( $D_{50}=3.4\ \mu\text{m}$ , feedstock formulation F3), and the main features of four different methods has been given as well.

<b>Table 12.</b> Summary of the employed methods in our investigation to determine the critical powder volume loading for 316L stainless steel feedstock				
<b>Method</b>	<b>Continuous mixing tests</b>	<b>Separate mixing tests</b>	<b>Rheological tests</b>	<b>Power law model tests</b>
<b>Tested powder loading range</b>	50~78%	60~78%	60~72%	66~70%
<b>Obtained critical powder loading range</b>	64~70%	64~70%	66~70%	68%
<b>Equipment</b>	Twin-screw mixer		Capillary rheometer	
<b>Advantage</b>	Already examined by other authors, one single continuous test to do, time-saving	Simultaneous determination of injectable feedstocks with different powder volume loading	Rheological characterization of the tested feedstocks	Already examined by other authors, rheological characterization of the elaborated feedstocks
<b>Disadvantage</b>	Possible decomposition of the binder during the continuous heating	Time-consuming	Obligatory preparation of the feedstock, time-consuming	Obligatory measurement of the viscosity and preparation of the feedstock, time-consuming

## 2.7. Homogeneity tests for the feedstocks

A proper homogeneity is one of the important goals for the feedstock preparation. In practice, three different situations can be met, as sketched in **Figure 48**. In the case of an excessive powder loading the fine spaces or interstices between small particles make the mixing stage more difficult [104]. During mixing, insufficient binder will induce incomplete wetting of the powder particle surface that leads to injection molding difficulties. In contrast, excessive binder decreases the viscosity of the feedstock, and this may cause powder-binder separation under high shear stress during injection molding [23]. On the other hand, molded microstructures with low strength may cause demolding problems as they can break or be distorted during demolding [105]. Lower powder content can also cause troubles during the sintering as well as the overall dimensions can undergo higher and non-isotropic shrinkage.



**Figure 48.** Three possible situations in a powder-binder mixture [23]: a) excess of binder, b) critical binder concentration, and c) voids due to insufficient binder

Different methods have been studied to characterize the quality of a powder mixture, for example, the binder burnt-out test, the methodology based on principle component analysis (PCA) [106], etc. In the present investigation, the homogeneity of the feedstock was examined by binder burnt-out test and under scanning electron microscope (SEM).

For the binder burnt-out test, the homogeneity of the feedstock was assessed by comparing the weight loss [36] in the SETSYS<sup>®</sup> dilatometer with TGA. The available melting pots to this application are related in **Figure 49**.



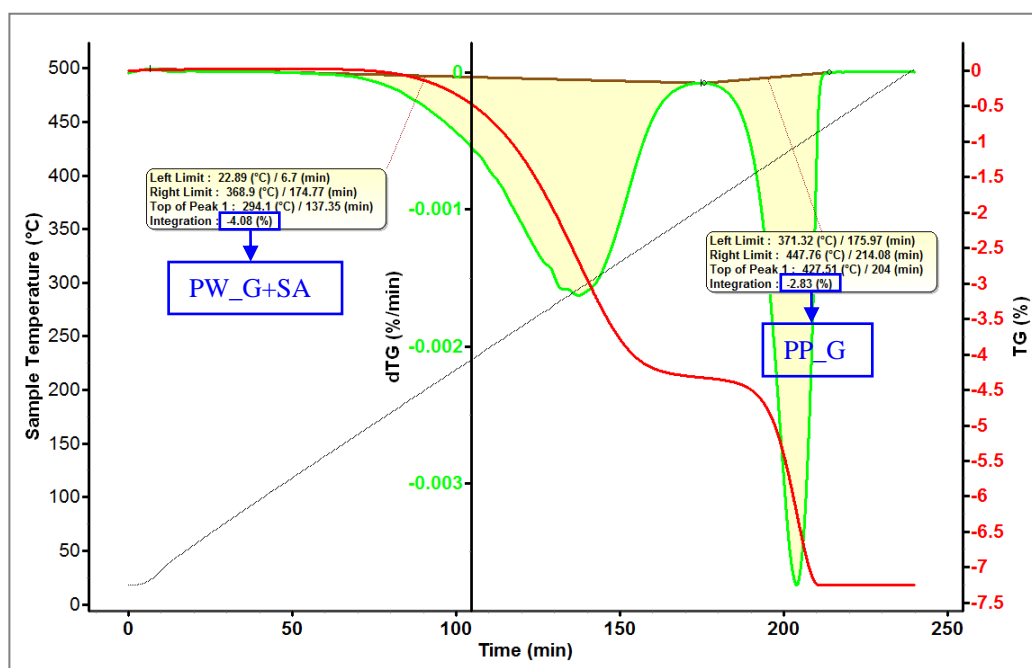
**Figure 49.** Some specific melting pots adapted to TGA (Thermogravimetric analysis) application

During the TGA measurement, the sample of the feedstock prepared according to formulation F3 (Powder+ PP\_G+ PW\_G+ SA) is contained in the selected melting pot (alumina, up to 1700 °C). The content of the binder in feedstock formulation F3 is indicated in the **Table 13**.

**Table 13.** Components and related contents in weight and volume in the feedstock formulation F3

Type	316L	PP (Polypropylene)	PW (Paraffin wax)	SA (Stearic acid)
Volume, %	60	16	22	2
Weight, %	92,90	2,80	3,90	0,40

Then the samples are put into the dilatometer furnace where an argon flow rate of 20 ml/min has been set. The temperature is set to 500 °C from 20 °C with a heating rate of 2 °C/min, the heating cycle and the corresponding results are shown in **Figure 50**.

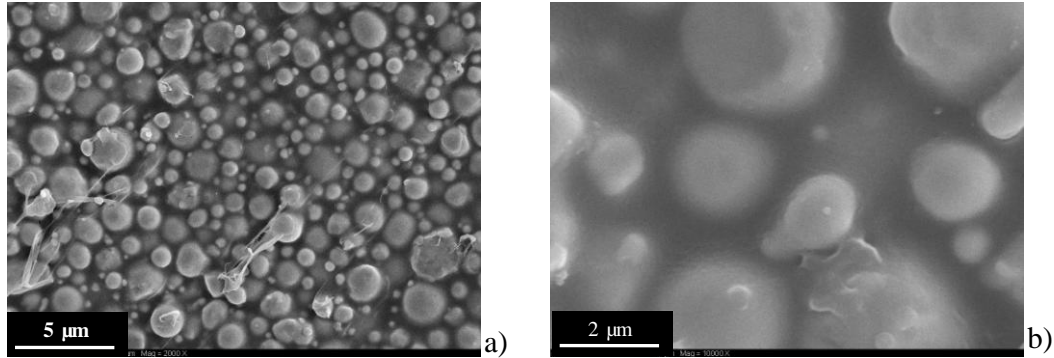


**Figure 50.** TGA results of the 316L stainless steel feedstock (D<sub>50</sub>=3.4 μm, formulation F3, powder volume loading=60%).

The two peaks related to the dTG curve correspond to the elimination of PW\_G plus SA and PP\_G respectively. The complete elimination of the binder at 427 °C corresponds to the minimum thermal debinding temperature. The total weight loss at the end of the heating cycle is about 7.2%, the value is extremely close to the theoretical binder weight in the feedstock formulation 3 (7.1% as indicated in **Figure 50**), the difference of 0.1% can be explained through the air, especially the vapor, absorbed through the feedstock. Three TGA tests with different total weight of feedstock have been investigated associated to the same conditions. The same results have been obtained. Hence, it confirms the homogeneity of the feedstock. From these essential TG analyses to determine the maximum temperature for the removal of binder in the thermal debinding cycle. It can be seen that the weight loss assisted by the degradation of polypropylene which serves as the backbone of the injected components and starts at



about 350 °C. This indicates the maximum temperature during injection moulding. In addition, the scanning electron micrographs of the feedstock are related in **Figure 51**. One can observe that the particles uniformly disperse into the matrix and are enveloped by the binder. So as a concluding remark, based on the thermogravimetry analysis results and the scanning electron micrographs, the proper homogeneity is well proved for the selected feedstock formulation F3.



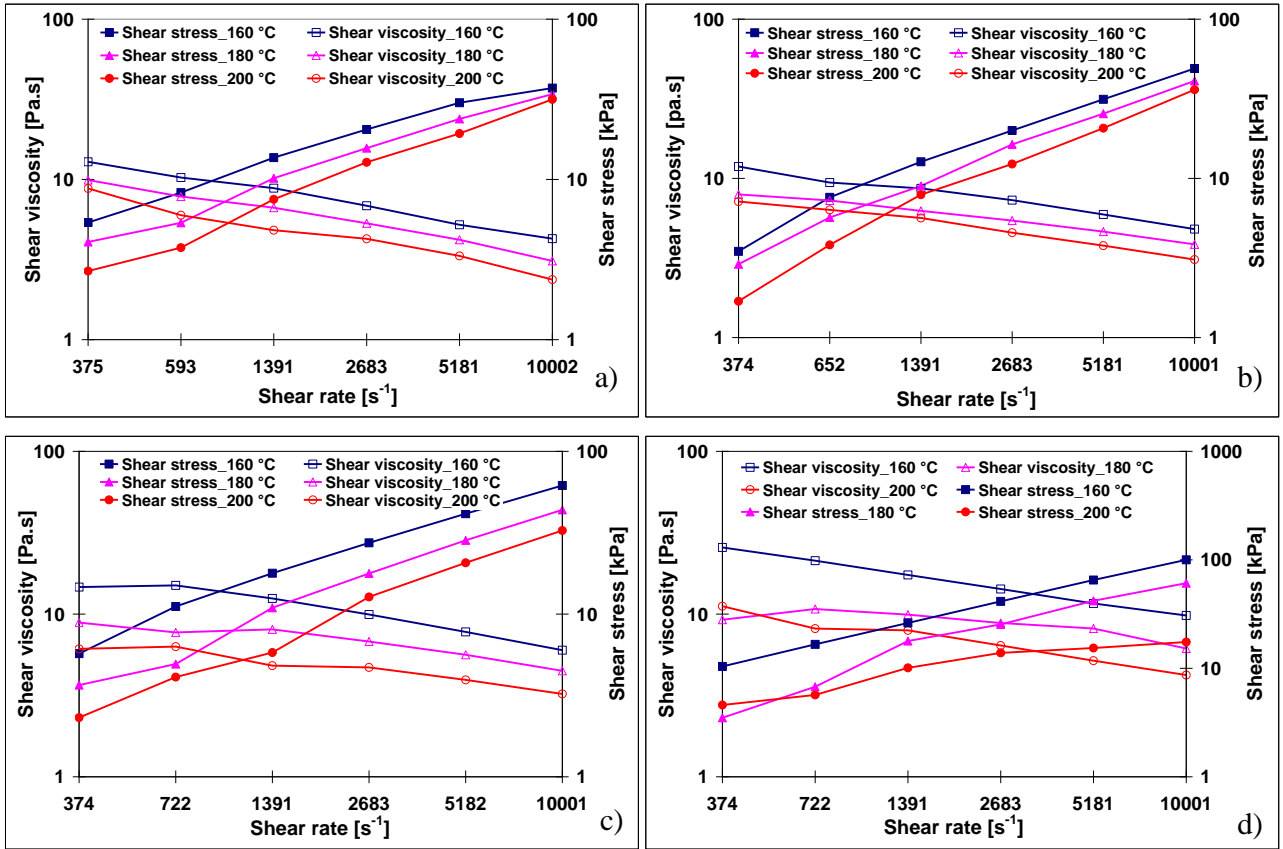
**Figure 51.** Scanning electron micrographs of feedstock after mixing stage, corresponding to formulation 2, powder loading equal 60% (mixing temperature: 160 °C, mixing rotation speed: 30 rpm and mixing time: 30 min)

## 2.8. Selected feedstock for the subsequent experiments

As the feedstock formulation F3 has been previously chosen, and the critical powder volume loading has been generally fixed at 68%. Hence, by mixing the binders according to the formulation F3 and the 316L stainless steel powder ( $D_{50}=3.4 \mu\text{m}$ ) with four different powder volume loadings (60%, 62%, 64% and 66%), four different feedstocks have been prepared for the following injection tests in chapter 3. The mixing temperature is 160 °C; the mixing rotation speed equals 30 rpm.

In **Figure 52**, the measured shear viscosities and shear stresses for these four feedstocks have been given in log10 scale for the temperatures of 160 °C, 180 °C and 200 °C. A linear relationship between the shear viscosity vs. shear rate and shear stress vs. shear rate has been indicated by these curves, respectively. It is shown that the shear viscosities decrease and the shear stresses increase with the increasing shear rates for a fixed temperature. Moreover, it is also presented that the shear viscosities and the shear stresses decrease with the increasing temperatures; in contrary, when the powder volume loadings increase, the values of the shear viscosity and shear stress rise.

However, it is interesting to note that the shear viscosity and shear stress for feedstocks loaded at 66% is less stable than the others. Since the shear stress can be considered as the minimum force required to make a relative movement between particle assemblies [107], these worse results of feedstocks loaded at 66% could be considered as the difficulty of feedstock flow resulted from the lower powder volume loading of the binder in the studied feedstock.



**Figure 52.** Shear viscosity and shear stress vs. shear rate for the 316L stainless steel feedstocks ( $D_{50}=3.4 \mu m$ ) at different temperatures with powder volume loadings of a) 60%, b) 62%, c) 64% and d) 66% according to formulation F3.

## Summary

This chapter has proposed the development of the new feedstocks, especially for fine stainless steel powders. The methodology to obtain the critical powder content has been presented and then validated through the measurement of the mixing torque and viscosity, and then the approximate powder volume loading window has been selected as well. For the feedstock based on 316L stainless steel powder ( $D_{50}=3.4 \mu m$ ), three feedstock formulation groups have been tested, and the powder volume loading has been optimized using different methods until 72%. SEM and TGA analyses have confirmed the homogeneity of these feedstocks. The rheological analysis in injection shear rate range has been carried out also until the same limit (72%). The feedstock with high powder volume loading is more appropriate for injection moulding because fluctuations of temperature will not produce an important viscosity change [2]. The critical powder volume content has been chosen up to 68%. Normally, the optimal solid content means 2 to 5% less powder than the critical content. As a consequence, an optimum powder loading of 66% has been determined to go on with the injection stage. The feedstocks based on 316L stainless steel powders ( $D_{50}=3.4 \mu m$ ) have been prepared to inject with the powder volume loading

varying from 60% to 66%, and the feedstock based on copper powder with the powder content of 60% will be injected for the micro bi-material components in next chapters.

## Chapter 3. Micro-MIM process for miniaturization and functionalization

With the elaborated and characterized feedstock resulting from previous investigation, the injection stage can be processed. In this stage, the desired form of the components should be attained without defects; this is the main objective of injection molding. Both mono-material injection with 316L stainless steel powder and bi-material injection combining 316L stainless steel and copper feedstocks have been tried to develop a micro-component integrating miniaturization and multi-functionalization.

### 3.1. Equipment used for injection molding stage

As conventional injection, micro injection molding and micro bi-material injection are also developed in our laboratory, different injection equipments have been involved for this stage: Arburg 220-S<sup>®</sup> and Battenfeld Microsystem 50<sup>®</sup>.

#### 3.1.1. Arburg 220-S injection moulding equipment

By injecting the feedstock prepared according to formulation F3 (316L stainless steel powder,  $D_{50}=3.4\ \mu\text{m}$ , different powder volume loading: 60%, 62%, 64% and 66%), the specimens dedicated to the identification tests are injected in hydraulic Arburg 220-S<sup>®</sup> (**Figure 53**) injection equipment.



**Figure 53.** Hydraulic Arburg 220-S injection equipment for the conventional injection molding

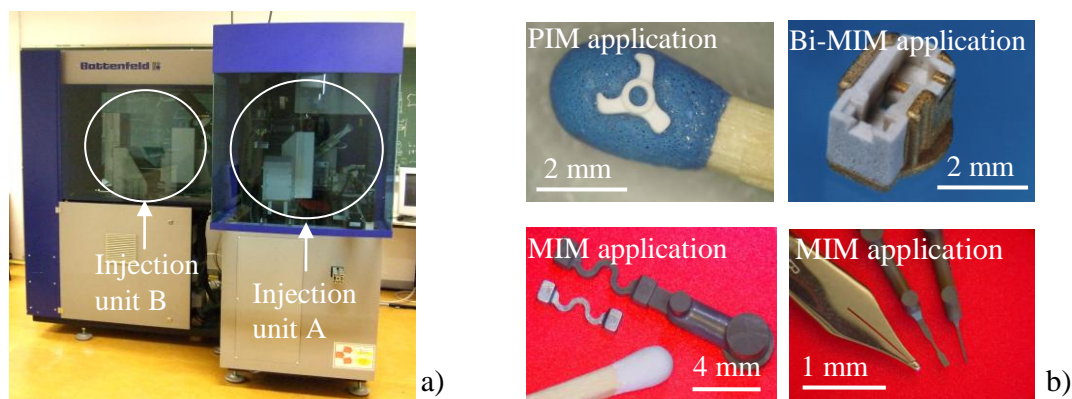
The main technical data are shown in **Table 14**.

<b>Table 14.</b> Technical specifications of Arburg 220-S injection equipment	
Clamping force (max.)	20 kN
Injection volume	3 to 12 cm <sup>3</sup>
Injection speed (max.)	366 mm/s
Injection temperature (max.)	400 °C
Injection pressure (max.)	250 MPa
Injection flow (max.)	22 cm <sup>3</sup> /s

### 3.1.2. Battenfeld Microsystem 50 injection moulding equipment

Different equipments have been developed especially for micro-injection molding and bi-material microinjection with polymers or high loaded feedstocks, such as electric injection molding equipments, appropriate units to measure accurate volume and to check the quality of the components, see Battenfeld Microsystem<sup>®</sup> or Ferromatik Milakron<sup>®</sup> [108] [109] [110]. More and more demands and requirements appear about micro-components realized by micro powder injection molding. Nevertheless, equipments available for bi-feedstock injection molding are not so common for PIM processes. Investigations and process knowledge has been developed to design adapted molds for bi-material injection molding to micro scale components during this Ph. D. thesis.

A specific micro-injection Battenfeld Microsystem<sup>®</sup> 50 (**Figure 54**) has been used to perform micro-Powder Injection Molding, a special micro bi-material injection molding equipment for biomedical and micro-system.

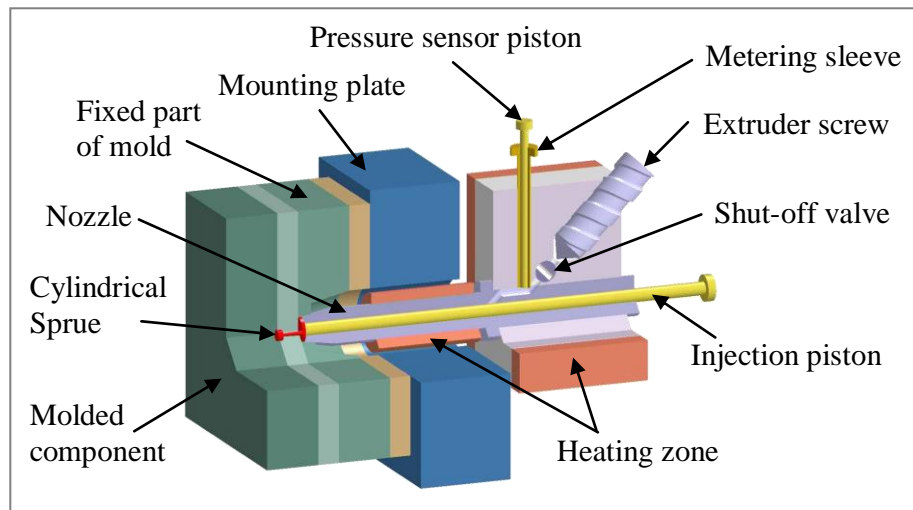


**Figure 54.** FEMTO-ST employed Battenfeld Microsystem 50 injection equipment (dedicated to micro-injection and bi-material injection molding) and examples of the components illustrated in the literature to prove the capacity of the new equipments, courtesy of Battenfeld

The micro-injection equipment consists of clamping module, injection module, swivel module, removal and handling module, quality monitoring module completed through an external vacuum pump. The injection unit is especially composed of three stages to achieve the high-precision processing of the very small injection molding volume, a 14 mm diameter extruder screw, an injection piston with a diameter of 5 mm and a 5 mm piston for pre-dosing with a accuracy of  $0.001 \text{ cm}^3$ . The injection molding capacities are the following: maximal injection speed equal to  $760 \text{ mm.s}^{-1}$ ; maximal injection pressure equal to 250 MPa and theoretical injection volume from  $0.025 \text{ cm}^3$  to  $1.1 \text{ cm}^3$ ; the maximal clamping force equal 50 kN and the ejection force equal to 1.2 kN.

In order to achieve a proper description of the injection process of Battenfeld Microsystem<sup>®</sup> 50, **Figure 55** is provided. At first the extruder screw pushes the material into the metering sleeve, and then the

materials are pressed into the nozzle where the injection piston injects them into the mold cavity. After demolding, one injection moulding cycle ends.



**Figure 55.** Sketch of the injection unit of Battenfeld Microsystem 50

### 3.1.3. Mould design and micro machining

Since the molds are specially designed, manufactured and used for micro powder injection molding, well adapted equipments (see **Figure 56**) have been set-up to manufacture the mold die cavities. The main technical specifications of these equipments are detailed in **Table 15**.



**Figure 56.** Equipment used in the investigation related to the machining of die cavities, a) DML 40 SI laser micro-manufacturing; b) HSPC 2216 high speed micro-milling and c) Charmilles Robofil 2050TW micro-Wire Electrical Discharge equipment

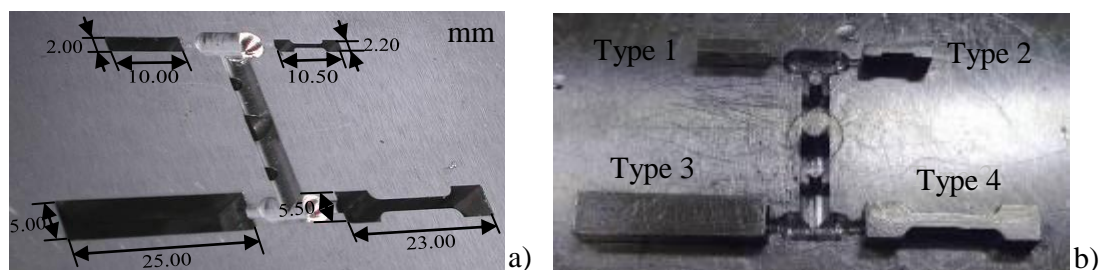
<b>Table 15.</b> Main technical specifications of the employed equipments for the mould manufacturing	
DML 40 SI	Nd: YAG laser, 3 axes mechanical, 3 axes optical, laser beam diameter: 40~100 $\mu\text{m}$
HSPC 2216	3 axes machining, 20~30000 rpm and 60000~160000 rpm, precision: $\pm 1 \mu\text{m}$ , automatic tool changer with 32 positions
Charmilles Robofil 2050TW	wire diameters: 0.33~20 $\mu\text{m}$ , maximal taper in TW mode: $\pm 30^\circ$ , max. work piece dimensions (L×D×H): 1000×490×260 mm, minimal surface roughness (steel, H=60 mm): Ra=0.10

### 3.2. Mono injection for the physical identifications of the feedstocks

After granulating the feedstock to small pellets for easy injection molding, the 316L stainless steel ( $D_{50}=3.4 \mu\text{m}$ ) feedstock is mixed homogenously according to formulation F3 with different powder volume loading (60%, 62%, 64% and 66%) is injected by using Arburg 220-S<sup>®</sup> injection equipment as mentioned above. The mold involved for these experiments is related in **Figure 57**, it was manufactured and optimized during previous Ph. D. thesis [44] in our research team, four types of specimen have been combined in the same mold, and the dimensions are indicated as well. **Figure 58** relates the injected components from this mold using the following the injection parameters:

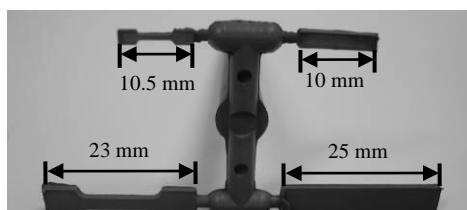
- Injection temperature: 180 °C;
- Injection volume: 4 cm<sup>3</sup>;
- Injection speed : 10 m/min;
- Injection pressure: 100 MPa;
- Injection flow: 20 cm<sup>3</sup>/s.

One can notice that the injection temperature is 180 °C, which is a little higher than the mixing temperature (160 °C) related to the preparation of the feedstock; this is to ensure that the feedstock can fill perfectly into the entire die cavity of the mold, especially for the small size specimen corresponding to type 3 and 4 with a section gate of 0.5 mm<sup>2</sup> without paraffin wax degradation.



**Figure 57.** Mold combining four types of specimen used for mono injection tests, a) dimensions of the mold cavities; b) the ejectors for the four types of specimen

According to the injected specimens related **Figure 58**, this injection is well realized for the four loaded feedstocks (from 60% to 66% in 2% increments), there is no external defect on the specimens with a constant geometry size. The beam-bending test specimens will be used to determine the viscosity modulus during the sintering stage.

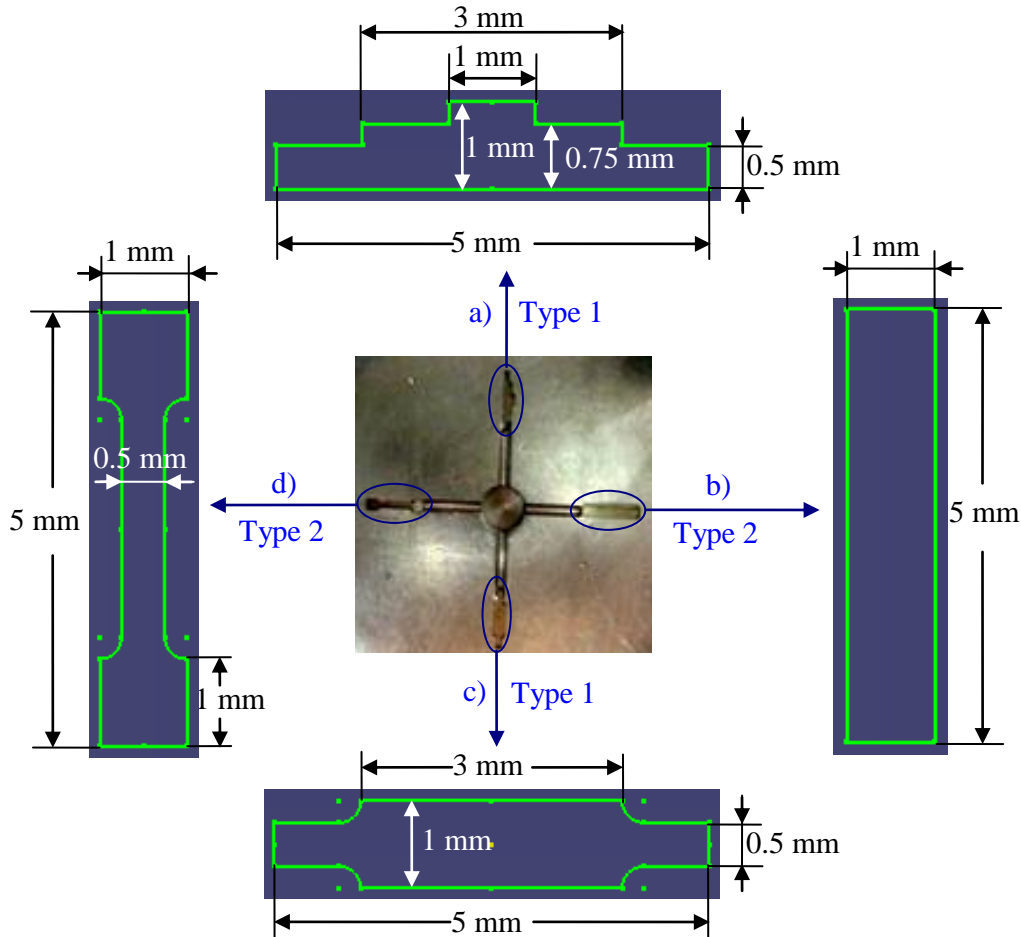


**Figure 58.** Injected specimens from the involved two-plate mold without external defect



### 3.3. Micro injection of the specimens used for validation of the simulations

Instead of using Arburg 220-S<sup>®</sup> injection equipment, Battenfeld Microsystem<sup>®</sup> 50 is also used for the micro injection of the different specimens which will be used to validate the subsequent FE simulations of the sintering stage with Abaqus<sup>®</sup>. Four types of specimen have been assembled in the same mold, the micro die cavity of this two-plate mold is shown in **Figure 59**, and the thickness of these specimens is 0.5 mm. These different specimens will be used for the simulation of sintering stage in order to compare the shrinkage and final relative density applied to the micro-components manufactured from the MIM process with the very fine powder.

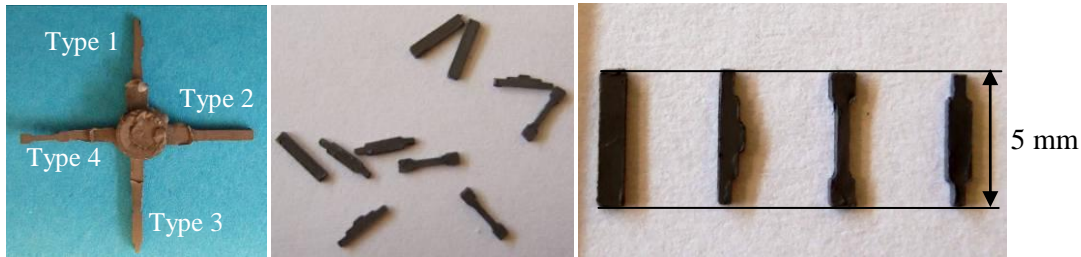


**Figure 59.** Geometry of the four different micro-mold cavities used specifically in micro-injection tests, a) Type 1, step test specimen; b) Type 2, beam-bending test specimen; c) Type 3, cross test specimen; d) Type 4, tensile test specimen

Four feedstock with different powder volume loadings corresponding to 60%, 62%, 64% and 66% (316L stainless steel powder,  $D_{50}=3.4 \mu\text{m}$ , according to formulation F3) have been tested by using this



mold. The mould has been designed by another Ph. D. student in our research team: Mr. Guillaume LARSEN). Some injected specimens are shown in **Figure 60**.



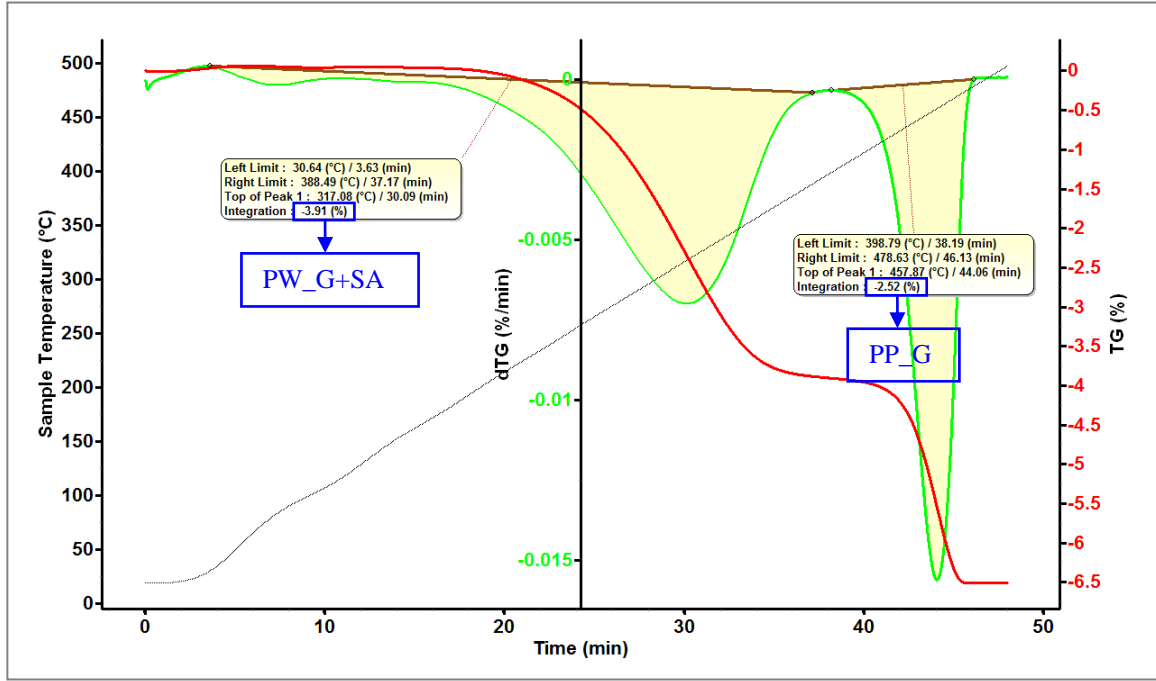
**Figure 60.** Injected micro specimens dedicated to the simulations of sintering stage with Abaqus<sup>®</sup>, realized in Battenfeld Microsystem 50 corresponding to powder volume loading to 60%

To guarantee that the feedstock filling can be correctly carried out in the micro mold cavities with a smallest semi-circle injection section gate of 0.25 mm<sup>2</sup>, the injection temperature is increased up to 210 °C (10 °C even higher than in the former mono injection of the specimens used for the identifications). The other injection parameters are:

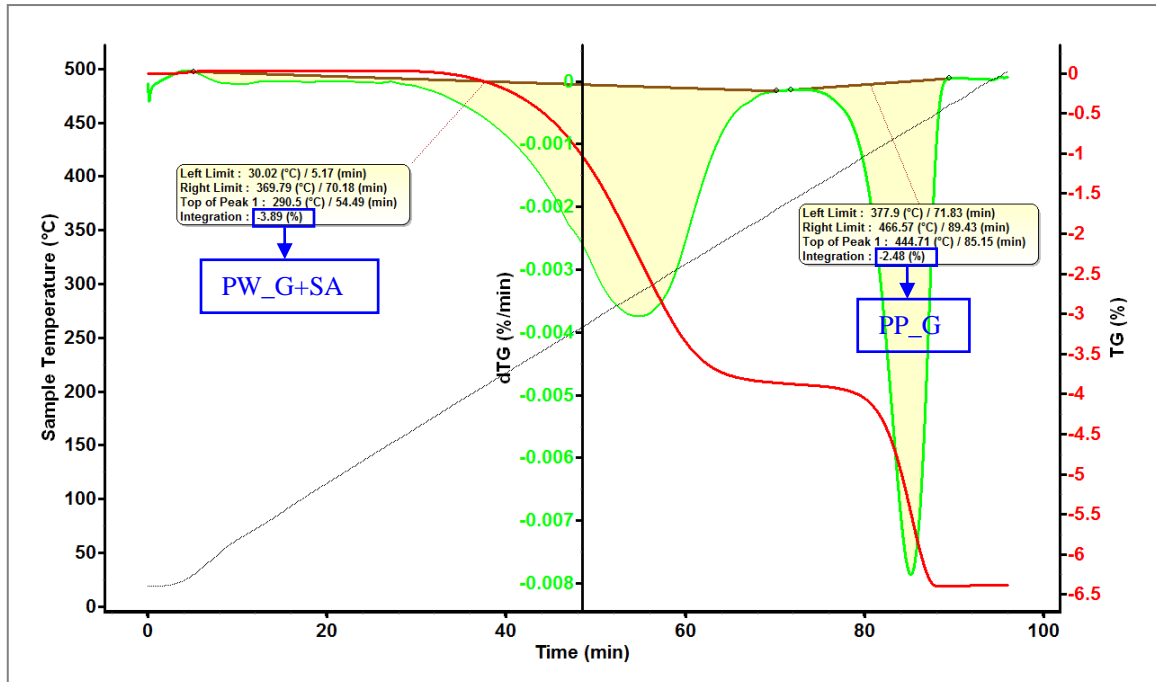
- Injection volume: 45 mm<sup>3</sup>;
- Injection velocity : 10 m.min<sup>-1</sup>;
- Injection pressure: 35 bar.

### 3.4. Homogeneity tests of the injected specimens from micro injection

The TGA analysis of the feedstock (mentioned in section 2.7) has proved that the feedstocks prepared according to formulation F3 have a good homogeneity. Due to the fact that the factors of the injection stage can influence the feedstock quality, another TG analysis has been performed on the injected specimens from micro injection in Battenfeld Microsystem<sup>®</sup> 50. Two methods have been compared for these analyses. In the first case, the tested objects are one entire specimen of the four types. Accordingly, each specimen has been split into two parts in the second case, and then two or three parts from the different types of specimen have been tested together in one analysis. The results of the micro specimens injected with the feedstock loaded at 62% have been plotted in **Figure 61** and **Figure 62** for the two cases, respectively.



**Figure 61.** TGA results for the entire specimens from micro injection with 316L stainless steel feedstock ( $D_{50}=3.4\ \mu\text{m}$ , formulation F3, powder volume loading=62%)

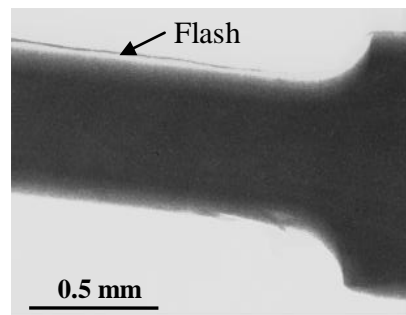


**Figure 62.** TGA results of the split specimens from micro injection with 316L stainless steel feedstock ( $D_{50}=3.4\ \mu\text{m}$ , formulation F3, powder volume loading=62%)

In terms of the results from these two different methods, homogeneity of the injected specimens or the extruded feedstock has been indicated by the good agreement of the two weight losses in each plot. However, notice that the weight losses of the polypropylene are higher than the theoretical value (2.7%, calculated according to equation (3)), which is caused by the residual polypropylene in the injection

machine. Moreover, the similar TG analyses have been carried out for the injected micro specimens with the feedstock loaded at 64%, and the same conclusion has been also reached.

Hence, in view of these TG analyses, the homogeneity of the micro specimens injected with the feedstocks according to formulation F3 has also been examined regardless the excrescent polypropylene. In addition, the segregation of the small components has been also used to verify by micro X-Ray tomography, the homogeneity of the specimen has been obtained. For example, the tomography photo of specimen type d) shown in **Figure 63** indicates the homogeneous distribution of feedstock, hardly any segregation has been presented regardless the flash in the edge area.

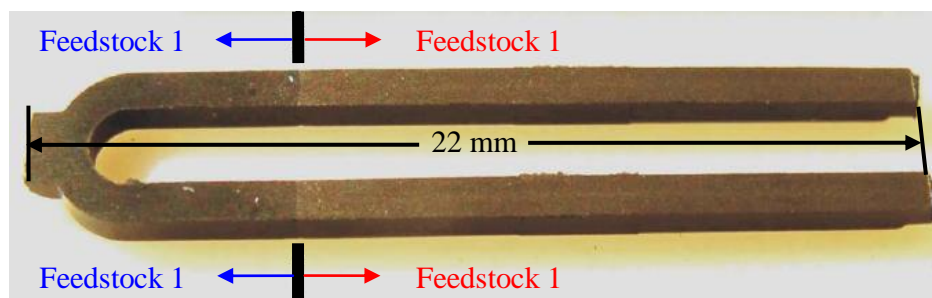


**Figure 63.** X-Ray tomography photo of micro specimens of type d) injected with 316L stainless steel feedstock ( $D_{50}=3.4\ \mu\text{m}$ , formulation F3, powder volume loading=60%)

### 3.5. Bi-material injection mold with two-plate mold

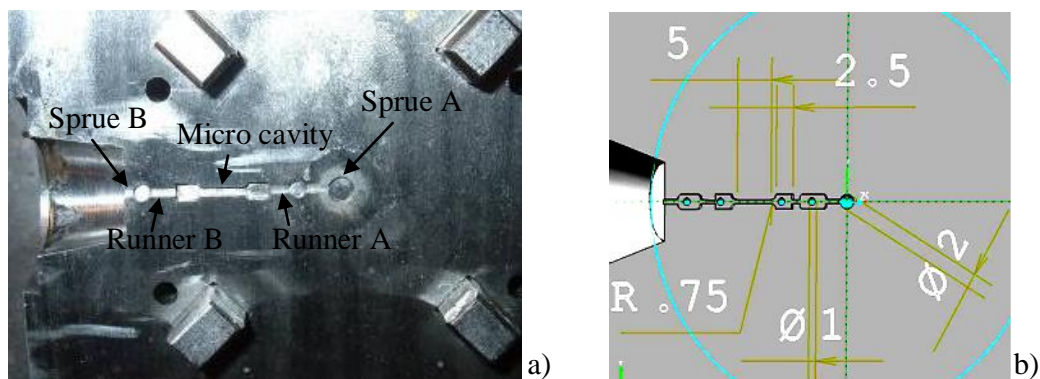
Bi-material components could be produced by using bi-powder injection molding technique. This process requires using a bi-unit powder injection molding process. It is widely recognized that the two different materials need to follow nearly similar thermal expansion and sintering kinetics, and also proper bonding characteristics [111].

Important research activities have been developed through CarCIM project since three years, especially by IKTS (Fraunhofer Institute for Ceramic Technologies and Systems) and the partners. The research investigations have concluded the possibility to inject two feedstock CIM component (see **Figure 64**) and proposed some approach to study the feedstock development in order to have the same shrinkage during the sintering stage for both materials. The topic of the project is to focus on the components in size of about 22 mm.



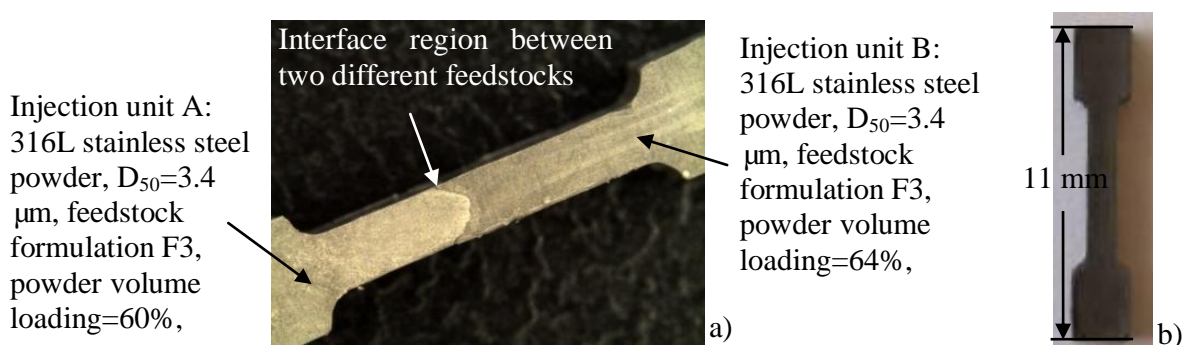
**Figure 64.** Bi-material CIM component realized during CarCIM project (STREP FP7)

During the first bi-material injection moulding test, the 316L stainless steel feedstock ( $D_{50}=3.4\ \mu\text{m}$ , according to formulation F3) with different powder loadings of 60% and 64% have been injected into a two-plate tensile test specimen mould cavity through two separate sets of sprue and rectangular runner (**Figure 65**) in Battenfeld Microsystem<sup>®</sup> 50, the dimensions of the mold cavity are given also.



**Figure 65.** Two-plate tensile mould for bi-material tensile test specimen injected on Battenfeld Microsystem 50, a) the micro cavity, sprues and runners of the mold; b) the dimensions (in mm) of this micro die cavity of this micro mold

The injected components (**Figure 66**) have been successfully obtained without external defects, the size and weight of the specimens are uniform. The injection temperature is  $220\ ^\circ\text{C}$ ; the injection volume for both injection units are  $30\ \text{mm}^3$  and the injection pressure is 40 bar.



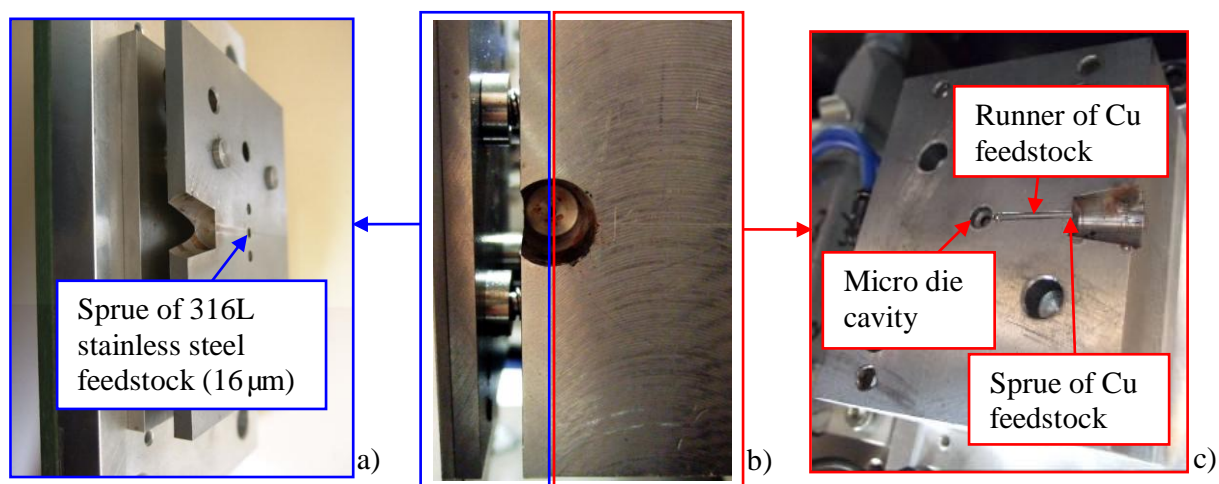
**Figure 66.** Tensile test specimen injected with feedstock loaded at 60% and 64% according to formulation F3, a) enlargement of the interface region between the two different region; b) the resulting injected tensile test specimen

Even the injection section during this bi-material injection is bigger than in the previous tests, the injection temperature is set at  $220\ ^\circ\text{C}$  due to the high powder volume loading of 64% to ensure that the correct feedstock filling can be achieved. In the photo taken under microscope, the feedstocks represent two different colors, because the feedstock loaded at 60% has less 316L stainless steel powder than the one loaded at 64%, and this metal powder is not brilliant before sintering, so the part with more powder particles is darker than the other. However, it is clearly shown that the interface between the two feedstocks is not straight, and its position varies with the injection parameters; this is related to the fact that the die cavities for both feedstocks are not separated, and they are injected simultaneously, so the

front flows of both different feedstock meet together to form the interface, but this irregular meeting of the feedstocks is not able to be repeated uniformly. Consequently, another mold specially designed for bi-material injection molding with two separated injection chambers are developed for the next bi-material injection test.

### 3.6. Bi-material injection with three-plate mold

As lots of research activities related to injection moulding with 316L stainless steel powder have been realized in the research team since long time, some other powders have been gradually introduced into the studies. In this thesis, in order to carry out the bi-material injection moulding, a Cu powder has been taken into account in this investigation. For this bi-material injection test, a three-plate mold has been developed in order to clearly define the separated die cavities for each feedstock, thus the interface between both feedstocks can be well controlled. This mold has been specially designed and manufactured during this Ph. D. thesis, the design of the mold is based on the knowledge issued from the two different polymer domains. The design of this mold is shown in **Figure 67**.

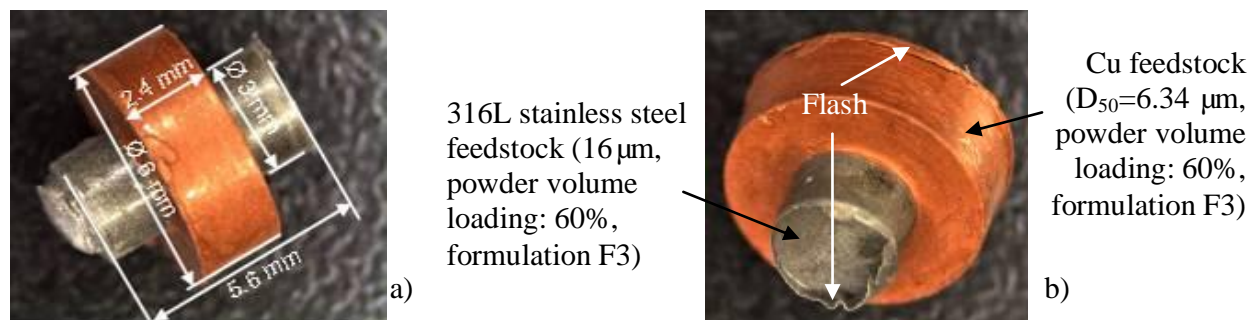


**Figure 67.** Three-plate mold for bi-material injection moulding dedicated to the injection of feedstocks based on 316L stainless steel (16 µm) and Cu powder according to formulation F3, a) fixed plate side; b) three plate mould in closed state and c) mobile plate side

The resulted components from this bi-material injection stage is shown in Figure 68, the central cylinder ( $\varnothing$  3mm $\times$ 5.6 mm) is injected with the 316L stainless steel (16µm) feedstock, while the ring ( $\varnothing$  6mm $\times$ 2.4 mm) around the central cylinder corresponds to the Cu powder ( $D_{50}$ = 6.34 µm) feedstock. Both feedstocks have been prepared according to the formulation F3 with 60% as the powder volume loading. During the injection tests, the Cu feedstock is firstly injected, and then the 316L stainless steel feedstock is injected afterwards. The interval between the two injections is about 0.2 second corresponding to the exit of the internal core. The main injection parameters are same for both injection



units: injection temperature equal 220 °C, injection pressure equal 40 bar, except for the injection volumes: 45 mm<sup>3</sup> for the 316L stainless steel feedstock and 60 mm<sup>3</sup> for the Cu feedstock.



**Figure 68.** Bi-material component injected with 316L stainless steel feedstock (16 μm, powder volume loading: 60%, formulation F3) and Cu feedstock (powder volume loading: 60%, formulation F3), a) the dimensions of the component; b) the two feedstocks in the component

However, there are still some flashes in edge region, the cause of the phenomena is possible the loose fits between the moveable and the fixed parts of the mold or high injection pressure.

However, this bi-material injected component has been manufactured without obvious defects like cracks, short shot, sticking and so on, in concluding, the bi-material injection combining the feedstocks prepared according to formulation F3 with different metal powders has been correctly carried out.

## Summary

The feedstocks involved in this chapter have been prepared using formulation F3, but they are based on different metallic powders: 316L stainless steel (5 μm and 16 μm) and copper (D<sub>50</sub>= 6.34 μm). Considering the components from the mono-injection, micro injection, micro bi-injection with two types of mold by injecting the feedstock retained from the 8 different feedstock formulations, this stage has been properly investigated.

Compared with the other injection tests based on the 316L stainless steel carried out by the previous Ph. D. theses, the higher volume loadings (62%, 64% and 66%) have been firstly reached by involving finer powder (D<sub>50</sub>=3.4 μm) in the feedstocks, various different components have been obtained without external defects, and a good homogeneity repartition between powder and binder has been observed. Some injected micro-components have a small size compared to previous studies. Secondly, the micro-injection and micro bi-material injection of these higher loaded feedstocks have been tested after the design and manufacturing of the mold. Especially, the micro bi-material injection combining one 316L stainless steel feedstock and one Cu feedstock has been tried in Battenfeld Microsystem<sup>®</sup> 50 in order to begin some new activities using the miniaturization and functionalization components.

## **Chapter 4. Debinding and sintering stages of MIM process for the components obtained by bi-material and micro-injection**

In this chapter, the debinding and sintering stages for the injected components from the previous injection stage are demonstrated. In the debinding stage, the mono injected specimens used for the identification (mentioned in section 3.2), the micro-injected specimens used for the simulations (mentioned in 3.3) and the specimens injected with two different 316L stainless steel feedstocks from bi-material injection with two-plate mold (mentioned in 3.4) have been debinded. However, the sintering stage has been performed only for the specimens dedicated to the identification and simulation. The resulting components from these two stages are related in this chapter. Moreover, the observations of the sintered components are covered as well.

### **4.1. Thermal debinding stage**

The debinding stage is a complex process (and it exists different debinding techniques), which consumes a major part of the processing time [112], for instance, in this thesis the debinding time is 24 hours in contrast to 30 min for mixing and 1 min for injection. Debinding stage is considered as one of the most critical steps in the processing technology among the four main stages of the MIM process. Due to the factors involved with solvent debinding, (chemical handling, health concerns with the solvent vapor and their recovery), solvent debinding has been excluded from our research.

Accordingly, the most popular debinding technique, thermal debinding, has been used in our studies under argon atmosphere for the sake of simplicity, safety and environment respect.

#### **4.1.1. Equipment used for thermal debinding stage**

A laboratory-scale debinding oven (**Figure 69**) is used to carry out the thermal debinding for the injected specimens from the previous stage. The principal technical specifications of this oven are related below:

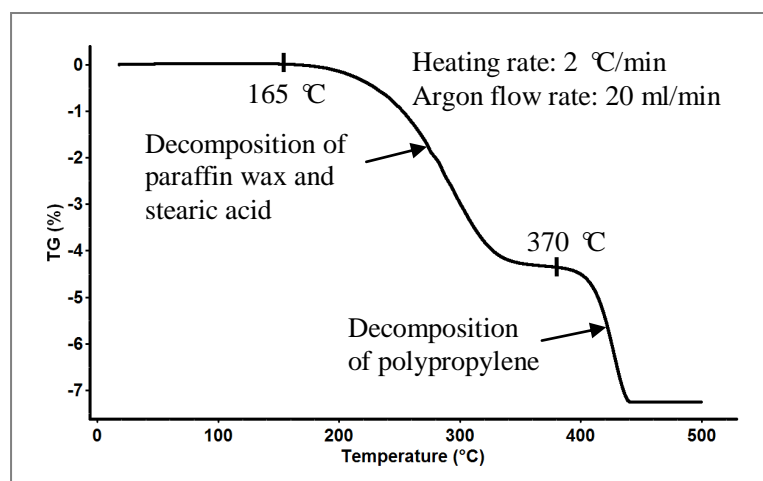
- Test temperature (max.): 300 °C;
- Volume (max.): 27 L;
- Gas circulation: air, argon;
- Gas flow (max.): 200 cm<sup>3</sup>/min.



**Figure 69.** Thermal debinding oven used in our analyses

#### 4.1.2. Debinding cycles and atmosphere

In the literature, previous works related to the thermal debinding mechanisms and kinetics [113] [114] [115] [116] [117] have already been performed, most of which focused on thermal debinding processing under a protective atmosphere, but for some active and easy-oxidized powders such as stainless steel and magnetic material powder, thermal debinding in vacuum is still very effective, and sometimes it is the only possibility [118]. Using thermal debinding, the lower molecular weight constituents are usually decomposed by evaporation or wicking. The capillary force moves the liquid binder from the center of the part to the surface where evaporation occurs. When the lower molecular weight components are removed, the decomposition of the higher molecular weight components will take place at a higher temperature by breaking off into lower molecular weight components [119]. They are usually decomposed by either chain depolymerization or random decomposition [120]. Therefore, the temperatures should be carefully selected for thermal debinding with respect to the binder degradation points [119]. Hence, the results of the thermogravimetry analysis (from 20 °C to 500 °C, heating rate of 2 °C/min, argon flow rate of 20 ml/min) for the 316L stainless steel feedstock ( $D_{50}=3.4\ \mu\text{m}$ , formulation F3, different powder volume loading=60%) should be taken into account, as shown in **Figure 70**.

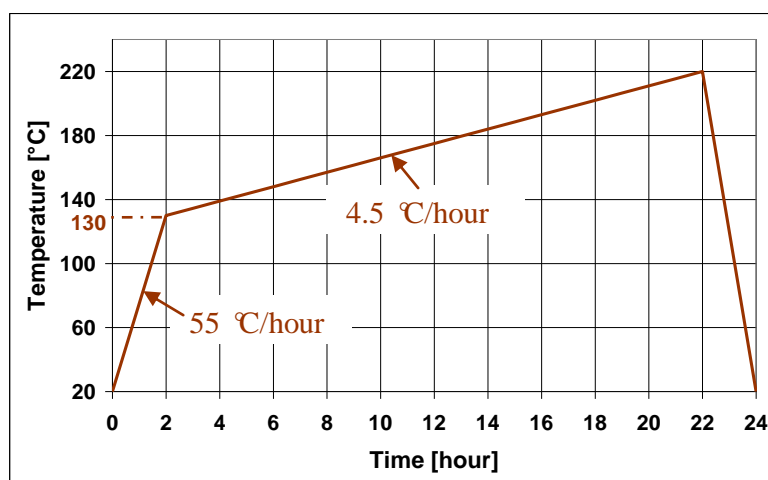


**Figure 70.** Thermogravimetry analysis for the 316L stainless steel feedstock ( $D_{50}=3.4\ \mu\text{m}$ , formulation F3, different powder volume loading=60%)



The thermogravimetry profile indicates that the first mass decrease starts at about 165 °C and completes at about 370 °C, which represents the decomposition of the paraffin wax and stearic acid (lower molecular weight components) in the formulation F3. Then the second degradation takes place from 370 °C upto 440 °C assisted by the decomposition of polypropylene (the higher molecular weight components).

According to the above analysis, a debinding cycle composed of two ramps has been employed and plotted in **Figure 71**. As it is shown, the injected compacts have been firstly heated with a heating rate equal 55 °C/hour from the 20 °C to 130 °C (lower than the beginning temperature of the decomposition of paraffin wax and stearic acid) to vaporize the water vapor absorbed in the injected components. Then the temperature is increased up to 220 °C with a very slow heating rate equal 4.5 °C/hour to eliminate the paraffin wax and stearic acid, without removing the polypropylene which serves as the backbone of the debinded porous components. Finally, the components are cooled during 120 min to reach ambient temperature.



**Figure 71.** Debinding cycle involved in the thermal debinding stage

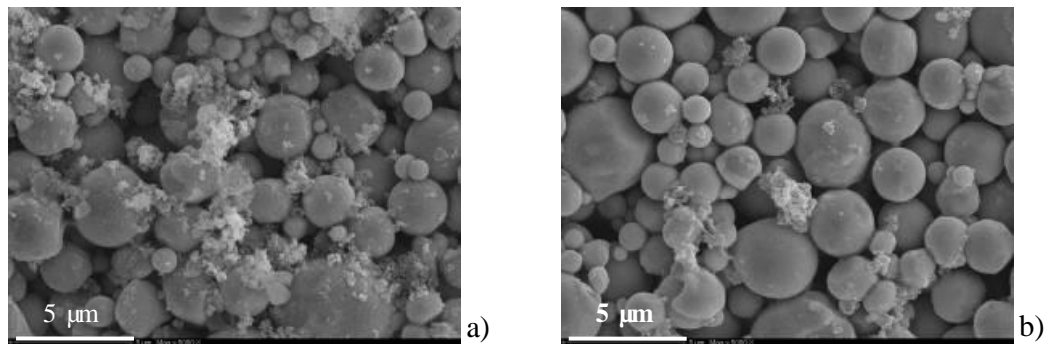
Gas flow rate is very important to ensure that the binder is swept away to prevent defects. When the gas flow rate is not high enough, some of the carbon in the binder will become carbon black on the part surface and some of potentially cause unexpected melting at high temperature sintering. Also, the components become more impressible to indicate defects such as cracking and blistering if the gas flow rate is too low. During the removal of the binders in our investigation, the argon gas flow (non-reactive atmosphere to prevent oxidation of the metallic powder) in the oven is 40 cm<sup>3</sup>/min in order to prevent the possible defects assisted by the improper gas flow [121].

Afterwards, the observations of the weight loss of binder have been carried out for the porous components from this debinding cycle. **Table 16** specifies the fractions of the removed binder to the initial mass of binder before debinding stage for the specimens injected with 316L stainless steel feedstocks with two different powder volume loadings.

**Table 16.** Fraction of the removed binder for the specimens injected with 316L stainless steel feedstock ( $D_{50}=3.4\ \mu\text{m}$ , formulation F3, different powder volume loading)

Powder volume loading of the specimens	Percentage of the removed binder
62%	71.02%
64%	75.06%

As suggested by the results, about 70% to 75% of the binders have been removed leading to open porosity in the component. The morphology of the debinded structures (**Figure 72**) has been examined using a scanning electron microscope (SEM). In both figures, the flocculent bulks between the spherical powder particles are the remaining binders. It is clearly shown that the removed binder for the specimen injected with feedstock loaded at 62% (**Figure 72 a**) is less than in the specimen injected with feedstock loaded at 64% (**Figure 72 b**), which results from the higher binder content (38%) in the specimen injected with feedstock loaded at 62% in comparison to specimen injected with feedstock loaded at 64% (36%).

**Figure 72.** Debinded structure of the specimens injected with 316L stainless steel feedstock ( $D_{50}=3.4\ \mu\text{m}$ , formulation F3), a) feedstock loaded at 62%; b) feedstock loaded at 64%.

The debinded components according to this debinding cycle are free of defects as creating residual stress, etc. As example, **Figure 75** and **Figure 79** show that the initial shape of the injected components are well kept by the debinded porous components, no dimension change has been found out between the injected and the debinded specimens.

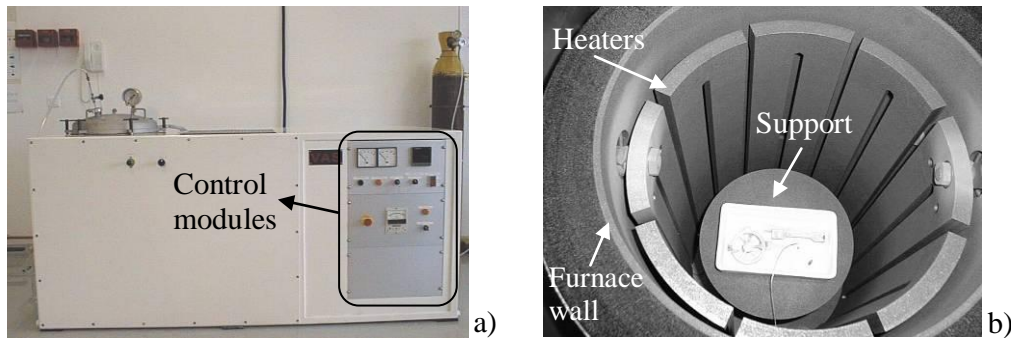
## 4.2. Sintering stage by solid state diffusion

Since the final mechanical properties are strongly affected by the sintering stage, this stage is commonly considered as one of the important step among the four MIM processing steps. The sintering stage consists of bonding the particles together by solid state diffusion to form a homogenous part when densification is achieved [122]. In the sintering stage, the pores inside the porous debinded components are eliminated. The porous parts resulting from the debinding stage are heated up to a temperature slightly lower than the melting temperature of the material used in the process, the powder particles bond together by solid-state diffusion.

#### 4.2.1. Equipment used for sintering stage

Since the objective of the sintering tests is not mass production, a batch furnace (Figure 73) that offers a maximal temperature equal 1850 °C has been used. In contrary, the batch furnace is more flexible than continuous furnace. The principal technical specification of the furnace is given below:

- Test temperature (max.): 1850 °C;
- Volume (max.): 50 L;
- Atmosphere:
  - gas circulation: argon, helium or mixture of both;
  - primary vacuum:  $10^{-3}$  mbar, secondary vacuum: 10-5 mbar;
- Temperature control: one command thermocouple and another one of S type (platinum - 10% rhodium) set-up in center of the heaters;
- Component holder: ceramic plates;
- Heater elements: graphite.



**Figure 73.** Furnace (provided by VAS®) for sintering stage: a) exterior view; b) interior view of the chamber

Actually, during the sintering stage, the pores may coarsen and grow due to the inner expansion of the gas in the pores when sintering is processed at too high temperature [123]. But there is no gas trapped when the sintering stage is carried out in vacuum atmosphere. Hence, primary vacuum is used in the related experiments.

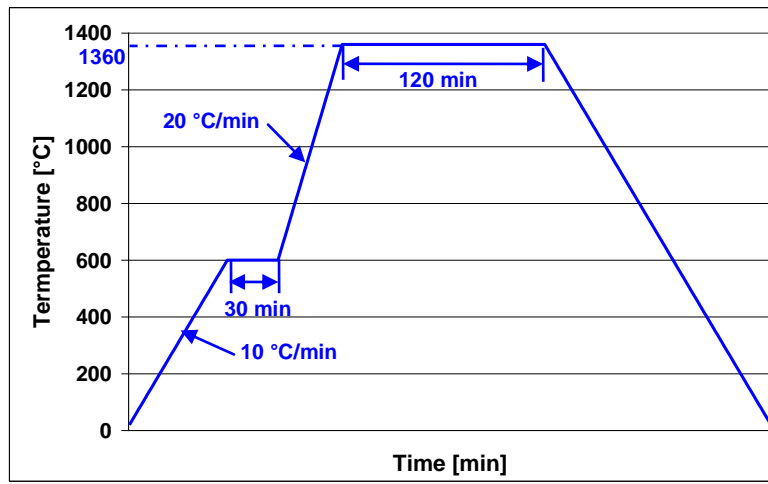
#### 4.2.2. Sintering cycles for bi-material injected specimens

The specimens injected with two differently loaded feedstocks have been sintered with the hereby described conditions. For these bi-material injected specimens, the temperature has been heated up to 1360 °C to activate fast sintering mechanisms, slightly lower than 1371~1398 °C corresponding to the melting point of 316L stainless steel powders.

Since the sintering time directly depends on the heating rate in a way, sintering tests with different heating rate have been carried out to analyze the influence of this factor. As above mentioned, a maximal temperature equal 1360 °C has been selected. The related sintering ramps are indicated in **Table 17**, and also illustrated in **Figure 74** to give a better description.

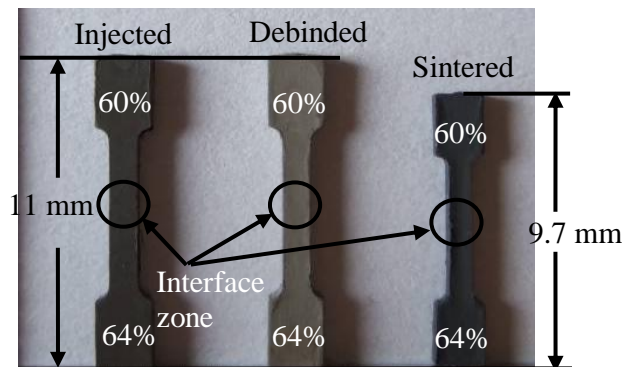
**Table 17.** Sintering ramps for specimens from bi-material injection

	Ramp 1	Ramp 2	Ramp 3
Heating rate [ °C/min]	10	20	-10
Temperature [ °C]	600	1360	20
Holding time [min]	30	120	End



**Figure 74.** Sintering cycle (1360 °C, 20 °C/min) for bi-material injected specimens

Firstly, the debinded components have been heated from ambient temperature up to 600 °C during nearly 120 min, then the temperature is maintained during 30 min; after that, the components one heated to 1360 °C with a heating rate equal 20 °C/min and a constant temperature during 120 min. Finally the cooling stage with a temperature rate equal -10 °C.min<sup>-1</sup> has been used for the components. As shown in **Figure 75**, the components are correctly sintered with no obvious defects appearing and no cracks near the interface between both different feedstocks, even along the interface zone (specified in **Figure 75** as well).



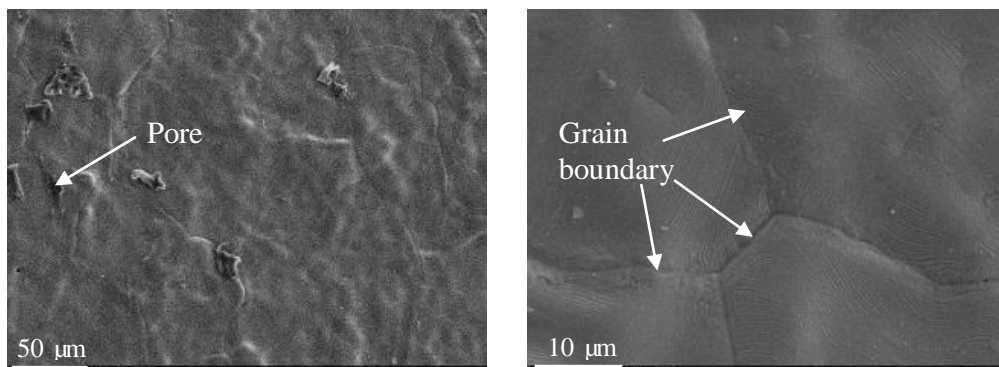
**Figure 75.** Beam-bending test specimens injected with two different feedstocks (60% for one half and 64% for the other half) after the injection, debinding and sintering stages

The sizes and dimensions of the final components have been measured using a microscope and compared with the geometry of the injected and debinded ones to analyze the shrinkage associated to debinding and sintering stage. The results (**Table 18**) indicate that significant shrinkages take place in the length direction for the components injected with the feedstocks loaded at 60% and 62% (12.07%); the other ones loaded at 60% and 64% exhibit over 10.94% shrinkage.

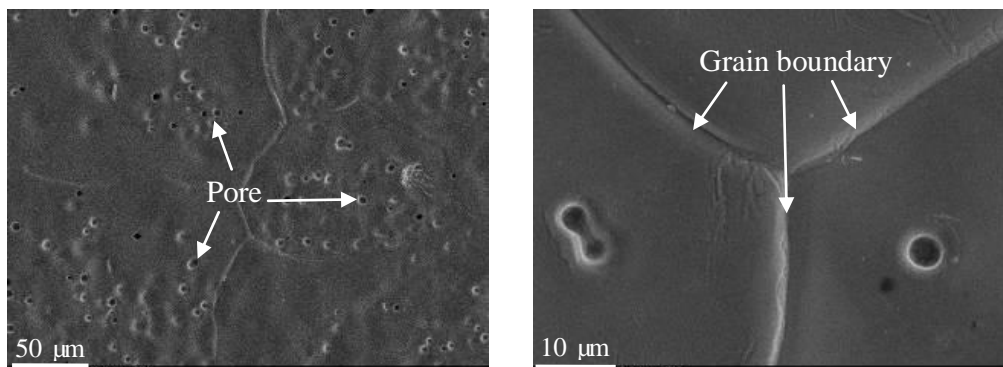
**Table 18.** Shrinkage in length direction of the beam-bending test specimens injected with 316L stainless steel feedstock ( $D_{50}=3.4\ \mu\text{m}$ , formulation F3, different powder volume loading)

Powder volume loading of the feedstock	Shrinkage in length direction
60%~62%	12.07%
60%~64%	10.94%

Afterwards, scanning electron micrographs have been carried out for the beam-bending test specimens (60%~64%) without polishing. Both sides of the same specimen have been observed and are related in **Figure 76** and **Figure 77**. The grain sizes have increased dramatically. Porosity has almost fully disappeared in the specimen half injected with powder volume loading of 60%, and the decrease in porosity in the half with powder volume loading of 64% has been clearly revealed as well, due to the elimination of pores via grain boundary and volume diffusion at high temperatures [124].



**Figure 76.** Scanning electron micrographs of the beam-bending test specimens (the half injected with powder volume loading of 60%) before polishing, almost no porosity is seen, the grain growth are observed



**Figure 77.** Scanning electron micrographs of the beam-bending test specimens (the half injected with powder volume loading of 64%) before polishing, the decrease in porosity and the grain growth are observed

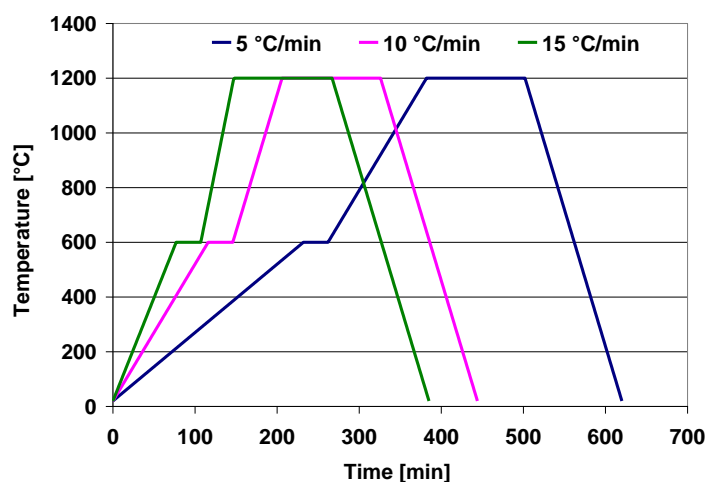
### 4.2.3. Sintering cycles for micro-injected specimens

Due to the decrease in size (especially the thickness) for the micro-injected components from the micro-injection with fine powder, the sintering temperature is no more obligate to be so high (as 1360 °C which has been used in our previous sintering for the bi-material injected specimens). So a temperature about 1250 °C [125] has been proposed in literature. Thus, instead of 1360 °C as the maximum peak during the sintering stage, for the micro mono-injected specimens, 1200 °C has been tested as adequate sintering temperature. The same primary vacuum has been used for this test.

Some investigations have been previously done in the literature, and they showed that the main parameters in sintering cycle are: heating rate, sintering time, sintering temperature and sintering atmosphere [126]. To study the influence of the heating rate, three different sintering cycles have been used in the analysis and three ramps have been included for each sintering cycle. **Table 19** and **Figure 78** give details about this sintering cycle. Ramp 1 corresponds the pre-sintering period, and the third ramp is to cool down the sintered compacts. The main sintering period is ramp 2 with the heating rate of 5 °C/min, 10 °C/min and 15 °C/min up to 1200 °C, the holding time at this temperature is still 120 min as before. In addition, still the same primary vacuum has been used during this sintering test.

**Table 19.** Sintering cycles for specimens from micro-mono-injection

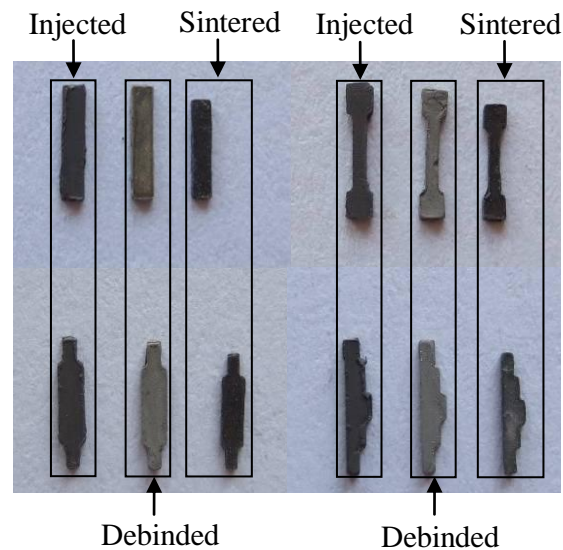
Sintering cycles		Ramp 1	Ramp 2	Ramp 3
<b>1</b>	Heating rate [ °C/min]	2.5	<b>5</b>	-10
	Temperature [ °C]	600	<b>1200</b>	20
	Holding time [min]	30	120	End
<b>2</b>	Heating rate [ °C/min]	5	<b>10</b>	-10
	Temperature [ °C]	600	<b>1200</b>	20
	Holding time [min]	30	120	End
<b>3</b>	Heating rate [ °C/min]	7.5	<b>15</b>	-10
	Temperature [ °C]	600	<b>1200</b>	20
	Holding time [min]	30	120	End



**Figure 78.** Sintering cycles (1200 °C) with three heating rates of 5 °C/min, 10 °C/min and 15 °C/min for mono-injected specimens

#### 4.2.4. Physical properties of the resulted micro-parts at the end of the processing stage

As the results suggest, four types of the micro specimen injected with 316L stainless steel feedstock ( $D_{50}=3.4 \mu\text{m}$ , formulation F3, powder volume loading of 60%, 62% and 64%) have been sintered. Taking the specimens loaded at 62% as an example, the resulting sintered specimens are shown in **Figure 79** without obvious defect.



**Figure 79.** Four types of micro specimens injected with 316L stainless steel feedstock ( $D_{50}=3.4 \mu\text{m}$ , formulation F3, powder volume loading is 62%) after the injection, debinding and sintering stages

##### 4.2.4.1. Shrinkages of the resulting micro-specimens in different directions

The analyses of the dimensions have been carried out to the sintered specimens injected with feedstock loaded at 62% and 64% respectively. The mean shrinkages in the main directions are related in **Table 20** and **Table 21**.




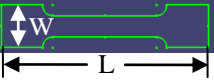
As shown by the results related to the feedstock loaded at 62%, the sintering cycle with the heating rate corresponding to  $10 \text{ }^{\circ}\text{C}/\text{min}$  generates the maximum shrinkages in L (9.6%) and W (10.4%) directions; in the thickness direction, the heating rate that indicates the maximum shrinkage (20.8%) is obtained at  $15 \text{ }^{\circ}\text{C}/\text{min}$ , which is much higher than the shrinkages in the other directions. In regard to the feedstock loaded at 64%, the sintering cycle with the heating rate of  $15 \text{ }^{\circ}\text{C}/\text{min}$  gives always the maximum shrinkages which are 10.3%, 11.9% and 20.9% in L, W and thickness directions, respectively.

One can remark that a very high shrinkage in thickness direction has also been revealed as for the feedstock loaded at 62%. Compared with the shrinkage in L direction for both feedstocks, higher values have been achieved in W direction for three heating rates. The same phenomenon has been encountered by other authors, N.H. Loh et al. [127]. The main parameters affecting final part size have been already



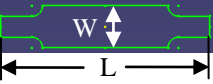



studied and these include the metal powder morphology, binder ingredients and proportions, mixing conditions, mold design, molding parameters, rheological behavior of the molding materials, debinding, sintering, equipment and even environmental conditions. Among these often integrally-related factors, the most sensitive are the powder volume loading and the mold design [127]. As it is shown, different shrinkages have been revealed for the same directions for the different specimen types, since all the conditions during the process are the same, these differences in our experiments can only be explained by the different mold design corresponding to the specimen types.

**Table 20.** Shrinkage in different directions corresponding micro specimen injected with 316L stainless steel feedstock ( $D_{50}=3.4\ \mu\text{m}$ , formulation F3, powder volume loading is 62%)

Direction	Heating rate [ °C/min]	Type a) 	Type b) 	Type c) 	Type d) 	Mean value
<b>L</b>	5	9.6%	9.4%	9.4%	9.2%	9.4%
	10	9.9%	10.1%	8.4%	9.9%	9.6%
	15	8.5%	9.3%	9.0%	9.4%	9.1%
<b>W</b>	5	10.0%	11.0%	10.2%	10.0%	10.3%
	10	12.0%	11.0%	9.6%	9.1%	10.4%
	15	8.0%	9.3%	10.7%	9.0%	9.3%
<b>Thickness</b>	5	18.0%	16.0%	24.0%	16.0%	18.5%
	10	16.0%	22.0%	22.0%	16.0%	19.0%
	15	19.6%	19.5%	24.0%	20.0%	20.8%

**Table 21.** Shrinkage in different directions corresponding micro specimen injected with 316L stainless steel feedstock ( $D_{50}=3.4\ \mu\text{m}$ , formulation F3, powder volume loading is 64%)

Direction	Heating rate [ °C/min]	Type a) 	Type b) 	Type c) 	Type d) 	Mean value
<b>L</b>	5	10.1%	10.4%	10.2%	9.8%	10.1%
	10	9.6%	9.5%	9.3%	9.3%	9.4%
	15	10.9%	10.2%	9.6%	10.4%	10.3%
<b>W</b>	5	9.8%	10.9%	11.3%	9.0%	10.3%
	10	10.0%	10.0%	12.0%	10.0%	10.5%
	15	9.5%	13.0%	13.0%	12.0%	11.9%
<b>Thickness</b>	5	16.0%	20.0%	24.0%	22.0%	20.5%
	10	16.0%	18.0%	20.0%	20.0%	18.5%
	15	22.2%	16.0%	26.0%	19.4%	20.9%

As we know, a low powder volume loading results in considerable dimensional change during the sintering stage in comparison with a high powder volume loading [2]. However, in some cases one can observe that the related results are in the opposite way. Thus, more tests should be carried out to examine this problem.



#### 4.2.4.2. Densities of the resulting micro-specimens

In addition, the density of the sintered micro-specimens have been measured by the water displacement method (Archimedes method) for feedstocks loaded at 62% and 64%, as it is reported in **Table 22**.

**Table 22.** Density of the sintered micro-parts resulting from 316L stainless steel feedstock ( $D_{50}=3.4 \mu\text{m}$ , formulation F3)

Powder volume loading	Heating rate [°C/min]	Density [ $\text{g/cm}^3$ ]	Relative density
62%	5	7.37	92.8%
	10	7.51	95.1%
	15	7.21	91.3%
64%	5	7.26	91.9%
	10	7.31	92.5%
	15	7.48	94.7%

#### 4.2.4.3. Vickers hardness of the micro-specimens

Besides measurements of shrinkages and densities of the sintered micro-specimens, Vickers hardness tests have been also used to evaluate the resulting mechanical properties. Since the four types of micro-specimens have been employed for the measurements before post-treatment (e.g. quenching, etc), a relative low average value of HV/160 has been observed.

### Summary

The micro-components in this chapter are the beam-bending test specimens injected with two 316L stainless steel feedstock (60% as the powder volume loading for one half and 64% for the other half) and the four types of the micro specimen injected 316L stainless steel feedstock ( $D_{50}=3.4 \mu\text{m}$ , formulation F3, powder volume loading is 60%).

For the thermal debinding stage, a classical cycle with two ramps has been used for these beam-bending test specimens in an argon atmosphere. About 70% to 75% of the binders are removed out without generating external defects for the debinded porous components. The debinded structures (e.g. for the injected with 316L stainless steel feedstock loaded at 62% and 64%) have been observed as well.

The debinded porous specimens are then sintered and the final specimens have been finally produced. A sintering cycle with a heating rate of 20 °C/min till 1360 °C has been processed on the beam-bending test specimens obtained from bi-material injection. The shrinkages in length direction for the bi-material injected specimen are 12.07% (specimens injected with feedstocks loaded at 60% and 62%) and 10.94% (specimens injected with feedstocks loaded at 60% and 64%). For the micro mono-injected specimens,

The shrinkages in length, width and thickness directions of the micro mono-injected specimens have been measured, one can notice smaller shrinkages in length directions (with an average value of about 11.5%) than in width directions (with an average value of about 13.2%) attributed to the mold design influence.

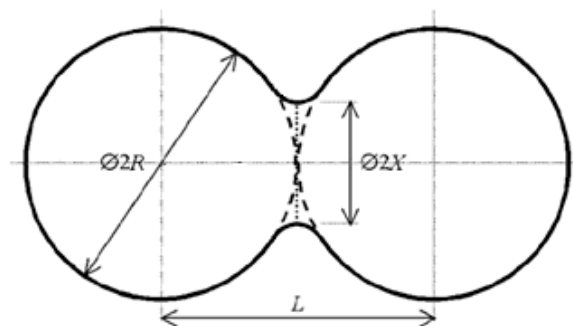
## Chapter 5. Identification of constitutive material parameters and numerical simulation of the sintering stage in micro-MIM

In comparison with the conventional trial and error method, computer simulation of sintering by finite element method in combination with appropriate material laws is a faster alternative to optimize entire industrial processes [128].

The objective of this chapter is the shrinkage and density calculation of the components form micro-injection obtained from the previous stages. In the first stage, the identification of constitutive behavior law and physical parameters concerning the very fine stainless steel powders and high volume loading contents involved in the sintering model should be performed in order to set up the implementation of the FE simulations. The identifications are carried out with Matlab<sup>®</sup>, and the identified parameters are presented. Then the solid state diffusion model for the sintering has been implemented in a commercial FE solver (ABAQUS<sup>®</sup>) as a user supplied material routine (UMAT) to perform the simulation of the sintering stage for micro-MIM process. Finally, the simulation results are related for the four specimen types and compared with the experimental results to validate the simulations of the micro-injected components.

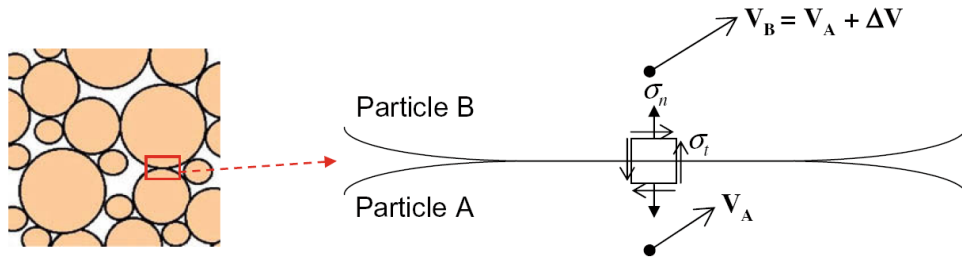
### 5.1. Constitutive sintering model

Sintering theory has been developed continuously from the late 1940s [128]. The most successful approaches to understand the mechanisms of neck growth and shrinkage is the two-sphere model due to Frenkel and Kuczynski [129] for the early sintering stages whereby the particles bond together by the neck which forms where the powder particles were initially touching, as shown in **Figure 80**. As temperature increases during the sintering process, the neck speeds up to grow [130].



**Figure 80.** Neck formation in the sintering of spherical particles of the same size with a neck

The cylindrical pore channel model is due to Coble [131] and the extrapolated two-particle model due to Kingery and Berg [132] for the intermediate shrinkage state, and the spherical pore model due to MacKenzie and Shuttleworth [133] for the late sintering stages have been proved correctly as well. In the seventies, more sophisticated models (based on less simplified pore geometries and taking superposition of the various sintering mechanisms into account) have been developed, for example, by Johnson [134], Skorokhod [135], Ashby [136], Beere [137], Scherer [138], among many others (for reviews see, for example, Exner et al. [139] [140] [141] [142], Schatt [143], German [47] or Olevsky [144]). A similar development took place in solid-liquid phase sintering theory, where the early model due to Kingery [145], has been the starting point for most of later and still ongoing theoretical work in spite of its geometric over simplifications and its lack of qualitative agreement with experimental observations. Extensive reviews on sintering models for liquid phase sintering are available (see, e.g. German [146], Schatt [143], Savitskii [147] or Exner and Arzt [141]). Later theoretical work on solid and liquid state sintering considering additional effects like non-isothermal sintering, gravity, particle orientation, anisotropic shrinkage [148], or superposition of external loads have been carried out. In addition, sintering theory was also applied to new sintering processes like microwave sintering [149]. Moreover, a microscopic model for viscous sintering has been adopted by A. Mawardi et al. to describe the micro/nano-structural evolution by considering the effects of nano-particle mechanics on the sintering kinetics [150]. The overall dimensional change of the sintered micro-part is determined based on the local sintering stress in the green body, which is evaluated using the variation of the micro/nanostructure during sintering, as shown in **Figure 81**, where the sintering stress  $\sigma_s$  is formulated based on the mechanism of diffusion at the interparticle boundary for two spherical particles in contact.



**Figure 81.** Diagrammatic sketch of interparticle boundary for the determination of sintering stress in the microscopic scale

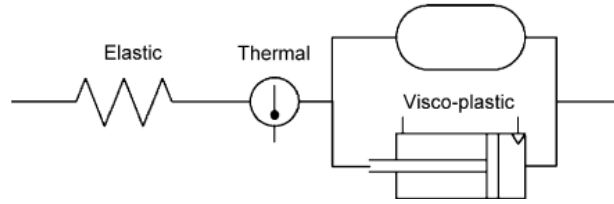
One can find a schematic illustration of an interparticle boundary across which a velocity discontinuity occurs, where the stresses,  $\sigma_n$  and  $\sigma_t$  are defined such that positive velocity differential results in positive work. The details of the formulation of mass transport on the interparticle boundary are reported in reference [151]. The deformation of the particle can be derived based on the quasistatic principle of virtual power, in the following form:

$$\sigma_s \int_A n_i v_i^* dA + \int_{L_p} \sigma_n m_i j_i^* dL = 0 \quad (12)$$

where  $v$  is the velocity,  $A$  is the surface area of particle,  $j^*$  is the diffusion flux, and  $\sigma_n$  is the stress on  $L_p$  (contact perimeter), while  $m$  and  $n$  are the unit normal vectors, for the  $i$ th plane of contact.

Recently, it has been increasingly possible to perform simulation of the micro-structural behavior of large systems, and this development opens the way for embedding micro-structural evolution into macroscopic models [152], which in turn allowed plasticity models to move beyond continuum phenomenological theories that rely on field quantities to approximate collective micro-structural phenomena [153] [154] [155] [156]. Some numerical researches have been realized on the micro-behavior during the sintering process of the alumina [157] [158].

The model chosen in our study is a phenomenological one based on the continuum mechanics, by considering a thermo-elasto-viscoplastic model (as shown in **Figure 82**) with isotropically distributed voids [159], in order to estimate shrinkage, relative density and variation of the shapes of micro-components, during and after the sintering stage without being obliged to carry out the physical experiments [72] [82] [160].



**Figure 82.** Sketch of the employed sintering model in our investigations

Under high sintering temperature conditions, the macroscopic behavior of the material can be regarded as a creep deformation one [161] [162] [163]. The total strain  $\varepsilon$  of this model is described as expressed in equation (13), consisting to split the strain rate in three parts [159].

$$\dot{\varepsilon} = \dot{\varepsilon}^e + \dot{\varepsilon}^{th} + \dot{\varepsilon}^{vp} \quad (13)$$

where  $\dot{\varepsilon}^e$ ,  $\dot{\varepsilon}^{th}$  and  $\dot{\varepsilon}^{vp}$  are the elastic, thermal and viscoplastic strain rates.

The part of elastic strain rate is assumed to be linear and isotropic. It can be expressed in the following expression:

$$\dot{\varepsilon}^e = C_e \dot{\sigma} \quad (14)$$

where  $C_e$  is the elastic compliance matrix. Equation (14) can also be expressed in the rate form of Hooke's law, as following:

$$\dot{\sigma} = D^e \dot{\varepsilon}^e = D^e (\dot{\varepsilon} - \dot{\varepsilon}^{th} - \dot{\varepsilon}^{vp}) \quad (15)$$

where  $D_e$  is elastic stiffness matrix.

The thermal strain is mainly due to thermal expansion that can be expressed as:

$$\dot{\varepsilon}^{th} = \alpha \Delta T \dot{I} \quad (16)$$

where  $\alpha$  is the thermal expansion coefficient,  $\Delta \dot{T}$  is the incremental temperature rate,  $\mathbf{I}$  is second order identity tensor.  $\alpha$  can be determined by the experiments carried out in dilatometer.

After overcoming a specified transition temperature in sintering, viscoplastic strains prevail on elastic strains and densification occurs. The viscoplastic strain rate is given by equation (17) [160]:

$$\dot{\epsilon}^{vp} = \frac{dev(\sigma)}{2G} + \frac{\sigma_m - \sigma_s}{3K} \mathbf{I} \quad (17)$$

where  $\dot{\epsilon}^{vp}$  is the viscoplastic strain rate,  $dev(\sigma)$  is the deviatoric stress tensor,  $\sigma_m = tr(\sigma)/3$  is the trace of the stress tensor,  $\mathbf{I}$  is the second order identity tensor,  $G$  is the shear viscosity modulus,  $K$  is the bulk viscosity modulus,  $\sigma_s$  is the sintering stress.  $G$ ,  $K$  and  $\sigma_s$  stand for the material parameters to be determined. This strain rate is function of temperature, density and relative density of pores [164] [165]. The material is considered a porous media in which the total relative density  $\rho$  (summation of the relative densities of powder, binder and pores, defined as the volume fraction of the constituent divided by the entire volume) is constant (equal to 1) during the entire process while the relative densities of each component continuously change [8].

The elastic-viscous analogy is suggested to define the shear and bulk viscosity modules for sintering materials, as related in equation [166]:

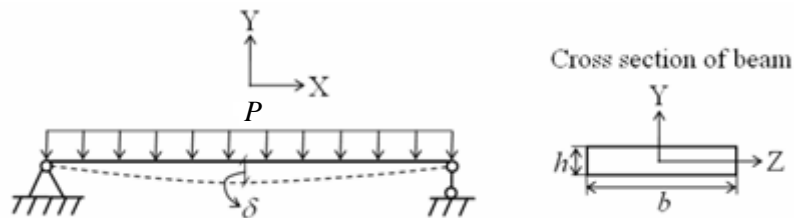
$$G = \frac{\eta_p}{2(1 + \nu_p)}, \quad K = \frac{\eta_p}{3(1 - 2\nu_p)} \quad (18)$$

where  $\eta_p$  and  $\nu_p$  are uniaxial viscosity and viscous Poisson's ratio of the porous material.

As shown in **Figure 83**, Song et al. have defined the following relationship to define the uniaxial viscosity  $\eta_p^e$  through bending tests [72] [160] [167]:

$$\eta_p^e = \frac{1}{\dot{\delta}} \left( \frac{5\rho_a g L_s^4}{32h^2} + \frac{PL_s^3}{4bh^3} \right) \quad (19)$$

where  $\dot{\delta}$  is the deflection rate at the center of the specimen,  $\rho_a$  is the apparent density,  $g$  is gravity,  $P$  is the external load,  $L_s$ ,  $b$  and  $h$  are respectively the distance between the two supporting rods and the width and thickness of the specimen.



**Figure 83.** Simply supported beam model for beam-bending tests

The viscous Poisson's ratio is determined from an average relationship in the following form [166]:

$$v_p \approx \frac{1}{2} \sqrt{\frac{\rho}{3-2\rho}} \quad (20)$$

where  $\rho$  is the relative density. The relative density of the sintered part is calculated by the following expression:

$$\rho = \frac{\rho_0}{(1+\lambda)^3} \quad (21)$$

where  $\rho_0$  is the relative density after pre-sintering and  $\lambda$  is the uniaxial shrinkage defined as:

$$\lambda = \frac{L - L_0}{L_0} \quad (22)$$

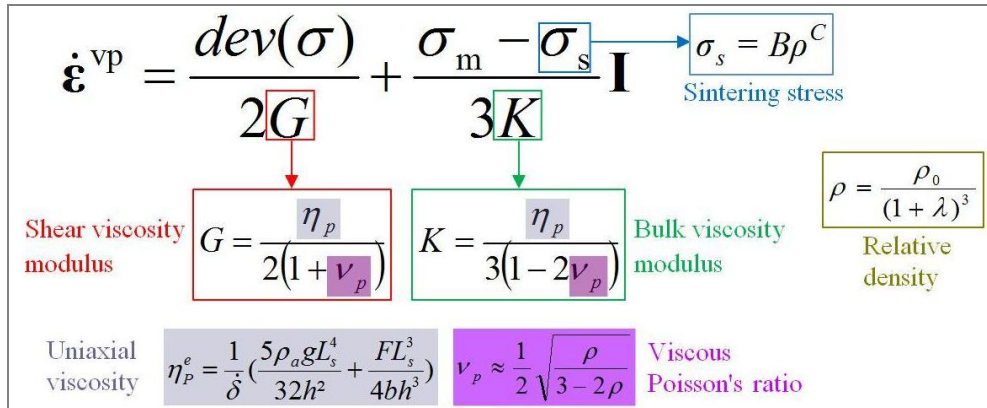
where  $L$  and  $L_0$  are the length of the specimens before and after sintering stage.

The following equation is proposed to determine the sintering stress [168]:

$$\sigma_s = B\rho^C \quad (23)$$

where  $B$  and  $C$  are the material parameters that should be identified from dilatometer experiments.

The above evaluation is summarized in **Figure 84**, the material parameters can be determined by identifying the shear viscosity module  $G$ , the bulk viscosity module  $K$  and the sintering stress  $\sigma_s$ . Extensive numerical simulations have been done for the small size components injected with a 316L stainless steel feedstock provided by AMW in our laboratory by Song et al. [160]. Besides, the components injected with some in-house feedstocks based on the powder with larger particle size (powder volume loading equal 60%) have been also simulated.



**Figure 84.** Evaluation of the viscoplastic strain rate in the sintering model

## 5.2. Sintering parameters identification

The beam-bending test process has been proposed to identify the sintering parameters for the sintered parts during the sintering stage at high temperature [169]. In our laboratory, Song et al. have carried out

the beam-bending tests specimens for the components (80mm in length) in a furnace [167]. Quinard et al. have performed identifications through the horizontal dilatometer equipped with a beam-bending test support for the components with the length of 25mm [170].

The vertical dilatometer has been intensively used for the identification in the present study. The 316L stainless steel feedstocks ( $D_{50}=3.4 \mu\text{m}$ , formulation F3) with high powder volume loadings (62%, 64% and 66%) have been identified here. As the deflection direction is vertical, so the influence of the gravity has been considered in these identification tests in the vertical dilatometer with primary vacuum for the micro-MIM process with the very fine powder.

### 5.2.1. Identification tests in vertical dilatometer

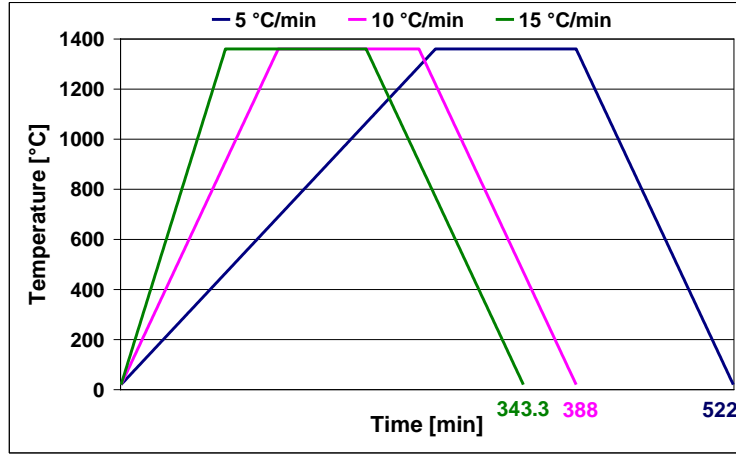
To succeed in the sintering stage, high sintering temperature and fast heating rate have been applied. However, fast heating can induce various defects in the sintered components [122], such as crack and distortion due to the stress and temperature gradients. It results in some difficulties to determine the sintering parameters and to choose the appropriate design of the injection mold. Thus, in the identification tests in the vertical dilatometer, three heating rates (as shown in **Table 23**) with the equal  $5 \text{ }^{\circ}\text{C}/\text{min}$ ,  $10 \text{ }^{\circ}\text{C}/\text{min}$  and  $15 \text{ }^{\circ}\text{C}/\text{min}$  have been used to correspond the heating rates employed in the sintering stage for the micro-injected specimens (see section 4.2.3). **Figure 85** illustrates the three cycles used in the analyses.

**Table 23.** Different sintering cycles for the identification tests in vertical dilatometer

Sintering cycles		Ramp 1	Ramp 2
1	Heating rate [ $^{\circ}\text{C}/\text{min}$ ]	5	-10
	Temperature [ $^{\circ}\text{C}$ ]	1360	20
	Holding time [min]	120	End
2	Heating rate [ $^{\circ}\text{C}/\text{min}$ ]	10	-10
	Temperature [ $^{\circ}\text{C}$ ]	1360	20
	Holding time [min]	120	End
3	Heating rate [ $^{\circ}\text{C}/\text{min}$ ]	15	-10
	Temperature [ $^{\circ}\text{C}$ ]	1360	20
	Holding time [min]	120	End

Considering the main densification of 316L stainless steel powder occurs from above  $900 \text{ }^{\circ}\text{C}$ , the pre-sintering stage has been omitted to simplify the sintering cycles. The temperature in the vertical dilatometer has been raised up to  $1360 \text{ }^{\circ}\text{C}$  due to the fact that sintering stage with higher temperature will be also simulated in the future. Since the 316L stainless steel powder in our study is an easy-oxidized powder, so during the identification tests in vertical dilatometer, an argon atmosphere has been used to protect them. The same pre-sintering stage as in the identification tests in horizontal dilatometer has been also carried out for the specimens in the vertical dilatometer. Consequently, the mechanical properties of the pre-sintered specimens are improved.

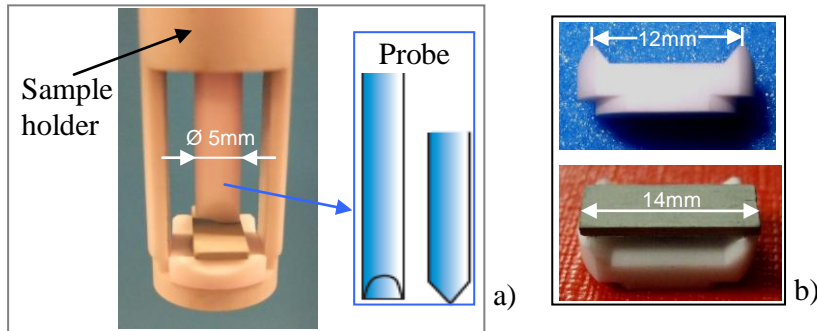




**Figure 85.** Heating cycles for beam-bending and free sintering test in vertical dilatometer

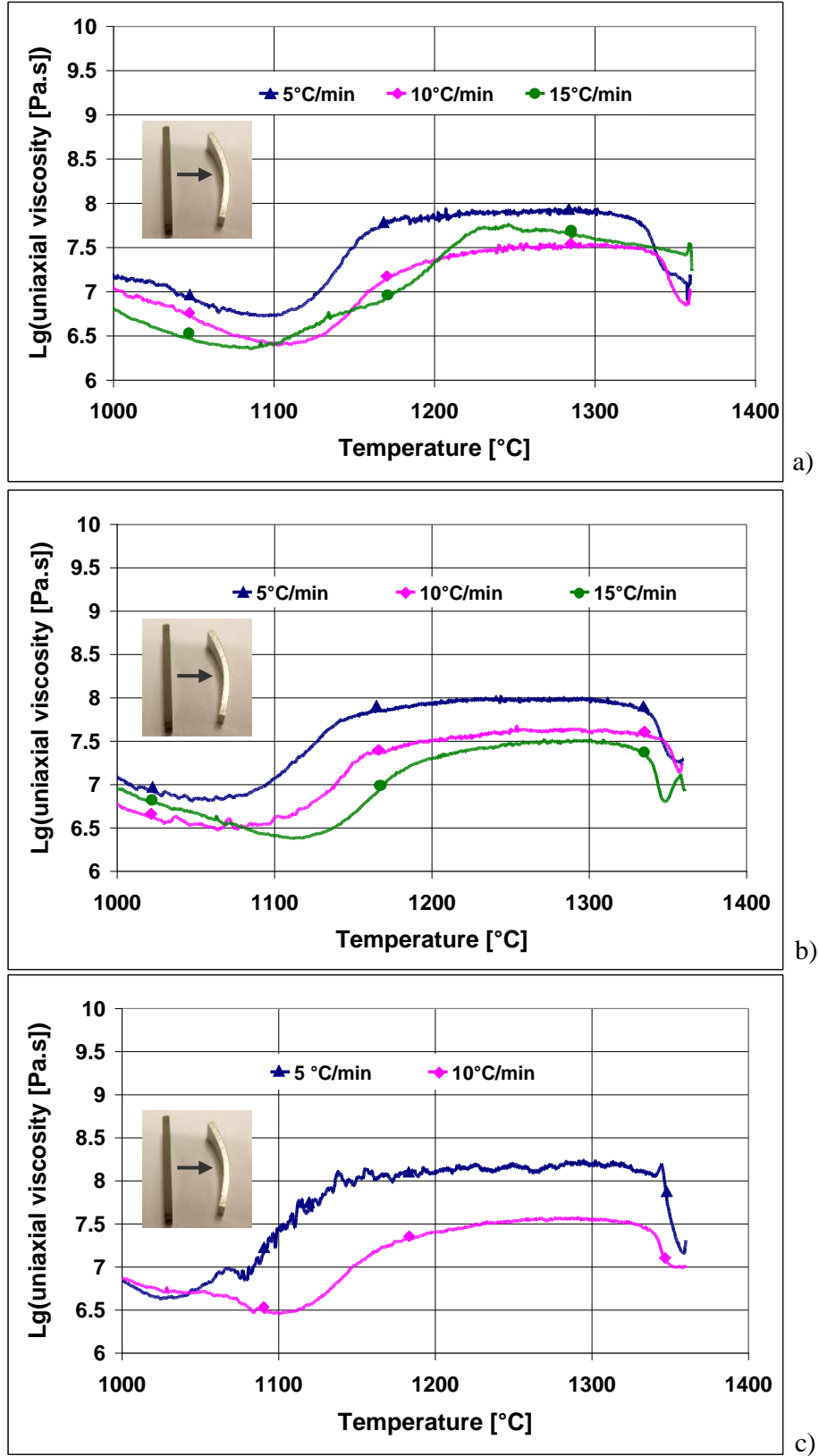
#### 5.2.1.1. Beam-bending tests in vertical dilatometer

The set-up used for the beam-bending tests in the vertical dilatometer is demonstrated in **Figure 86**. The associated probe is made up of a base with two knives and a rod with a knife-shaped cross section. A load equal 5 cN has been applied at the centre of the specimen through the rod. The specimens have a rectangular shape (14 mm in length, 5.5 mm in width and 1 mm in thickness).



**Figure 86.** Beam-bending test in vertical SETSYS® evolution dilatometer, a) Set-up for TMA measurement and the involved probe; b) geometry of the sample and the sample support

Since gravity has been taken into account, the uniaxial viscosities  $\eta_p^e$  have been evaluated according to equation (17) and related in **Figure 87** with the rectangular specimens before and after tests. Due to the difficulty of the injection with the feedstock loaded at 66%, as small number of specimens has been manufactured. As the consequence, the beam-bending and free sintering tests with heating rate of 15 °C/min have not been carried out for this feedstock.



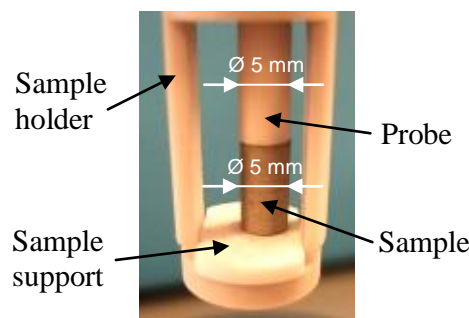
**Figure 87.** Uniaxial viscosities  $\eta_p^e$  vs. temperature from beam-bending tests in vertical dilatometer for 316 L stainless steel feedstock ( $D_{50}=3.4 \mu\text{m}$ , formulation F3) with the powder volume loadings equal a) 62%; b) 64%; c) 66%

Based on the results obtained from these tests, the following synthesis can be related:

- 1) The uniaxial viscosities are in the range 0.1-0.3 GPa.s for 316L stainless steel powders. However Blaine [169] got values of uniaxial viscosity in the range 0.2-0.6 GPa.s for 316L stainless steel powders compacted with boron. Lamé [171] reported values of uniaxial viscosity in the range 60-80 GPa.s for iron powder compacts. Vagnon [172] related the uniaxial viscosity of 316L stainless steel powders compacts in the range 4-50 GPa.s. The differences between the results reported by Blaine [169] and Lamé [171] can be explained through numbers of parameters as homogeneity of the feedstock, the content of the binder, the particle size of the powder, etc.
- 2) The powder materials under consideration begin to flow when the temperature is greater than 1000 °C, which confirms well the results obtained by different authors.
- 3) The feedstock loaded from 62% to 66%, exhibits greater uniaxial viscosities equals about 8 GPa.s at the lower heating rate of 5 °C/min. One has to remark that for the feedstock loaded at 62%, the uniaxial viscosity exhibits an abrupt increase at about 1225 °C for heating rate equal 15 °C/min.
- 4) One can remark that with the same heating rate, the higher the feedstocks are loaded, the higher uniaxial viscosities are obtained at the same temperature. This is related to the fact that the more the powder loading is, the higher the related viscosity becomes.

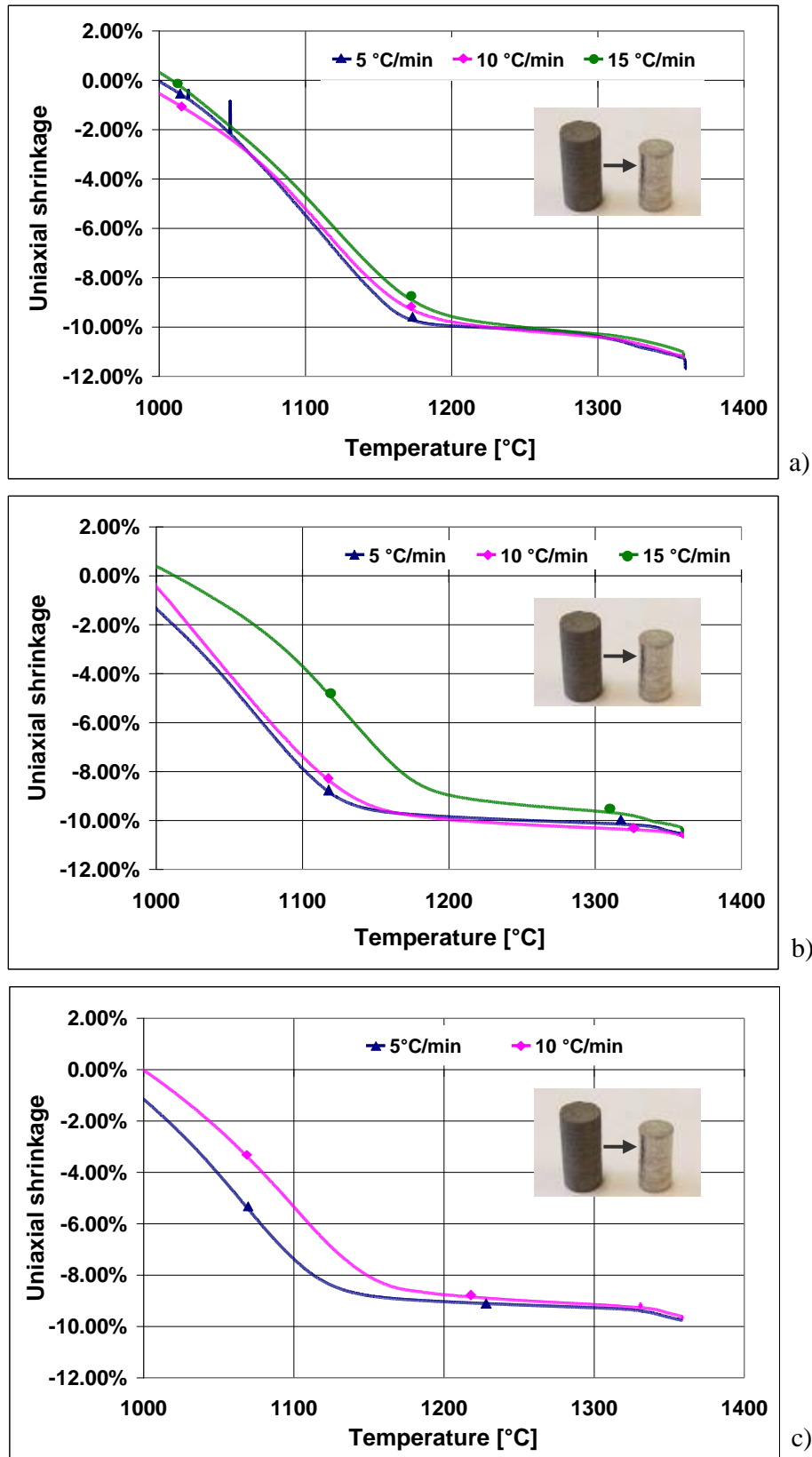
#### 5.2.1.2. Free sintering tests in vertical dilatometer

**Figure 88** indicates the set-up for free-sintering test in vertical dilatometer. The length of the cylindrical specimens is 10 mm and the diameter is 5 mm. The rod has a flat end and the base is also flat.



**Figure 88.** Set-up for free-sintering test in vertical SETSYS<sup>®</sup> evolution dilatometer

The shrinkage curves vs. different sintering temperatures for the different loaded feedstocks have been observed and plotted in **Figure 89**, and the involved cylindrical specimens in these free-sintering tests have been given as well.



**Figure 89.** Uniaxial shrinkage  $\lambda$  vs. temperature from free sintering test in vertical dilatometer for 316 L stainless steel feedstock (D<sub>50</sub>=3.4 μm, formulation F3) with the powder volume loading of a) 62%; b) 64%; c) 66%

According to these curves, the following conclusions can be set up:

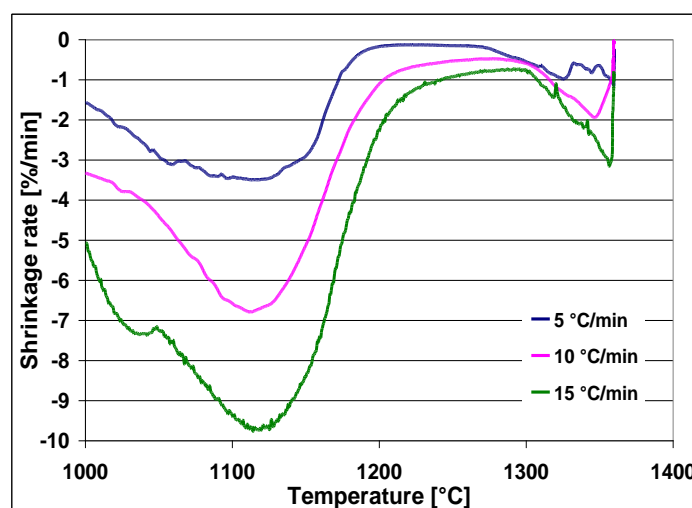
- 1) Shrinkage begins to occur at about 1000 °C and rapidly increase at a temperature above 1050 °C till around 1200 °C, then after and up to a temperature approaching to 1360 °C and the shrinkage largely decreases.
- 2) At the same temperature, large shrinkages are obtained for the specimens with lower powder loading. The reason is related to the fact that when powder loading is high, more pores are produced, so the components after sintering shrink more obviously.
- 3) A higher density was obtained using low heating rate since a greater shrinkage was obtained. The density investigation after the sintering stage has been performed on the sintered specimens.

As example, considering the feedstock loaded at 64%, as reported in **Table 24**, the rise of density in accordance with the drop of the heating rate has been clearly presented. In comparison with the lower heating rate, less time has been left to the components to shrink during the sintering stage with rapid heating.

**Table 24.** Density and shrinkage of 316 L stainless steel feedstock ( $D_{50}=3.4\ \mu\text{m}$ , formulation F3, powder volume loading is 64%) after sintering stage with three different heating rates

Heating rate, °C/min	Density, g.cm <sup>-3</sup>	Shrinkage
5	7.618	12.51 %
10	7.593	12.26 %
15	7.567	12.20 %

Besides, the shrinkage rates during these free sintering tests in the vertical dilatometer have been measured as well, always the same temperature about 1180 °C (see **Figure 90**) has been revealed as the highest shrinkage rates occur for all the three powder volume loadings. And it is can be seen that the shrinkage rates increase as the heating rates rise up.



**Figure 90.** Shrinkage rate during the free sintering test in vertical dilatometer for 316 L stainless steel feedstock ( $D_{50}=3.4\ \mu\text{m}$ , formulation F3) with the powder volume loading of 62%

### 5.2.2. Numerical identification of the sintering model

As discussed in section 5.1, the shear viscosity module  $G$ , bulk viscosity module  $K$  and sintering stress  $\sigma_s$  should be determined to identify the employed sintering model based on the results from the identification tests mentioned previously. Matlab<sup>®</sup> and the related tools are used for this.

#### 5.2.2.1. Numerical identification of $B$ and $C$ parameter

Sintering stress is the driving force for densification. It depends on the surface tension, relative density, size and shape of the particles, as well as the grain and pore size that varies with the microstructure evolution during the sintering process. As discussed above (in section 5.1), parameter  $B$  and  $C$  in sintering model (equation (23)) are the material parameters that should be identified from dilatometric experiments.

##### 5.2.2.1.1. Algorithm in Matlab<sup>®</sup> for identification of parameter $B$ and $C$

Different expressions are proposed to calculate the sintering stress for the open and closed pores [173] [174]. The following equation (24) has been proposed to calculate the sintering stress for 316L stainless steel powder during the sintering stage [160].

$$\frac{\dot{L}}{L} = \alpha \dot{T} - \frac{1}{3K_p} \sigma_s \quad (24)$$

By coupling the equation (23), equation (24) can be expressed as:

$$\frac{B\rho^C}{K} = 3\left(\alpha \dot{T} - \frac{\dot{L}}{L}\right) \quad (25)$$

where  $\dot{L}$  is the dimensional change of the specimen,  $\alpha$  is the coefficient of thermal dilatation,  $\dot{T}$  is the variation rate of temperature. The strategy to identify the parameters  $B$  and  $C$  in Matlab<sup>®</sup> is to approach the numerical shrinkage curve according to equation (26) to the one obtained from the free sintering tests. The algorithm is indicated in the following expression [160]:

$$\begin{cases} \min F(x) \\ F(x) = \sum_{i=1}^n \left| \lambda^m(T_i, x) - \lambda^e(T_i, x) \right|^2 \\ x = [B, C] \end{cases} \quad (26)$$

where  $\lambda^e$  is experimental uniaxial shrinkage, obtained from dilatometer test,  $\lambda^m$  is numerical uniaxial shrinkage,  $F(x)$  is the mean residual squares of the tolerance where  $i=1, \dots, n$  indicates different values of the sintering temperature,  $x$  is the set of material parameters to be identified. The Nelder-Mead

Simplex method [175] has been employed to minimize the value of  $F(x)$  in our case. Note that the calculations have been divided into two segments specified by critical relative density (0.8) during the sintering stage due to the different shrinkage rates for each one.

5.2.2.1.2. *B and C identified for 316L stainless steel feedstock with the powder volume loading of 62%, 64% and 66%*

In accordance, by coupling the shrinkages obtained from the identification tests in vertical dilatometer, the identification of B and C parameters during the sintering stage with three different heating rates of 5 °C/min, 10 °C/min and 15 °C/min have been implemented for the 316L stainless steel feedstock loaded at 62%, 64% and 66% and the identified values are indicated in **Table 25**, **Table 26** and **Table 27**, respectively.

**Table 25.** Identified  $B$  and  $C$  during sintering stage with different heating rates for 316 L stainless steel feedstock ( $D_{50}=3.4 \mu\text{m}$ , formulation F3, powder volume loading is 62%)

Heating rate	$\rho < 0.8$		$\rho \geq 0.8$	
	$B_1$	$C_1$	$B_2$	$C_2$
5 °C/min	6501.7	5.2478	2482.9	-5.4275
10 °C/min	1114.0	0.0504	1528.9	-6.3254
15 °C/min	6756.4	4.6458	1696.2	-8.7859

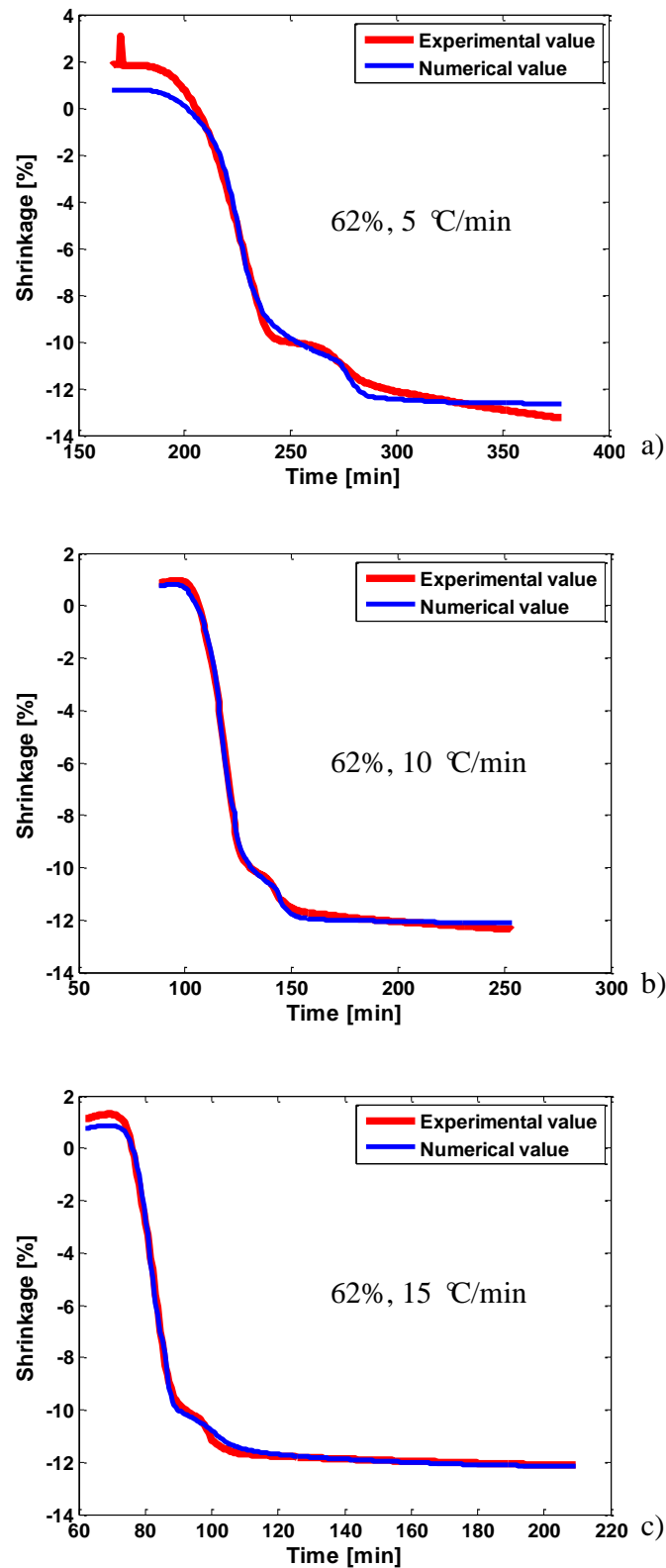
**Table 26.** Identified  $B$  and  $C$  during sintering stage with different heating rates for 316 L stainless steel feedstock ( $D_{50}=3.4 \mu\text{m}$ , formulation F3, powder volume loading is 64%)

Heating rate	$\rho < 0.8$		$\rho \geq 0.8$	
	$B_1$	$C_1$	$B_2$	$C_2$
5 °C/min	7147.2	5.2287	852.3	-10.407
10 °C/min	3982.8	3.3489	3094.3	1.2225
15 °C/min	6169.3	4.6355	207.5	-23.273

**Table 27.** Identified  $B$  and  $C$  during sintering stage with different heating rates for 316 L stainless steel feedstock ( $D_{50}=3.4 \mu\text{m}$ , formulation F3, powder volume loading is 66%)

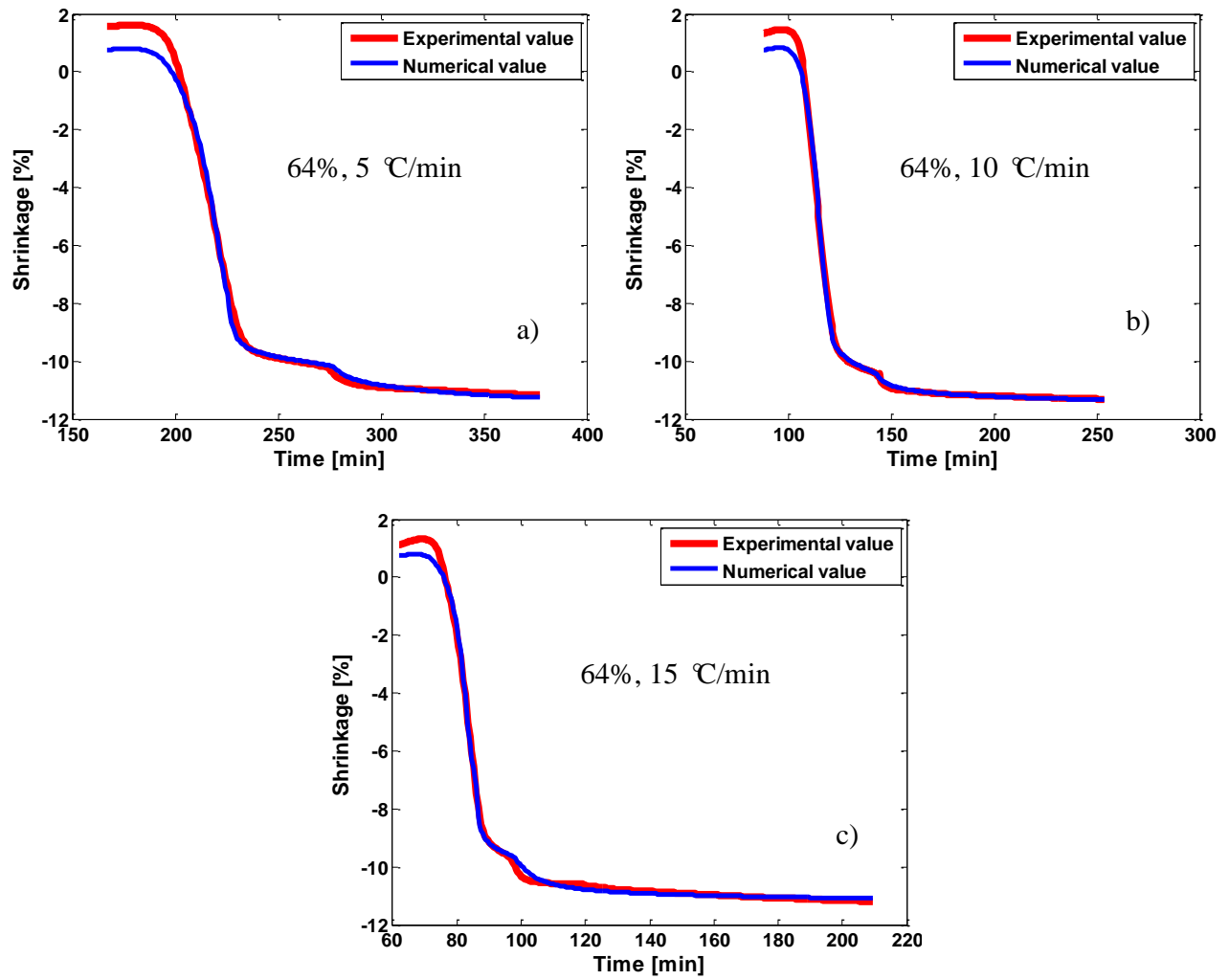
Heating rate	$\rho < 0.8$		$\rho \geq 0.8$	
	$B_1$	$C_1$	$B_2$	$C_2$
5 °C/min	3090	3.728	2435.9	-6.1662
10 °C/min	5696.6	4.9671	1814.1	-1.7039

The numerical shrinkage curves after identification are related in **Figure 91**, **Figure 92** and **Figure 93**. As it is shown for the three different heating rates, all the numerical curves fit well the experimental ones; these results have confirmed very well the choice of our sintering stress model and the identification method.

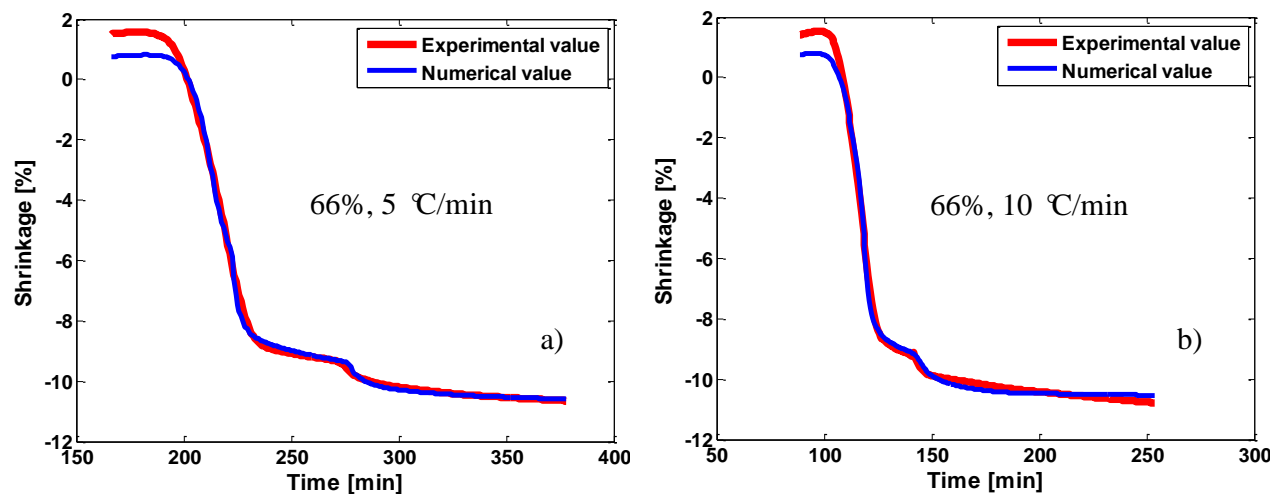


**Figure 91.** Comparison between experimental shrinkages in vertical dilatometer during the sintering stages with different heating rates and identified ones for 316 L stainless steel feedstock (D<sub>50</sub>=3.4 μm, formulation F3, powder volume loading is 62%)



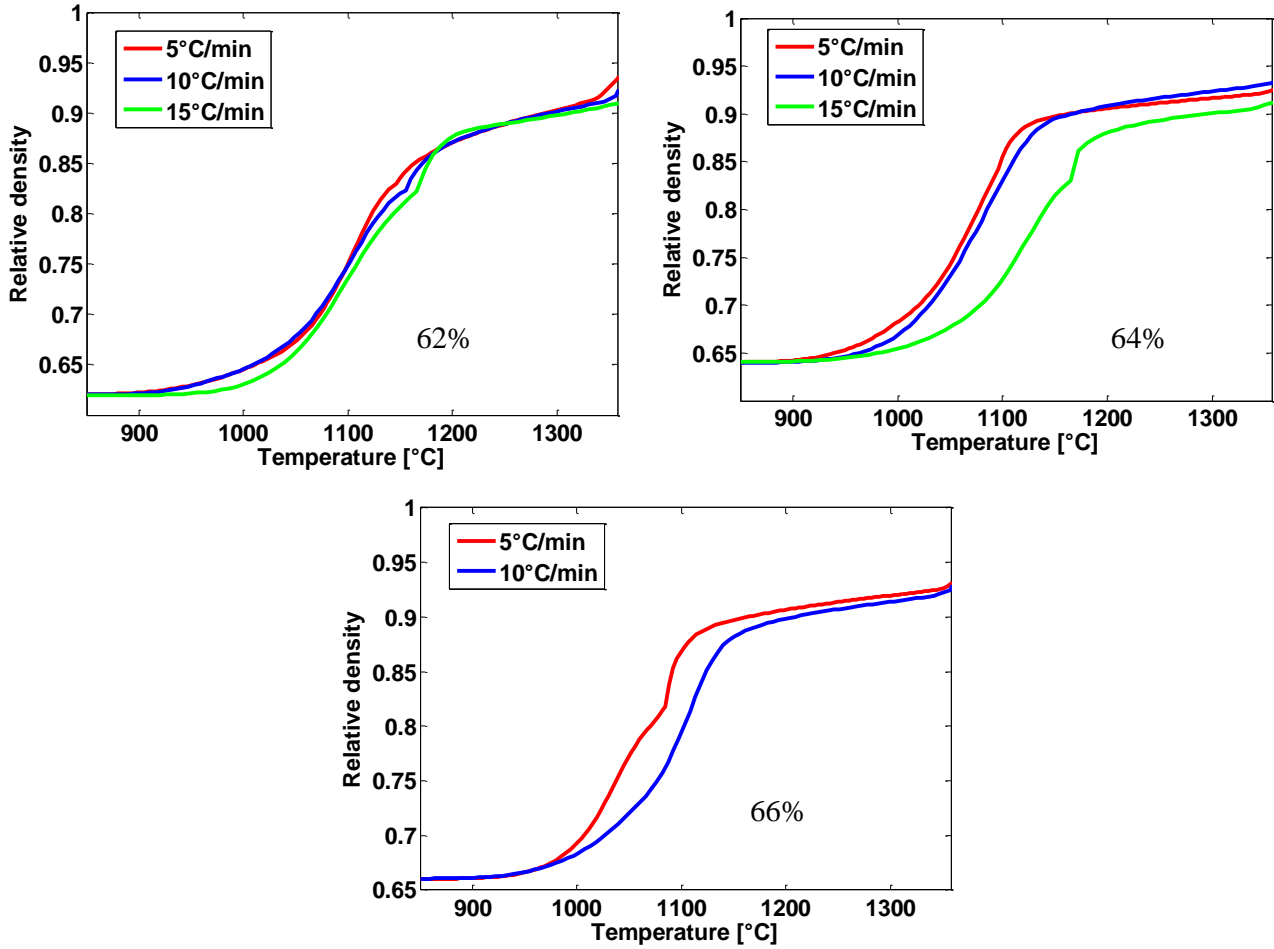


**Figure 92.** Comparison between experimental shrinkages in vertical dilatometer during the sintering stages with different heating rates and identified ones for 316 L stainless steel feedstock (D<sub>50</sub>=3.4 μm, formulation F3, powder volume loading is 64%)



**Figure 93.** Comparison between experimental shrinkages in vertical dilatometer during the sintering stages with different heating rates and identified ones for 316 L stainless steel feedstock (D<sub>50</sub>=3.4 μm, formulation F3, powder volume loading is 66%)

In addition, the relative densities associated to these three heating cycles for 316 L stainless steel feedstock ( $D_{50}=3.4 \mu\text{m}$ , formulation F3) with different powder volume loadings of 62%, 64% and 66% have been calculated with the identified shrinkage, as shown in **Figure 94**. Compared with the ones obtained in the horizontal dilatometer, higher values (about 0.95) of the relative density have been reached with more significant shrinkages.

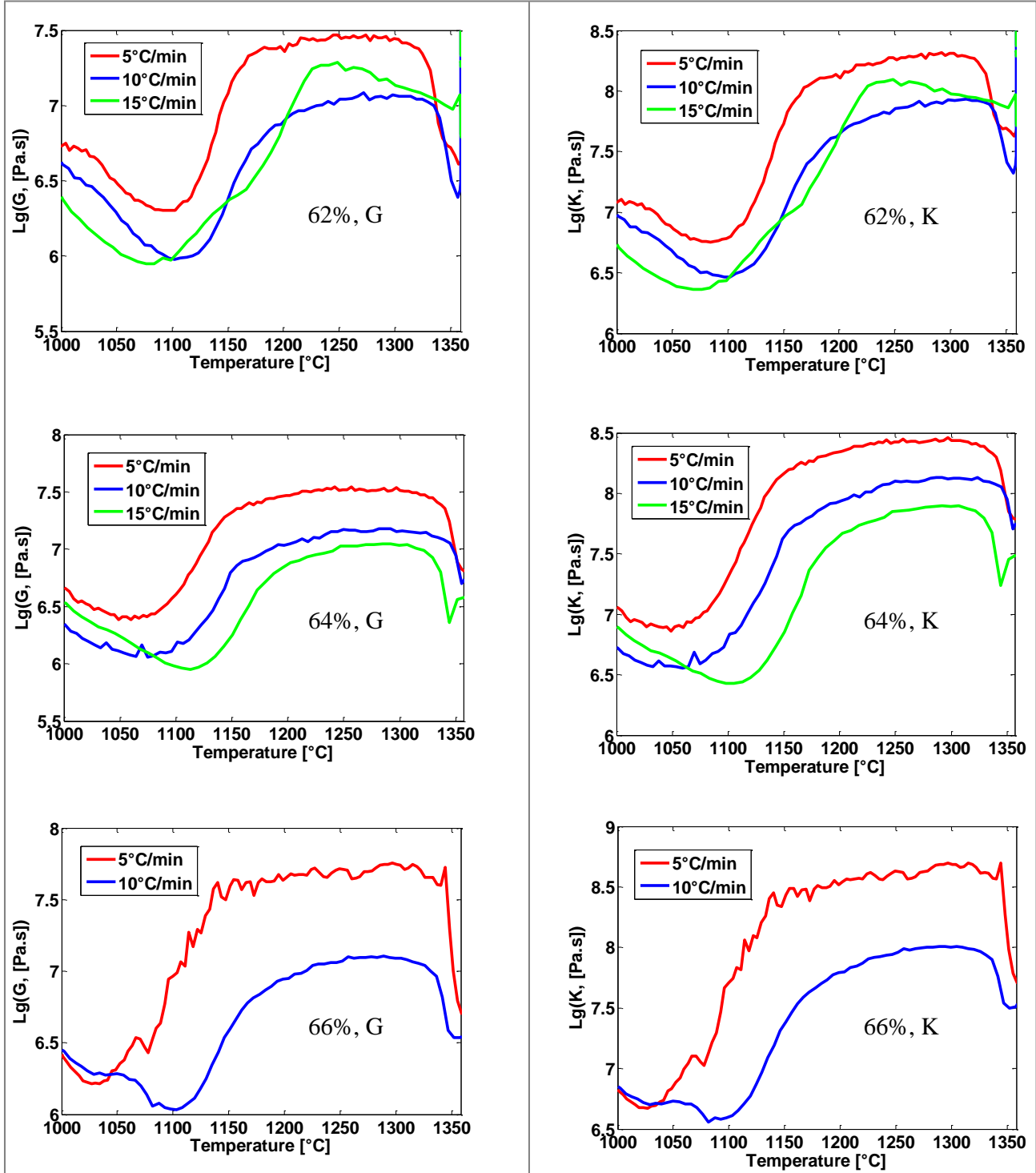


**Figure 94.** Calculated relative densities according to equation (20) for 316 L stainless steel feedstock ( $D_{50}=3.4 \mu\text{m}$ , formulation F3, powder volume loading of 62%, 64% and 66%) during the sintering stages with different heating rates of 5, 10 and 15 °C/min

#### 5.2.2.2. Numerical identification of viscosity parameters

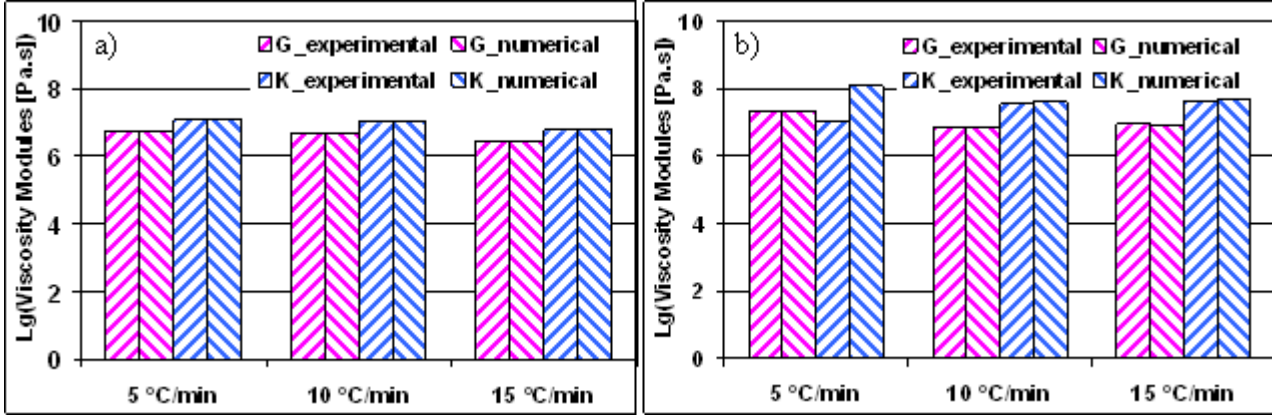
In parallel to the identification of sintering stress, the shear and bulk viscosity modules have been calculated using equation (17) for the 316L stainless steel feedstock ( $D_{50}=3.4 \mu\text{m}$ , formulation F3, powder volume loading of 62%, 64% and 66%). The modules  $G$  and  $K$  have been calculated by using the above identified shrinkages and relative densities. The results are plotted (in logarithmic coordinates) vs. temperature in **Figure 95** in accordance to the three heating cycles.  $G$  and  $K$  begin to increase when the temperature is greater than 1000 °C, which confirms well the experimental results obtained in the

dilatometer and they give the values always smaller than 0.31 GPa.s for all the tested cases. Besides, the values of  $G$  and  $K$  with the same heating rate as the powder volume loadings rise at the same temperature. Note that for the feedstock loaded at 62%,  $G$  and  $K$  exhibit an abrupt increase at about 1225 °C for heating rate equal 15 °C/min, which is generated by the abrupt increase of the uniaxial viscosity with the same heating rate.

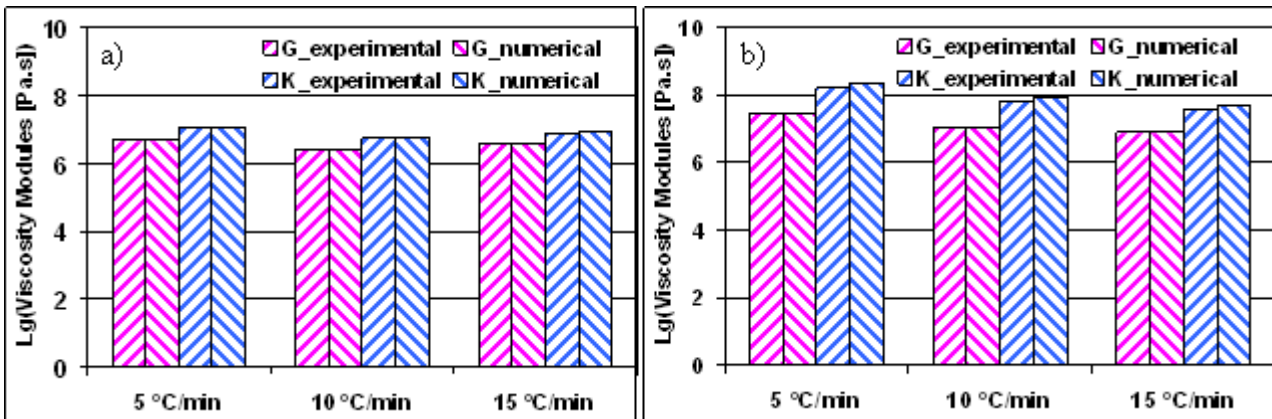


**Figure 95.** The identified shear and bulk viscosity modules according to equation (17) during the sintering stages with different heating rates for 316 L stainless steel feedstock ( $D_{50}=3.4 \mu\text{m}$ , formulation F3, powder volume loading of 62%, 64% and 66%)

Moreover, the experimental and numerical identified viscosity modules ( $G$  and  $K$ , in logarithm coordinates) during the sintering stages with different heating rates have been compared in **Figure 96**, **Figure 97** and **Figure 98** for three powder volume loadings. As different moments of the sintering stage gives different  $G$  and  $K$ , 1000 °C and 1200 °C have been selected as the examples to demonstrate these results.

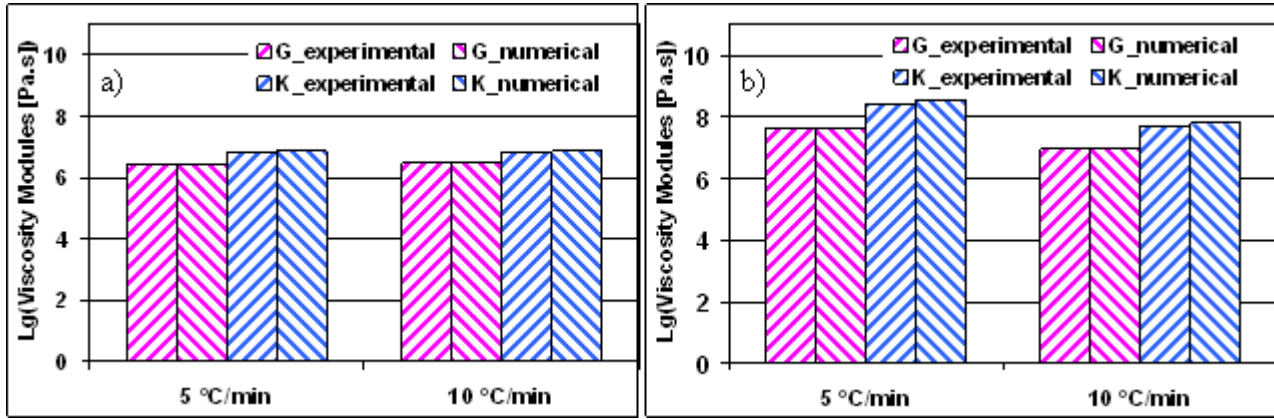


**Figure 96.** Comparison of shear ( $G$ ) and bulk ( $K$ ) viscosity modules (in logarithm coordinates) from experiments and numerical identification with different heating rates during the sintering stages for 316 L stainless steel feedstock ( $D_{50}=3.4 \mu\text{m}$ , formulation F3, powder volume loading of 62%) at temperature of a) 1000 °C and b) 1200 °C



**Figure 97.** Comparison of shear ( $G$ ) and bulk ( $K$ ) viscosity modules (in logarithm coordinates) from experiments and numerical identification with different heating rates during the sintering stages for 316 L stainless steel feedstock ( $D_{50}=3.4 \mu\text{m}$ , formulation F3, powder volume loading of 64%) at temperature of a) 1000 °C and b) 1200 °C

It is shown that the identified viscosity modules are in perfect agreement with the experimental ones. All the same, one exception should be noted that the identified  $K$  at 1200 °C with heating rate equal 5 °C/min for powder volume loading of 62%. To explain this problem, new experiments and identifications will be carried out. Still due to the lack of specimens load at 66%, only two sintering stages with heating rates of 5 °C/min and 10 °C/min have been studied, and the results have been related in **Figure 98**, the identified viscosity modules fit well the experimental values as well.



**Figure 98.** Comparison of shear ( $G$ ) and bulk ( $K$ ) viscosity modules (in logarithm coordinates) from experiments and numerical identification with different heating rates during the sintering stages for 316 L stainless steel feedstock ( $D_{50}=3.4 \mu\text{m}$ , formulation F3, powder volume loading of 66%) at temperature of a) 1000 °C and b) 1200 °C

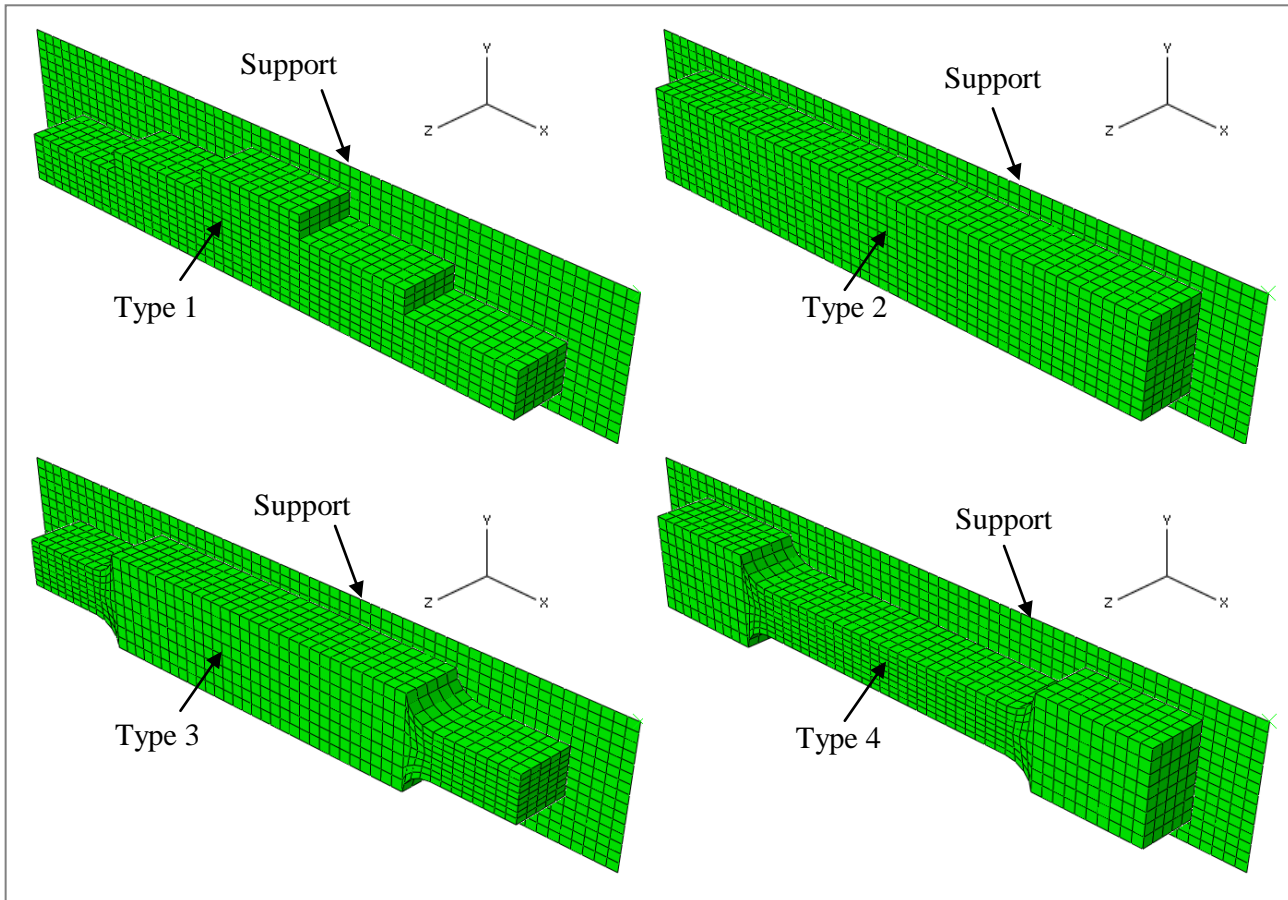
### 5.3. FE simulation of the sintering stage for the components from micro-MIM with 316 L stainless steel feedstock

In this study, the sintering process is investigated using numerical analysis are the four types of specimen from micro injection with the 316 L stainless steel feedstock ( $D_{50}=3.4 \mu\text{m}$ , formulation F3) loaded at 62%, 64% and 66% with Abaqus® software. The sintering stages with three heating rates of 5 °C/min, 10 °C/min and 15 °C/min till 1200 °C have been simulated and compared with the already obtained experimental results. However, only two sintering stages with heating rates of 5 °C/min and 10 °C/min have been simulated for powder volume loading equal 66%, due to the absence of the identification for sintering stage of 15 °C/min (mentioned in section 5.2.1.1), so no comparison has been done with the experimental results for this powder volume loading.

The sintering simulations of whole parts are sometimes based on results from numerical investigations of processing production steps like uniaxial die compaction, isostatic compaction, slip and tape casting, debinding or drying [176]. For example, the inhomogeneous density colors obtained after injection stage leads to differential shrinkage of different volume elements and is the main reason for the developing distortions during sintering in this production route [177] [178] [179] [180] [181]. However, in our case, the initial density distributions of the pre-sintered components are supposed due to the proper homogeneity of the feedstock.

The constitutive equations for the investigated sintering stage have been defined in section 5.1, considering thermo-elasto-viscoplastic properties to decide the final shape of the four types of specimens from the micro injection. The fully coupled thermal-stress analysis is chosen for simulation [182]. The whole set of the equations has been implemented in the FE software ABAQUS/Standard

(version 6.9-2) as a user supplied material routine (UMAT). The assembly composed of the micro-specimens and the support has been demonstrated in **Figure 99**.



**Figure 99** FE mesh of the four micro-specimen types and the support plate before sintering

The support for the four types of specimens is the same one. R3D4 and C3D8R have been set for the support and the specimens as the element type, respectively. More details about characterization of the mesh for these assemblies have been given in **Table 28**.

**Table 28.** Characterization of the mesh used in the investigated simulation

Component	Support	Type 1	Type 2	Type 3	Type 4
Element type	R3D4	C3D8R	C3D8R	C3D8R	C3D8R
Number of element	900	2100	2500	2160	2160
Number of node	976	2898	3366	2970	2970

The frictional coefficient between the specimens and the support has been set at 0.5 resulting from previous analysis [167]. In addition, some other material parameters have been used in the simulation; they are related in **Table 29**.

**Table 29.** Material parameters (316L stainless steel feedstock,  $D_{50}=3.4 \mu\text{m}$ , formulation F3) used in the simulation with Abaqus®

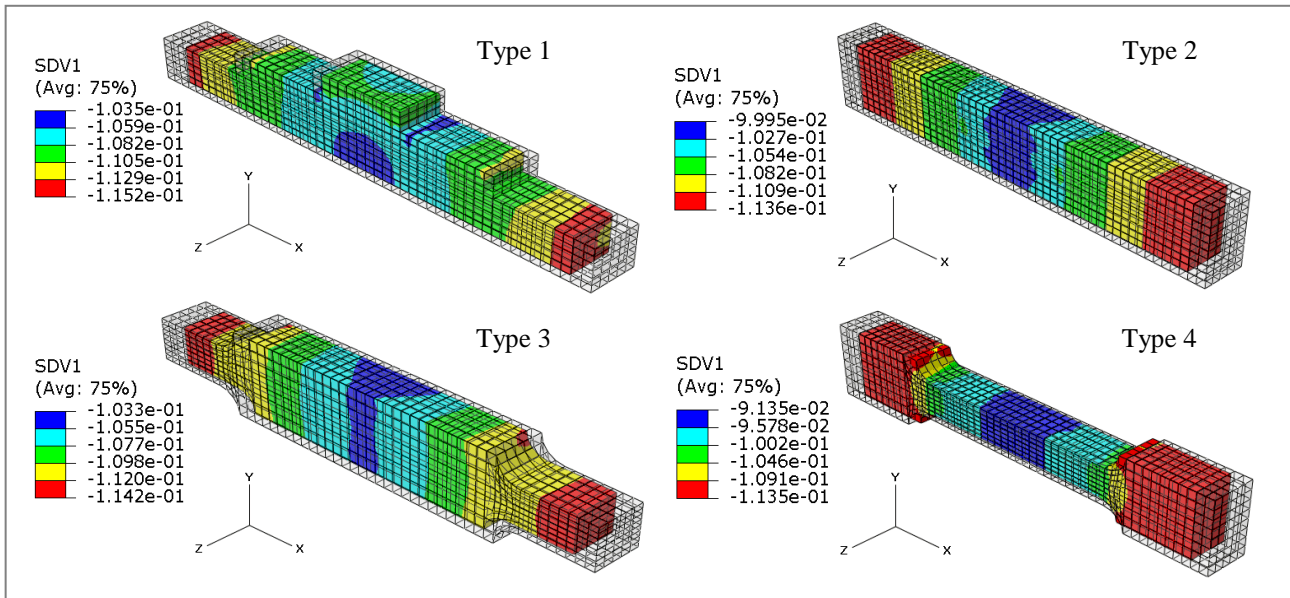
Young modulus	196 GPa
Elastic Poisson's ratio	0.28
Thermal conductivity	14.6 W/(m °C) [183]
Thermal expansion coefficient	$1.12 \times 10^{-5} \text{ } ^\circ\text{C}^{-1}$



### 5.3.1. Prediction of shrinkages for micro- injected specimens with 316L stainless steel feedstock ( $D_{50}=3.4\ \mu\text{m}$ , formulation F3)

The homogeneous green relative densities equal 0.62, 0.64 and 0.66 have been used in simulation corresponding to the feedstocks loaded at 62%, 64% and 66%, respectively.

The final shrinkages (in 3D) (powder volume loading equal 62%, heating rate equal 5 °C/min) of the sintered micro-specimens have been shown in **Figure 100**, and then the comparisons between the simulated shrinkages and the experimental ones in length, width and thickness directions are related in **Figure 101**. The other simulation results and comparisons have been shown in Appendix I, according to different powder volume loadings and heating rates.



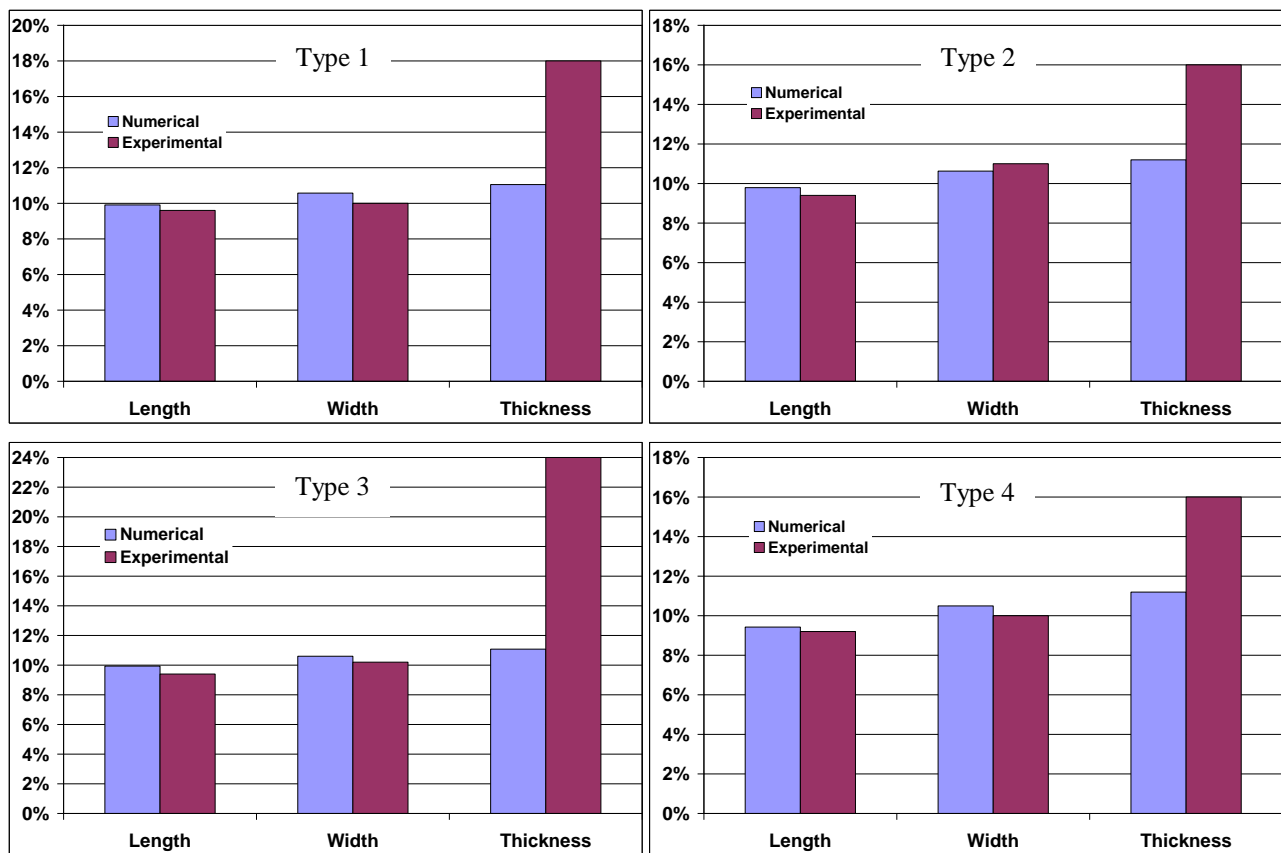
**Figure 100.** Numerical shrinkages of the four types of micro specimen (316L stainless steel,  $D_{50}=3.4\ \mu\text{m}$ , formulation F3, powder volume loading=62%) after the sintering stage (heating rate=5 °C/min)

As we discussed at the beginning of this chapter, no real manufacturing of the micro-specimen loaded at 66% have been processed, so only the numerical values have been given in **Figure 115** and **Figure 116** for this powder volume loading.

According to the results for powder volume loading of 62% and 64% (**Figure 100** to **Figure 109**), it can be observed that the experimental and numerical shrinkages are in good agreement in length and width directions, especially for the sintering stage with heating rates of 5 °C/min and 10 °C/min. And for these two heating rates, the shrinkages are more homogeneous than the ones for 15 °C/min, which can be proved by the variation over 20% in light of shrinkage for the heating rate of 15 °C/min. In addition, significant changes in shrinkage have been revealed by different types of the micro-specimens with the heating rate of 15 °C/min. It means that the shrinkages evidently vary according to different forms of the component to be sintered. The worse prediction of the dimensional shrinkages for the heating rate of

15 °C/min is caused by this rapid thermal kinetic, which can generate more probable distortions to the components under sintering, and this influence can particularly be more obvious for the micro-components. So in terms of the resulted shrinkage, it can be concluded that a relatively slow heating rate is preferred by the sintering stage for the micro-components with complex form, regarding the high sensibility of component form associated to the rapid heating rate.

Some studies have been done about the gravity effects on the shrinkages of the sintering components [184] [185]. The influence of gravity on uneven shrinkage of the sintered body depends on its dimensions, support reaction, and the initial density distribution. Considering the gravitational effect, more uneven shrinkages have been also observed in our study in the thickness direction for all these four types of specimens compared with the shrinkages in other directions.



**Figure 101.** Comparison between the experimental and the numerical shrinkages of the four types of micro specimen (316L stainless steel,  $D_{50}=3.4\ \mu\text{m}$ , formulation F3, powder volume loading=62%) after the sintering stage (heating rate=5 °C/min)

Furthermore, if the contrast should be done between the sintered micro-specimens loaded at 62% and 64% in view of shrinkage, we can find out that the present results can hardly agree with the argument that higher powder volume loading generally leads to lower dimensional shrinkage, and it will be even worse when the simulation results are taken into account. One of the main reasons is due to the fact that the identification results of shear viscosity modules  $G$  and bulk viscosity modules  $K$  with heating rate of

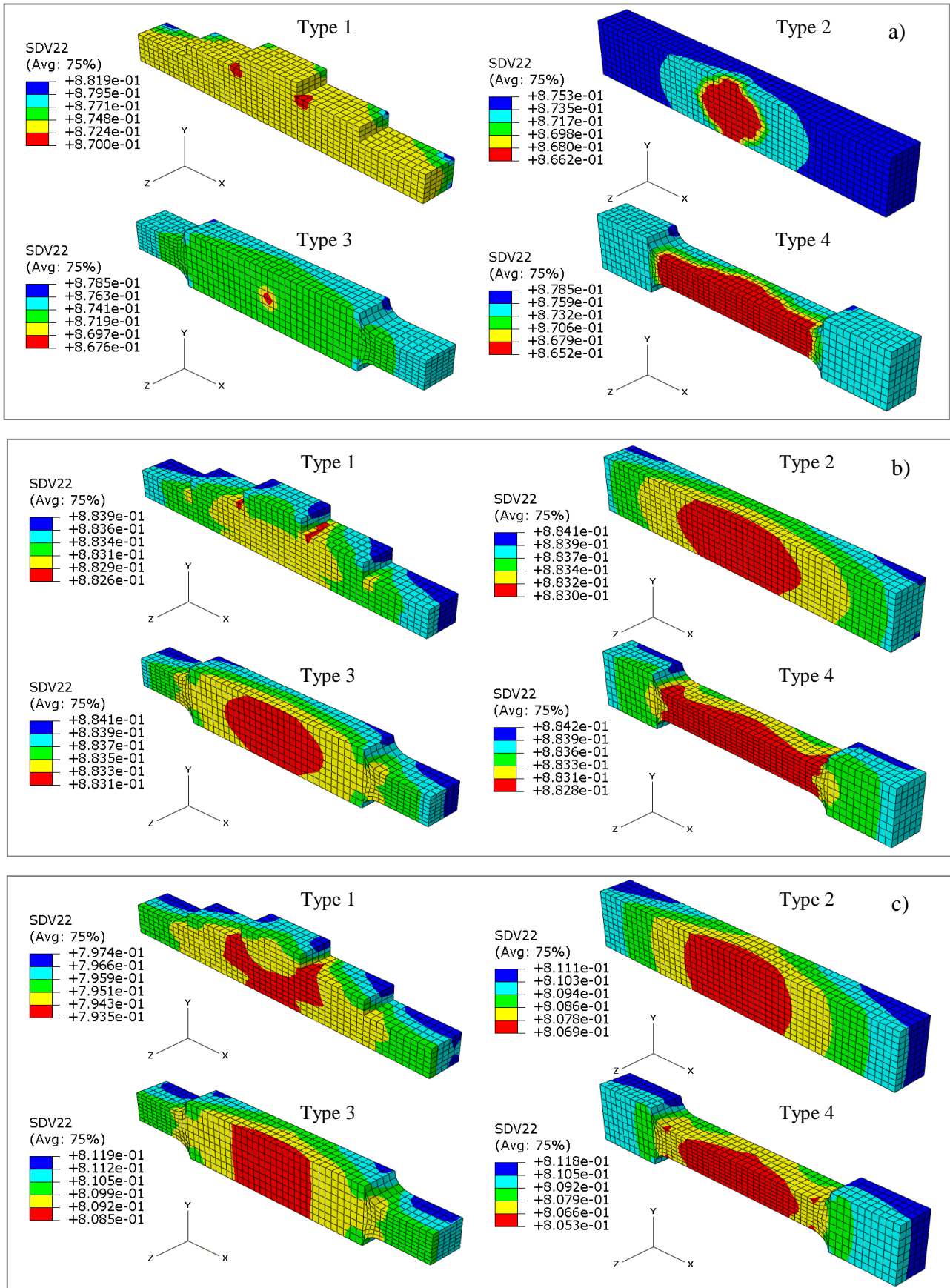


5 °C/min are not very steady (see **Figure 95**), which have increased abruptly from about 1100 °C and then slowed down the shrinkage in the simulation.

### 5.3.2. Prediction of relative density for the micro-injected specimens with 316L stainless steel feedstock ( $D_{50}=3.4\text{ }\mu\text{m}$ , formulation F3)

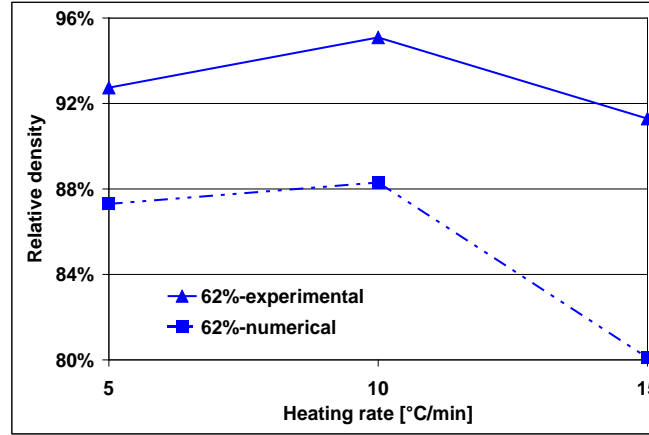
Besides of shrinkages, the relative densities have been simulated as well for these micro-specimens injected with powder volume loading of 62%, 64% and 66%, respectively. The relative density distributions (powder volume loading equal 62%, heating rate equal 5 °C/min) of the sintered micro-specimens have been illustrated in **Figure 102**. The other simulation results have been shown in section Appendix II, according to different powder volume loadings and heating rates.

As it is shown in the figures, the relative densities are generally homogeneous for most of the simulations, in which the variations have been well controlled within 1%. However, some different results have been encountered for the powder volume loading of 64% with heating rate of 15 °C/min (see **Figure 117 c**) and powder volume loading of 66% with heating rate of 5 °C/min (see **Figure 118 a**). Especially the simulation for the first one (powder volume loading=64%, heating rate=15 °C/min), a highest value of 100% has been attained by the micro-specimens of type 2, type 3 and type 4 while their shapes have been significantly changed. This is due to the higher heating rate afforded to these micro-specimens, which evidenced by the experimental phenomena mentioned in section 5.3.1, the components loaded higher are particularly more sensitive to the rapid heating rate. Though in contrast with these three types of micro-specimen, a relatively homogeneous distribution has been given by type 1, as shown in the same figure, just 3% as the variation has been found. Some little better results have been obtained in the second one (powder volume loading=66%, heating rate=5 °C/min), in which study about 5% error has been revealed by the micro-specimens of type 1, type 3 and type 4, but for one of type 2, perfect densification has been achieved (only 0.77% as the variation) due to the more simple form of this type.

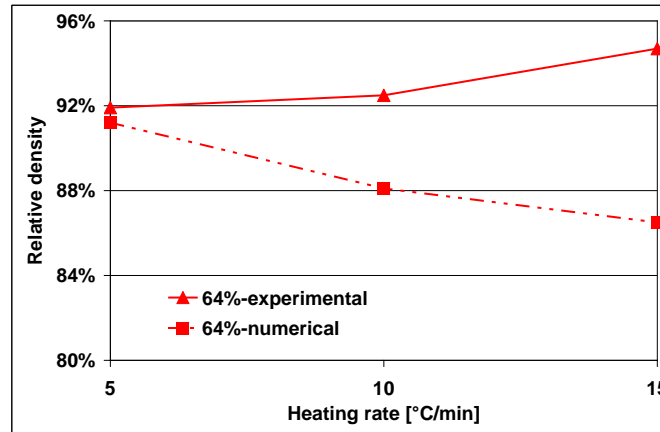


**Figure 102.** Numerical relative densities of the four types of micro-specimen (316L stainless steel,  $D_{50}=3.4 \mu\text{m}$ , formulation F3, powder volume loading=62%) after the sintering stage with heating rate of a) 5 °C/min, b) 10 °C/min and c) 15 °C/min

Finally, with the measurement of the relative density (mentioned in section 4.2.4.2) for the sintered micro-specimens, the comparison between the experiments and these simulations have been summarized and the mean values are plotted in **Figure 103** and **Figure 104** for powder volume loading of 62% and 64%, respectively.



**Figure 103.** Comparison between the experimental and the numerical relative density corresponding to four types of micro specimen (316L stainless steel,  $D_{50}=3.4\ \mu\text{m}$ , formulation F3, powder volume loading=64%) after the sintering stage (heating rate=5 °C/min, 10 °C/min and 15 °C/min)



**Figure 104.** Comparison between the experimental and the numerical relative density corresponding to four types of micro specimen (316L stainless steel,  $D_{50}=3.4\ \mu\text{m}$ , formulation F3, powder volume loading=64%) after the sintering stage (heating rate=5 °C/min, 10 °C/min and 15 °C/min)

Actually, obvious differences between the experimental and numerical values have been observed for both powder volume loadings. The results from simulation are almost smaller than the ones from experiment, this is due to the fact that the identification tests (mentioned in section 5.2.1) in the vertical dilatometer have been carried out in an argon atmosphere instead of vacuum to prevent them from getting oxidized. As it is known, in some worse situations, the pores will be coarsen due to the inner expansion of the gas in the pores when the sintering is processed at high temperature [186], the consequence is that the slow down and the reduction effect for densification, but there no gas trapped

when the sintering stage is carried out in vacuum atmosphere, that's why the experimental results are always higher than the ones simulated by using the identified parameters from the vertical tests.

## Summary

In this chapter, a phenomenological model of solid state diffusion sintering has been presented. Meanwhile the parameters ( $G$ ,  $K$  and  $\sigma_s$ ) should be determined have been highlighted. The beam-bending and free sintering tests in the vertical dilatometer have been realized in order to identify the model parameters. Consequently, the identifications in Matlab<sup>®</sup> have been successfully carried out, and the results have been related.

Based on the identified parameters, by coupling the other parameters proposed in literature and the other similar researches, such as Young modulus, elastic Poisson's ratio, thermal conductivity and the friction between the component and support, etc, the model has been implemented in the finite element code Abaqus<sup>®</sup> as a user defined material routine UMAT. The sintering stages with different heating rates (5 °C/min, 10 °C/min and 15 °C/min) are simulated for four micro-specimens types injected with three powder volume loadings (62%, 64% and 66%). As the results, the shrinkage and relative density associated to each sintering cycle have been related and compared to the experimental values, respectively. The simulation results fit well the experiments, especially for the sintering cycles with relative low heating rates and low powder volume loadings. However, due to the high sensibility of the component shape associated to the sintering cycle with rapid heating rate, the prediction of the sintering behavior for micro-specimens injected with high powder volume loading (66%) and rapid heating rate (15 °C/min) has to be improved in comparison with the other results.

In summary, the sintering computational simulation with the proposed thermo-elasto-viscoplastic model can generally predict the results of the sintering stage. But this ability in some cases remained limited for some particular situations, such as the very rapid heating rate during the sintering stage, the micro-specimens with complex form, the components injected with feedstock loaded very high, etc.

## Chapter 6. Conclusions and perspectives

The researches reported in this thesis focus on the elaboration and characterization of feedstock based on 316L stainless steel powders, the identification of material and physical parameters associated to the sintering stage and the numerical simulations of the sintering process by the FE method using the identified parameters. The main experimental developments and the related numerical simulations, as well as the future works in this chapter.

### 6.1. Conclusions

- In comparison to the previous Ph. D. theses carried out in our research team, new binder systems composed of different polymeric binder systems have been adapted to various 316L stainless steel powders (5  $\mu\text{m}$  and 16  $\mu\text{m}$ ). Three feedstock formulations have been elaborated using polyethylene and wax (Group #1), polypropylene + wax + acid (Group #2) and polyethylene + acid (Group #3). The resulting feedstocks for each group have been characterized using the mixing torque tests in twin-screw mixer and the shear viscosity tests using in capillary rheometer. Group #2 has been highlighted from the three groups due to the lower mixing torque and shear viscosity revealed by this binder system. Meanwhile, the feedstock associated to formulation F3 that is well adapted for both powders is retained for the subsequent tests.
- By using the selected F3 feedstock formulation, four methods have been employed to determine the critical powder volume loading with 316L stainless steel powder (5  $\mu\text{m}$ ): mixing tests by continuously powder content increasing and batch powder loading, rheological tests and feedstock viscosity model. The different powder volume loading ranges obtained according to each method are 64~70%, 64~70%, 66%~70 and 68%, respectively. By coupling these four ranges, the critical powder volume loading corresponding to formulation F3 has been located at 68% for the powder of 5  $\mu\text{m}$ .
- Mono-material injection with one single feedstock and bi-material injection with two different feedstocks have been properly developed and realized. Four types of micro-specimen used for the simulation validation have been injected with three 316L stainless steel feedstocks (5  $\mu\text{m}$ ) of 62%, 64%, and 66% corresponding to formulation F3. A two-plate mold has been used for the bi-material injection with 316L stainless steel feedstocks (5  $\mu\text{m}$ ) loaded at 60% and 64%, but the injection chambers are not separated for the different feedstocks, so the irregular joining of feedstock at the interface zone have been encountered in these first bi-material injection tests. Then micro component injected with 316L stainless steel feedstock (5  $\mu\text{m}$ ) and Cu feedstock has

been realized by using a three-plate mold with the separated die cavities. The interface between both feedstocks has been well controlled in comparison with the first process.

- Binder burnt-out tests have been carried out for the selected feedstocks in TGA module in the vertical dilatometer, as well as for the injected micro-specimens dedicated in order to validate the numerical simulations. In the first case, the feedstock pellets with different powders volume loading have been heated up to 500 °C, and the weight loss has been measured. In micro-specimen injection, TGA has been examined for injected specimens. Consequently, the homogeneity of feedstock has been investigated before and after injection. The measured weight losses in both cases are in good agreement to the theoretical binder weight in the feedstock formulation. In addition, the binders and powder particles distribution have been observed through SEM. Both TGA and SEM analyses lead to the same conclusion: the feedstock prepared corresponding to the selected formulation F3 (binder system composed of polypropylene, paraffin wax and stearic acid) are homogeneous.
- In order to identify the sintering parameters based on the proposed model, beam-bending and free sintering tests have been performed through TMA in a vertical dilatometer. Three heating rates corresponding to 5 °C/min, 10 °C/min and 15 °C/min have been used during these tests on 316L stainless steel (5 µm) feedstocks with various powder volume loadings (62%, 64% and 66%). On basis of the results obtained from the dilatometer, the shear viscosity module  $G$ , the bulk viscosity module  $K$  and the sintering stress  $\sigma_s$  have been properly identified using Matlab® software, The identified parameters fit well the experimental values.
- A thermo-elasto-viscoplastic model well suited for sintering stage has been implemented in Abaqus® finite element code, the element that are used correspond to R3D4 and C3D8R for the support and the four micro-specimens, respectively. The material parameters resulting from the experiments have been used to define the 316L stainless steel feedstock, together with the identified  $G$ ,  $K$  and  $\sigma_s$ . Finally, the sintering stage of 1200 °C for the four types of micro-specimens (powder volume loading of 62%, 64% and 66%) with three heating rates (5 °C/min, 10 °C/min and 15 °C/min) have been simulated. The experimental shrinkages and relative densities of the sintered micro-specimens have been compared to the simulation results. Adequate comparisons are related, especially for the case of lower heating rates adapted to the components injected with lower powder volume loadings and simple forms.

## **6.2. Perspectives**

### **6.2.1. Experiments and processing**

According to the obtained results, new investigations about the new binders involved in the feedstock formulations should be carried out, due to the fact that the linear relationship between shear viscosity and shear rate is influenced in relative high shear rate range (mentioned in section 2.5.2).

The difficulty of micro injection moulding with high powder volume loading (66%) on the devoted equipments should be improved, and then more specimens with this powder volume loading should be manufactured for the identification tests and the comparison with the simulation results.

For the debinding stage, some alternative debinding techniques will be introduced and tried in our research team, and still some modifications will be done for the debinding cycle and debinding atmosphere.

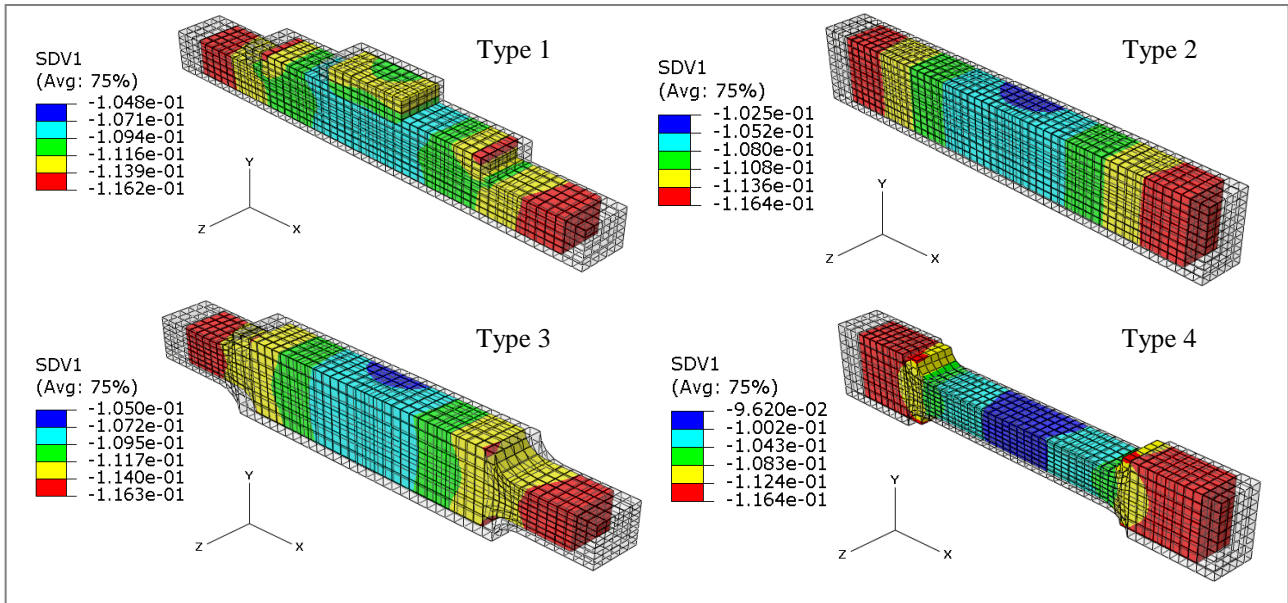
In terms of sintering stage, the micro-specimens injected with 316L stainless steel feedstock and Cu feedstock will be sintered in order to complete the bi-material injection moulding process, various sintering cycles and atmospheres will be tested. As a general objective, one has to develop the sintering capacities and related numerical simulations to be able to proceed with various materials.

### **6.2.2. Computational developments**

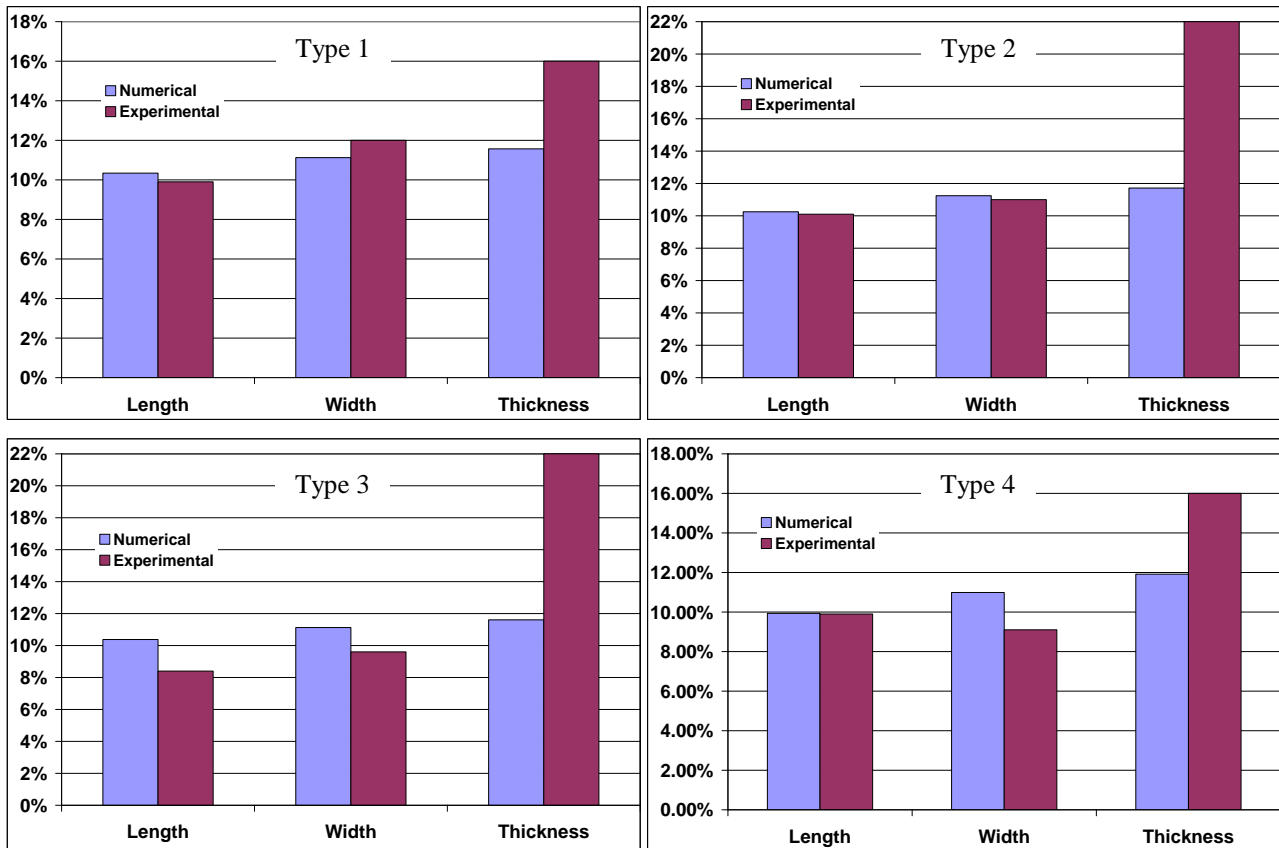
A sintering model specially developed for the densification of micro-MIM process, such as the microscopic model mentioned in section 5.1, will be correspondingly introduced and adapted to new developments as micro-specimens. Accordingly, new parameters dedicated to the numerical simulation should be identified. So new models will be introduced in Abaqus<sup>®</sup>, considering the worse situations in which the sintering stage with rapid heating rates accommodated to the complex micro-specimens with high powder volume loading. Finally, simulations for the sintering stage of bi-material injection moulding will be also performed by combining two material routines for the feedstocks involved in the bi-material component, on the basis of the identified parameters for each feedstock.

New challenges will also be investigated to provide the ability of the MIM process for the micro manufacturing of active functional devices (sensors ...), based on multi materials joining ability of the process.

## Appendix I: Simulated shrinkages and comparisons between the numerical and experimental results

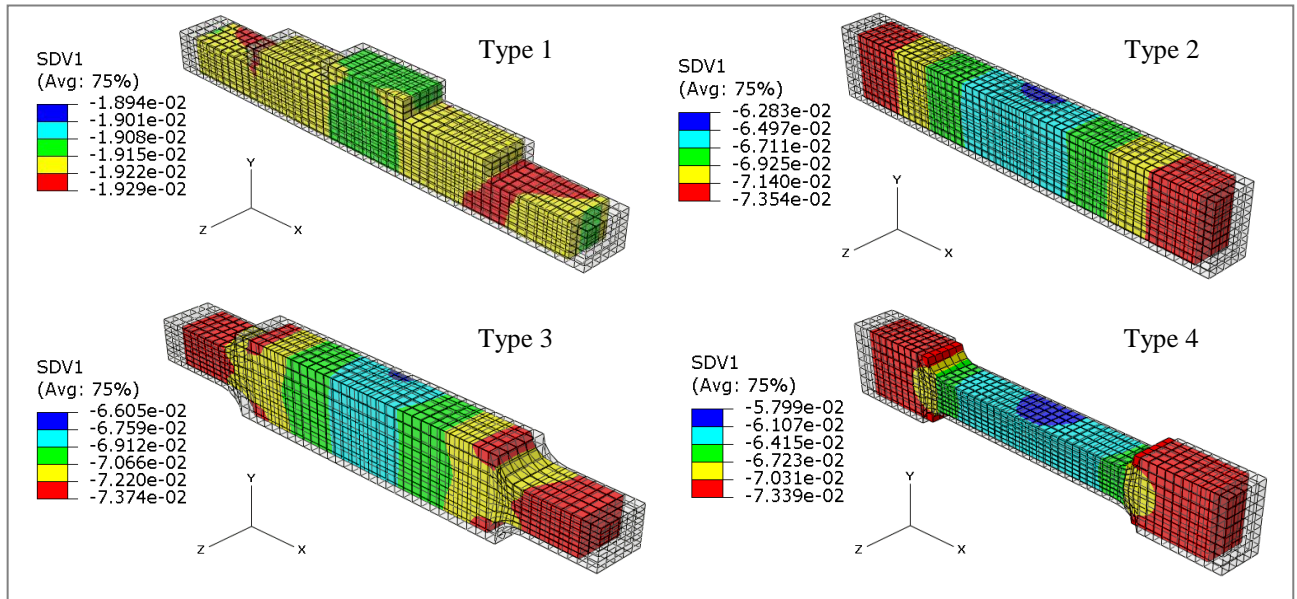


**Figure 105.** Numerical shrinkages of the four types of micro specimen (316L stainless steel,  $D_{50}=3.4\ \mu\text{m}$ , formulation F3, powder volume loading=62%) after the sintering stage (heating rate=10 °C/min)

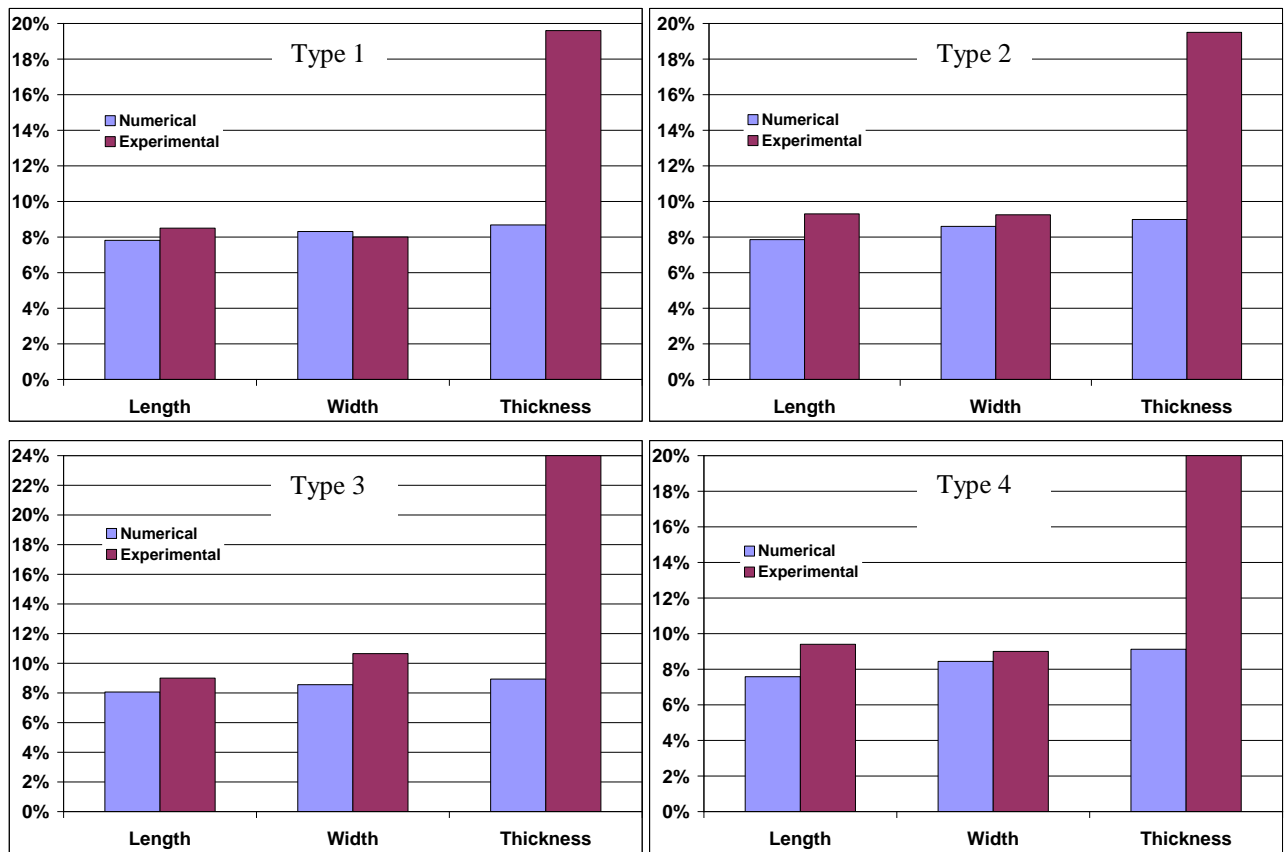


**Figure 106.** Comparison between the experimental and the numerical shrinkages of the four types of micro specimen (316L stainless steel,  $D_{50}=3.4\ \mu\text{m}$ , formulation F3, powder volume loading=62%) after the sintering stage (heating rate=10 °C/min)

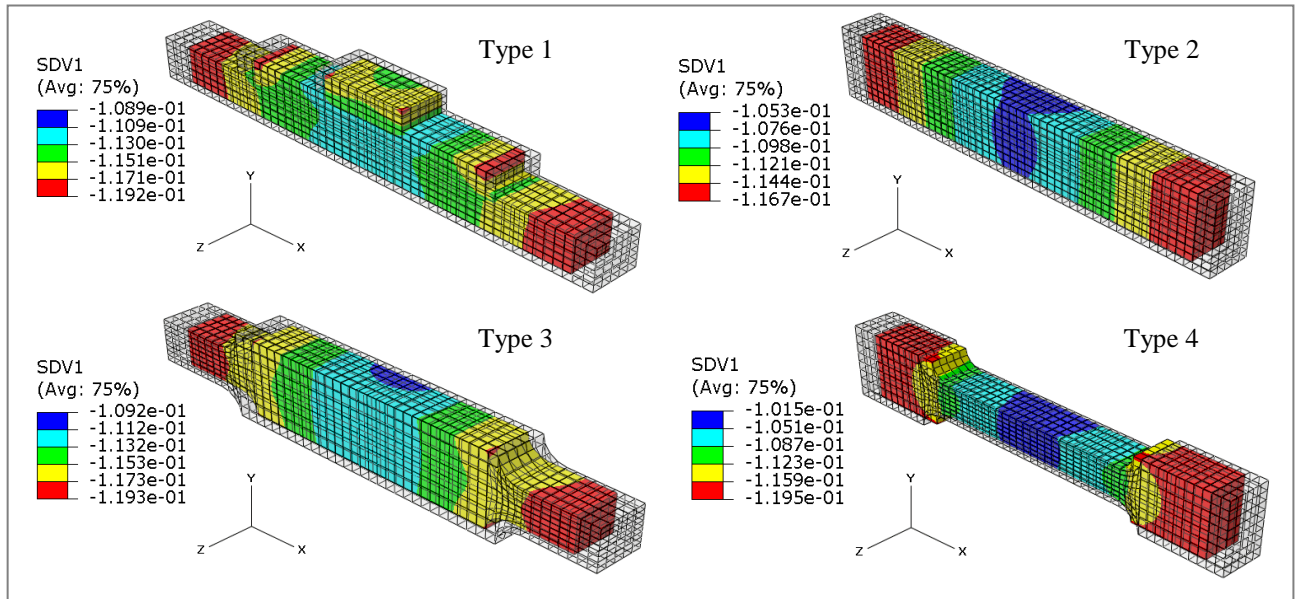




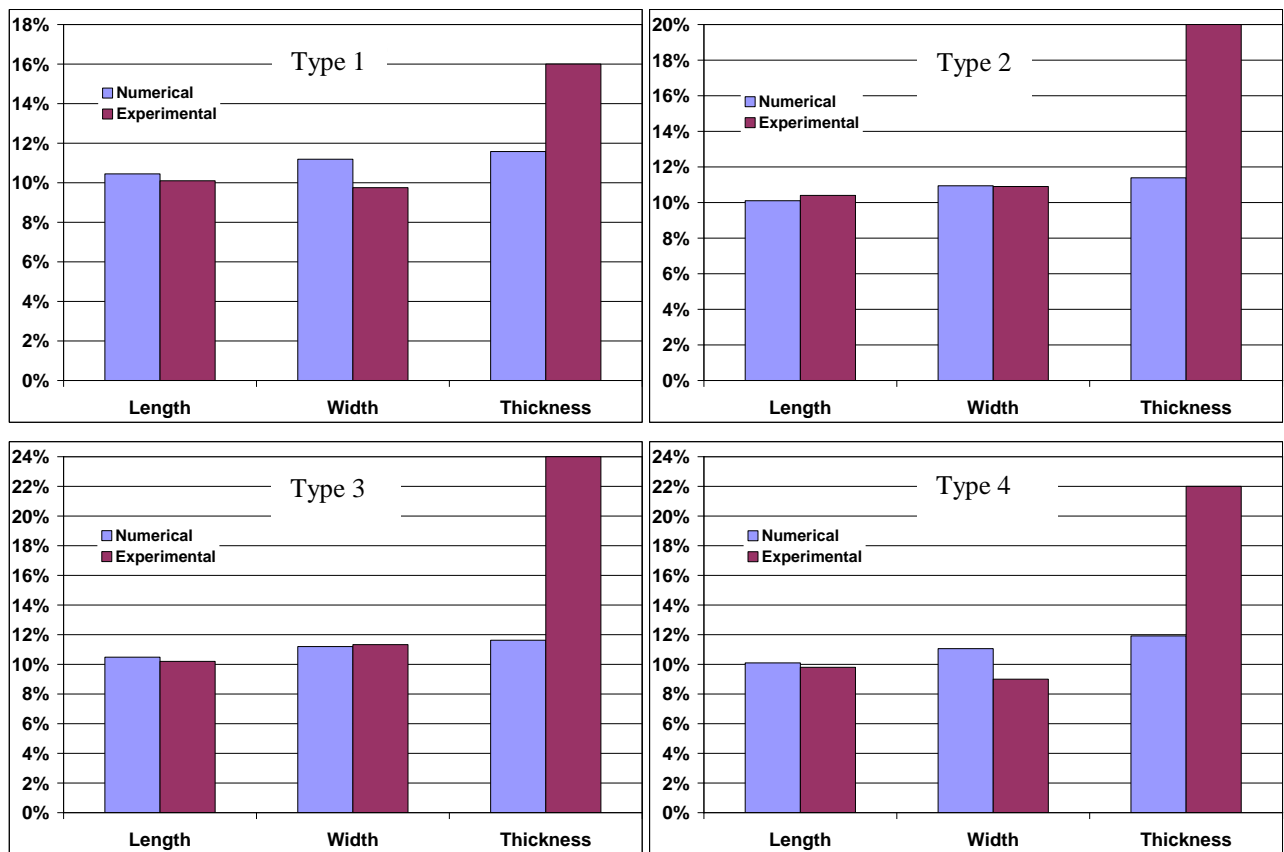
**Figure 107.** Numerical shrinkages of the four types of micro specimen (316L stainless steel,  $D_{50}=3.4\ \mu\text{m}$ , formulation F3, powder volume loading=62%) after the sintering stage (heating rate=15 °C/min)



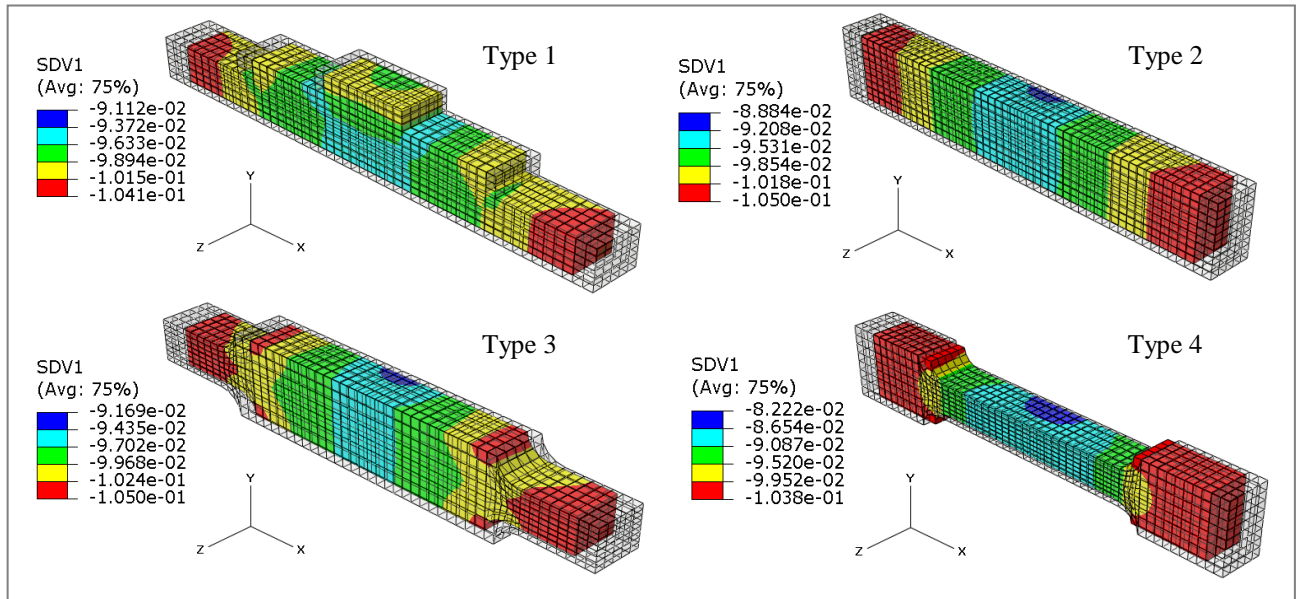
**Figure 108.** Comparison between the experimental and the numerical shrinkages of the four types of micro specimen (316L stainless steel,  $D_{50}=3.4\ \mu\text{m}$ , formulation F3, powder volume loading=62%) after the sintering stage (heating rate=15 °C/min)



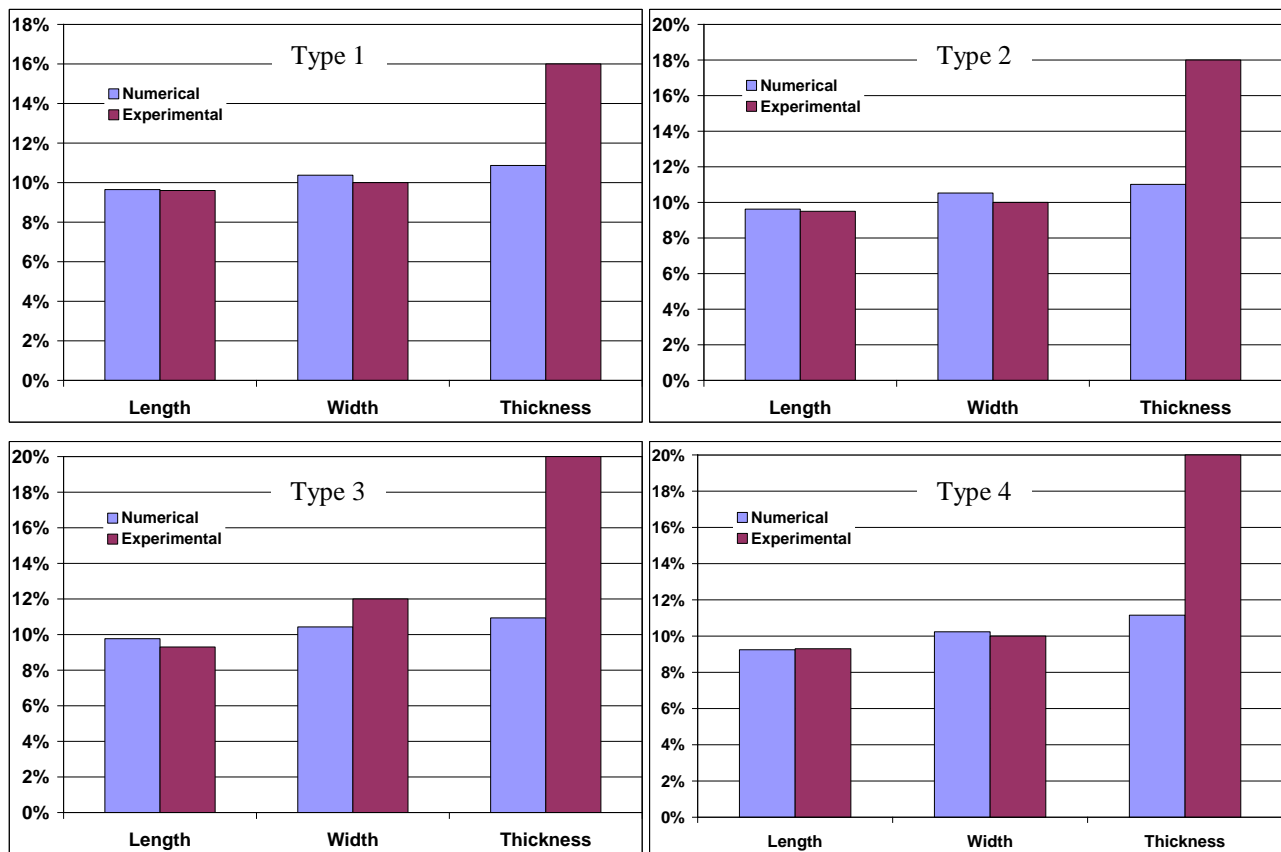
**Figure 109.** Numerical shrinkages of the four types of micro specimen (316L stainless steel,  $D_{50}=3.4 \mu\text{m}$ , formulation F3, powder volume loading=64%) after the sintering stage (heating rate=5 °C/min)



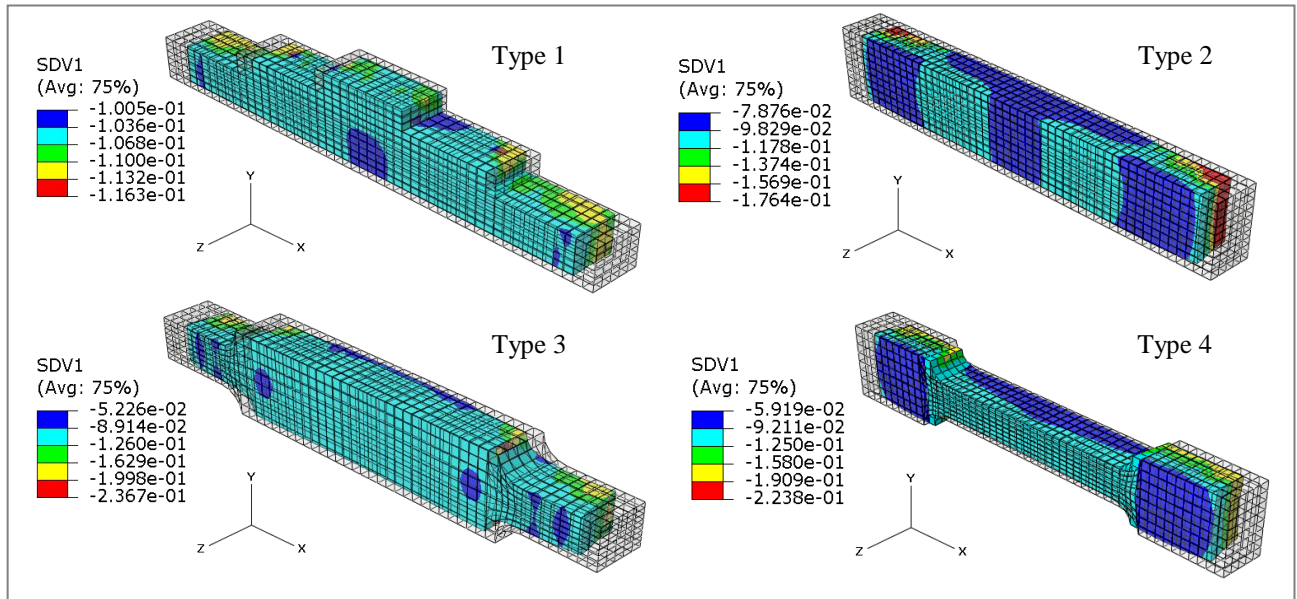
**Figure 110.** Comparison between the experimental and the numerical shrinkages of the four types of micro specimen (316L stainless steel,  $D_{50}=3.4 \mu\text{m}$ , formulation F3, powder volume loading=64%) after the sintering stage (heating rate=5 °C/min)



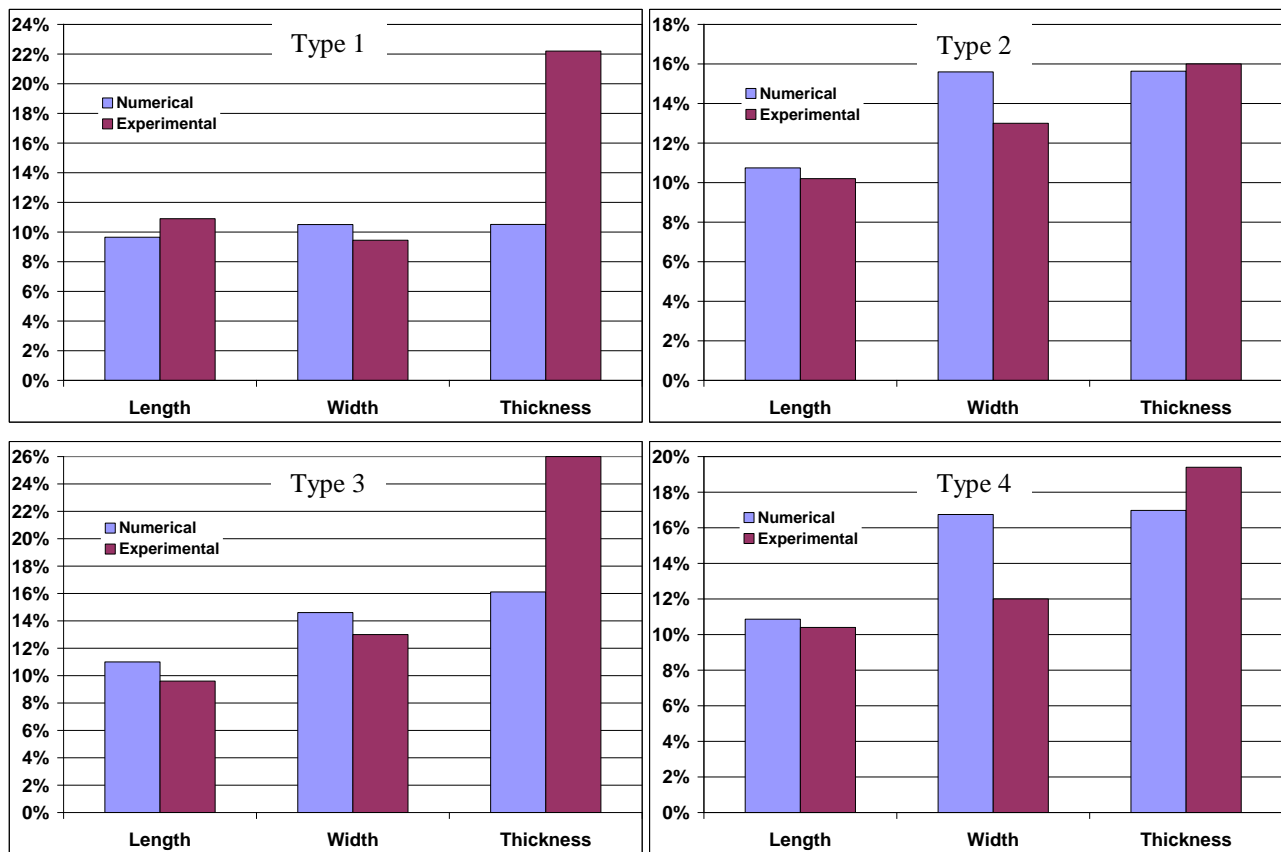
**Figure 111.** Numerical shrinkages of the four types of micro specimen (316L stainless steel,  $D_{50}=3.4 \mu\text{m}$ , formulation F3, powder volume loading=64%) after the sintering stage (heating rate=10 °C/min)



**Figure 112.** Comparison between the experimental and the numerical shrinkages of the four types of micro specimen (316L stainless steel,  $D_{50}=3.4 \mu\text{m}$ , formulation F3, powder volume loading=64%) after the sintering stage (heating rate=10 °C/min)

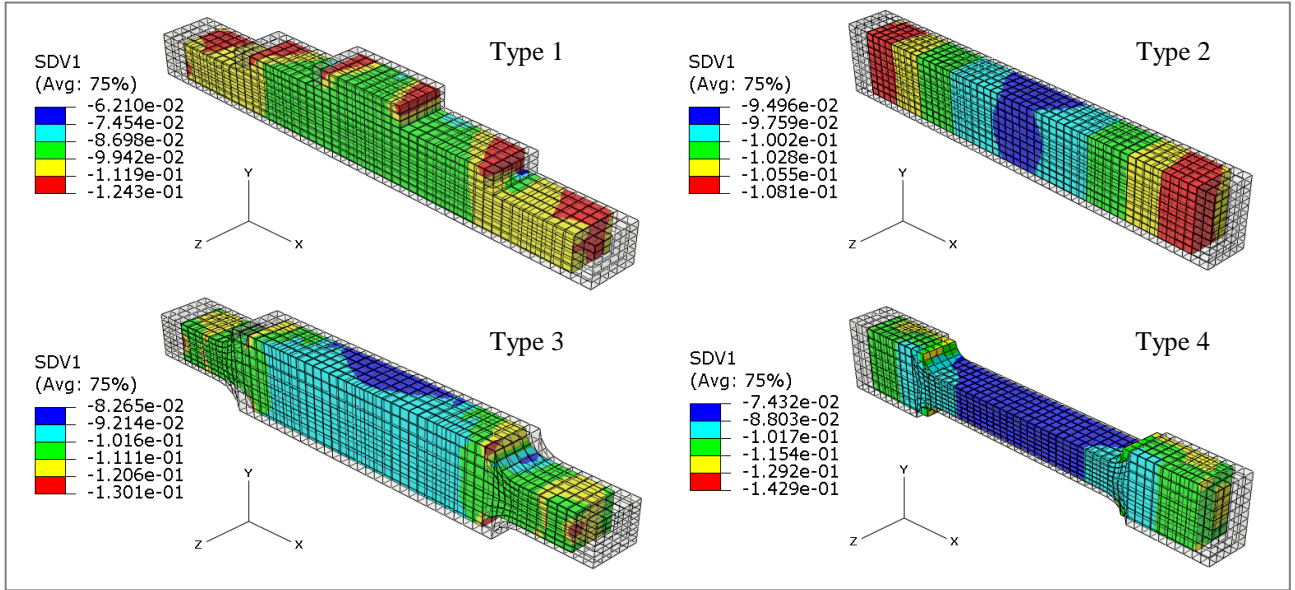


**Figure 113.** Numerical shrinkages of the four types of micro specimen (316L stainless steel,  $D_{50}=3.4 \mu\text{m}$ , formulation F3, powder volume loading=64%) after the sintering stage (heating rate=15 °C/min)

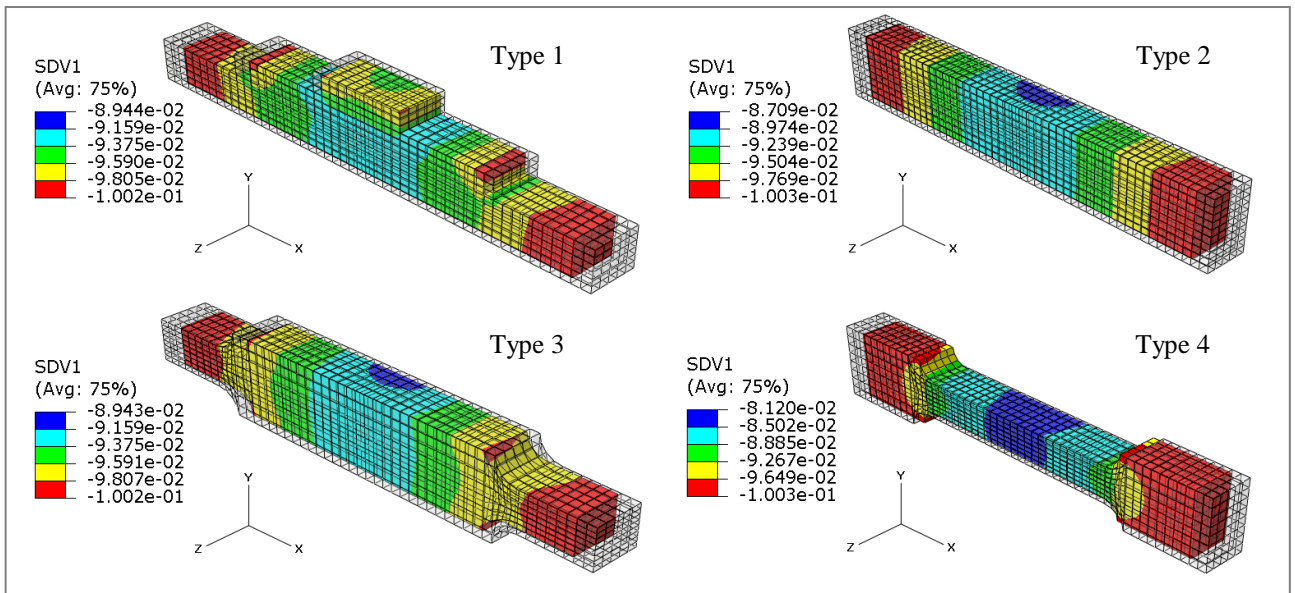


**Figure 114.** Comparison between the experimental and the numerical shrinkages of the four types of micro specimen (316L stainless steel,  $D_{50}=3.4 \mu\text{m}$ , formulation F3, powder volume loading=64%) after the sintering stage (heating rate=15 °C/min)



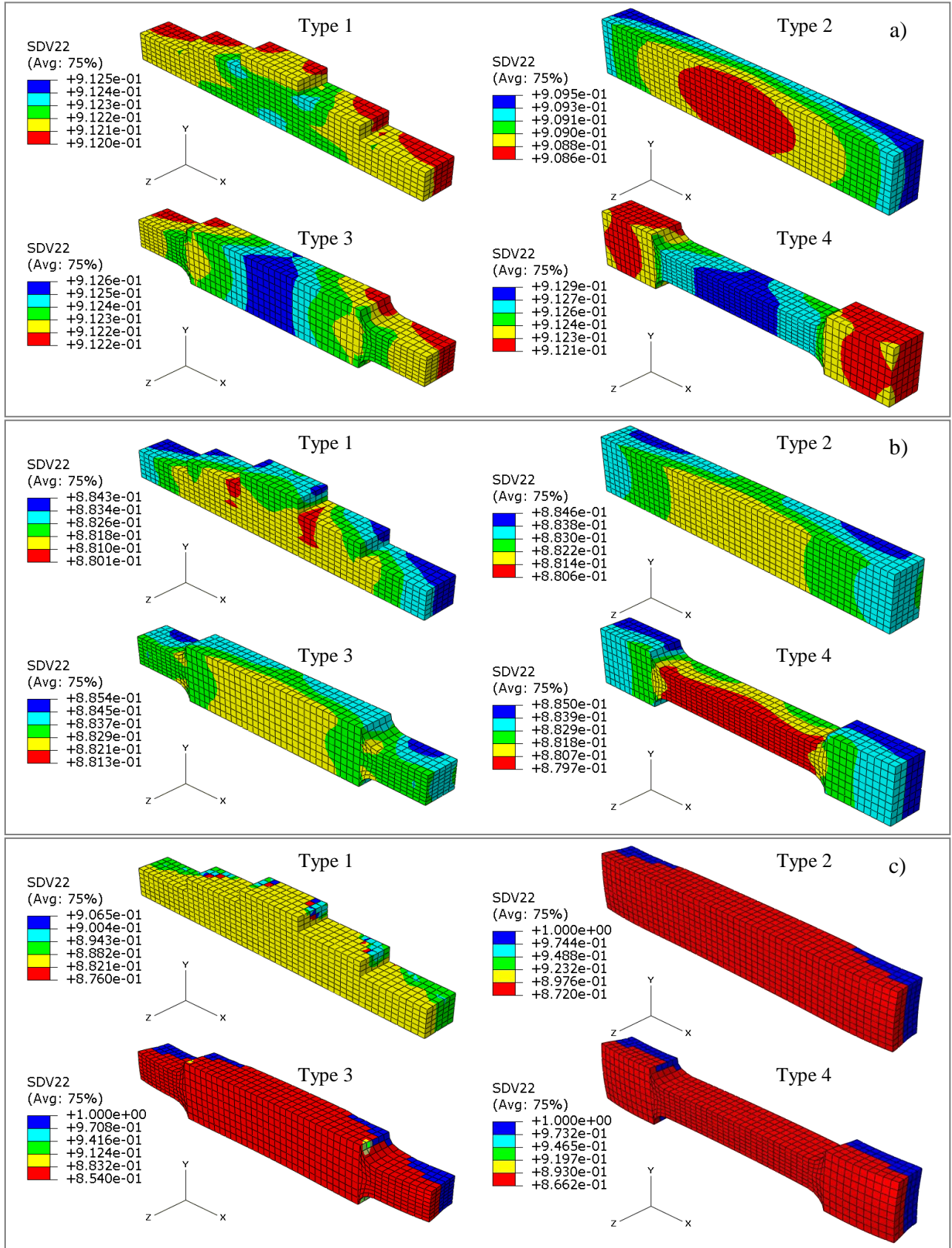


**Figure 115.** Numerical shrinkages of the four types of micro specimen (316L stainless steel,  $D_{50}=3.4 \mu\text{m}$ , formulation F3, powder volume loading=66%) after the sintering stage (heating rate=5 °C/min)

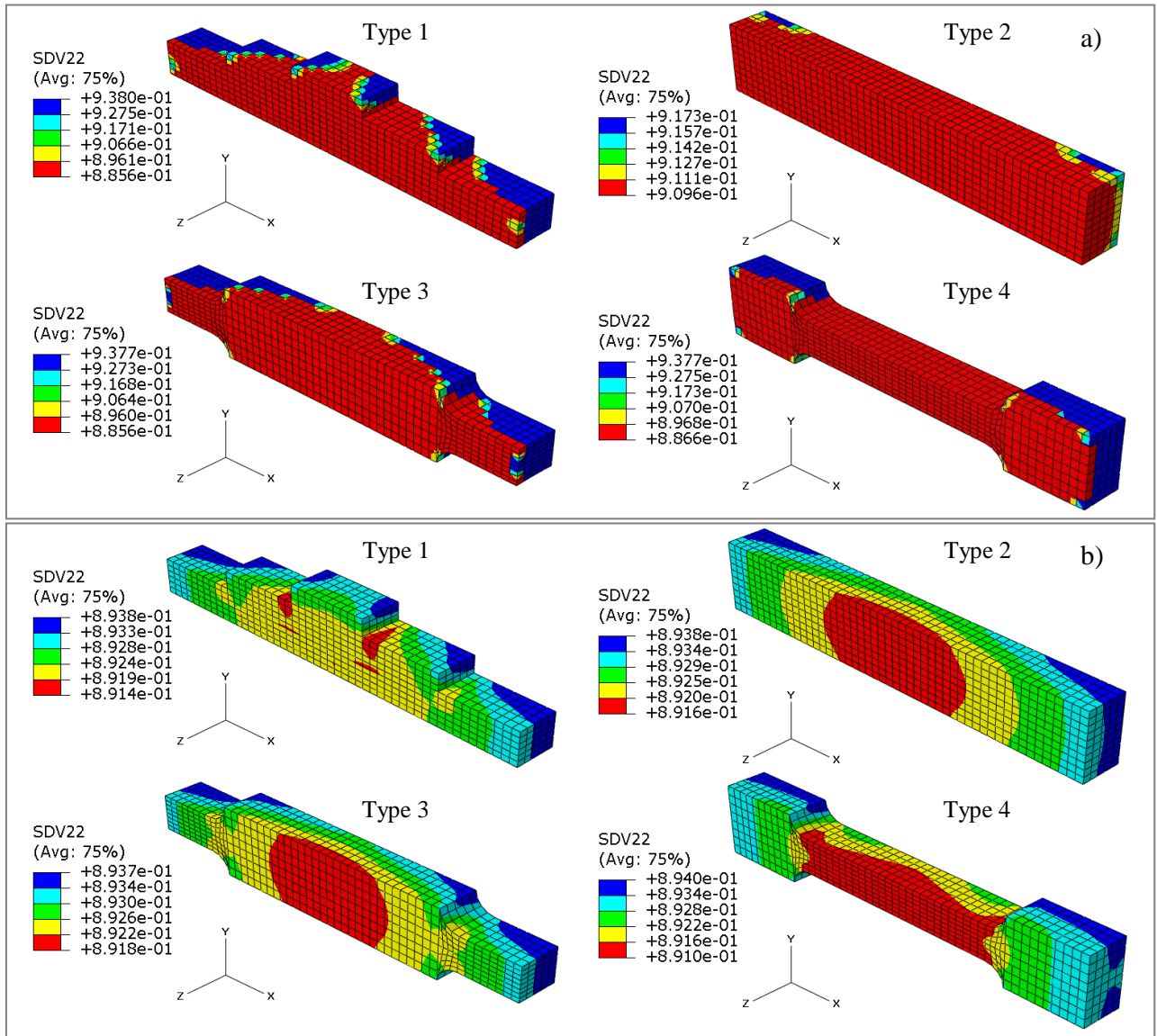


**Figure 116.** Numerical shrinkages of the four types of micro specimen (316L stainless steel,  $D_{50}=3.4 \mu\text{m}$ , formulation F3, powder volume loading=66%) after the sintering stage (heating rate=10 °C/min)

## Appendix II: Simulated relative density distributions



**Figure 117.** Numerical relative densities of the four types of micro-specimen (316L stainless steel,  $D_{50}=3.4 \mu\text{m}$ , formulation F3, powder volume loading=64%) after the sintering stage with heating rate of a) 5 °C/min, b) 10 °C/min and c) 15 °C/min



**Figure 118.** Numerical relative densities of the four types of micro-specimen (316L stainless steel,  $D_{50}=3.4 \mu\text{m}$ , formulation F3, powder volume loading=66%) after the sintering stage with heating rate of a) 5 °C/min and b) 10 °C/min

## Bibliography

- [1] **H.Ö. Gülsoy and R.M. German**, Production of micro-porous austenitic stainless steel by powder injection molding, *Scripta Materialia*, Volume 58, Issue 4, 2008, pp. 295-298.
- [2] **R.M. German and A. Bose**, *Injection Molding of Metals and Ceramics*, MPIF, 1997.
- [3] **C. H. Ji, N. H. Loh, K. A. Khor and S. B. Tor**, Sintering study of 316L stainless steel metal injection molding parts using Taguchi method: final density, *Materials Science and Engineering A*, Volume 311, Issues 1-2, 2001, pp. 74-82.
- [4] **K. Nishiyabu, I. Andrews and S. Tanaka**, Making and measuring in micro MIM manufacturing, *Metal Powder Report*, Volume 64, Issue 9, 2009, pp. 22-25.
- [5] **A. Rota, P. Imgrund, L. Kramer, R. Meyer and J. Haack**, Micro MIM approaches mass production , *Metal Powder Report*, Volume 60, Issue 12, 2005, pp.16-20.
- [6] **L. K. Tan, R. Baumgartner and R.M. German**, Powder Injection Molding of Bi-Metal Components. PIM Compilation IV: Applications and Management Issues, Metal Powder Industries Federation, Princeton, NJ, May 2007.
- [7] **M. Braginsky, V. Tikare, E. Olevsky**, Numerical simulation of solid state sintering, *International Journal of Solids and Structures* 42 (2005) 621–636.
- [8] **D.F. Heaney, R. Spina**, Numerical analysis of debinding and sintering of MIM parts, *Journal of Materials Processing Technology* 191 (2007) 385–389.
- [9] [www.mpif.org/newsroom/facts.pdf](http://www.mpif.org/newsroom/facts.pdf)
- [10] **L. Sheppard**, The powder metallurgy industry worldwide 2007 – 2012, *Materials Technology Publications*, Sep 2007, pp. 450.
- [11] **K.P. Cooper**, Producing net-shape products by powder metallurgy, *JOM Journal of the Minerals, Metals and Materials Society*, Volume 51, Number 7, DOI: 10.1007/s11837-999 0104-9.
- [12] <http://www.azom.com/details.asp?ArticleID=1627>.
- [13] **M. Kearns**, Alloy Metal Powders for Dental Applications, 2007, Sandvik Osprey Ltd., [www.smt.sandvik.com/osprey](http://www.smt.sandvik.com/osprey).
- [14] **R.M. German**, PIM breaks the \$1 bn barrier, *Metal Powder Report*, Volume 63, Issue 3, 2008, pp. 8-10.
- [15] **P. Balaji**, Metal Injection Molding, *Advanced Materials*, Report Code: AVM049A, 2005.
- [16] **G. Schlieper**, Euro PM2009 review: A high level of MIM industry participation gives a welcome boost in Copenhagen, *Powder injection moulding international* Volume 3, Number 4, 2009, pp. 38-42.
- [17] **P. Balaji**, Metal injection molding, report code: AVM049A, July 2005.



- [18] **J. Song, T. Zhi, Y. Yu and Z. Zhuang**, Development of Molybdenum Powder Injection Moulding Feedstock, PM2010 World Congress proceeding, Volume 4, pp. 573-580.
- [19] **H. Mulin, P. Jacquet, M. Lambertin, D. Moinard-Checot and J.C. Bihr**, Contribution to the Development of 18 Carat Gold Alloy Shaped by MIM, PM2010 World Congress proceeding, Volume 4, pp. 339-346.
- [20] **D. Seo, K. Ogawa, Y. Nakao, H. Miura and T. Shoji**, Influence of high-temperature creep stress on growth of thermally grown oxide in thermal barrier coatings, Surface and Coatings Technology, Volume 203, Issue 14, 2009, pp. 1979-1983.
- [21] **R.M. German**, Divergences in global powder injection moulding, Journal of Powder Injection Moulding, Volume 2, Number 1, 2008.
- [22] [http://www.xstreamscience.org/H\\_Glaze/H\\_Glaze\\_1.htm](http://www.xstreamscience.org/H_Glaze/H_Glaze_1.htm)
- [23] **R.M. German and A. Bose**, Injection Molding of Metals and Ceramics, Princeton, New Jersey, USA, 1997.
- [24] **J. Hidalgo, J.M. Contreras, S. Gonzalez, A. Jiménez-Morales and J.M. Torralba**, Rheological Behaviour of Powder Injection Moulding (PIM) Feedstocks Fabricated with a Thermoplastic Binder System Based on Polysaccharides, PM2010 World Congress proceeding, Volume 4, pp. 549-555.
- [25] **J. Hidalgo, J.M. Contreras, B. Baile, A. Jiménez-Morales and J.M. Torralba**, Rheological and Thermal Behaviour of Powder Injection Moulding (PIM) Feedstocks Fabricated with Binder System Based on Waxes, PM2010 World Congress proceeding, Volume 4, pp. 589-594.
- [26] <http://www.custompartnet.com/wu/metal-injection-molding>
- [27] **B. Linke**, Injection molding an IC into a connector or consumable item, APP 4717, Aug 03, 2010.
- [28] **H. Jorge**, Compounding and Processing of a Water Soluble Binder for Powder Injection Moulding, Ph. D. thesis, Universidade do Minho, 2008.
- [29] **D.V. Rosato**, Injection Molding Handbook, New York (USA): Van Nostrand Reinhold (1986).
- [30] **J. Song, T. Barriere, J.C. Gelin and B. Liu**, Powder injection molding of metallic and ceramic hip implants, Int. J. Powder Metallurgy, 2009, Volume 45, Issue 3, pp. 25-34.
- [31] **Ph. Imgrund, A. Rota and L. Kramer**, Processing and properties of bi-material parts by micro metal injection moulding, Multi-Material Micro Manufacture, 2005, pp. 131.
- [32] **L.Tan and R. Baumgartner**, Powder injection molding of bi-metal components, Proceedings of European Congress and Exhibition on Powder Metallurgy Nice, France, 2001, pp. 135-140.
- [33] [http://www.fcs.com.tw/webtop/FAQ\\_EN/index.phtml?action=browse&id=164&StoreID=9&](http://www.fcs.com.tw/webtop/FAQ_EN/index.phtml?action=browse&id=164&StoreID=9&)
- [34] **R. Ruprecht, T. Gietzelt, K. Mueller, V. Piotter and J. Hausselt**, Injection molding of microstructured components from plastics, metals and ceramics, Microsystem Technologies, 2002, pp.351-358.

- [35] **Ph. Imgrund, A. Rota and A. Simchi**, Microinjection moulding of 316L/17-4PH and 316L/Fe powders for fabrication of magnetic–nonmagnetic bimetals, *Journal of Materials Processing Technology*, Volume 200, Issues 1-3, 2008, pp. 259-264.
- [36] **L. Liu, N.H. Loh, B.Y. Tay, S.B. Tor, Y. Murakoshi and R. Maeda**, Mixing and characterisation of 316L stainless steel feedstock for micro powder injection molding, *Materials Characterization*, Volume 54, Issue 3, 2005, pp. 230-238.
- [37] **L. Liu, N.H. Loh, B.Y. Tay, S.B. Tor, Y. Murakoshi and R. Maeda**, Effects of thermal debinding on surface roughness in micro powder injection molding, *Materials Letters*, Volume 61, Issue 3, February 2007, pp. 809-812.
- [38] <http://www.pim-international.com/magazine>
- [39] **F. Watari, A. Yokohama, F. Saso, M. Uo and T. Kawasaki**, Fabrication and properties of functionally graded dental implant, *Composites B: Engineering*, Volume 28, Issues 1-2, 1997, pp. 5-11.
- [40] **E.S. Thian, N.H. Loh, K.A. Khor and S.B. Tor**, Effects of debinding parameters on powder injection molded Ti-6Al-4V/HA composite parts, *Advanced Powder Technology*, Volume 12, Issue 3, 2001, pp. 361-370.
- [41] **R. Felton, P. Imgrund, F. Petzoldt, V. Friederici, D. Busquets-Mataix, L. Reig, V. Amigó and J.A. Calero**, PM companies eye a new future of taking medicine, *Metal Powder Report*, Volume 64, Issue 3, 2009, pp. 12-17.
- [42] [http://www.epma.com/New\\_non\\_members/mim\\_design.htm](http://www.epma.com/New_non_members/mim_design.htm)
- [43] **N. Williams and P. Whittaker**, PM2010 : Case studies highlight global success of Metal and Ceramic Injection Moulding, *Powder Injection Moulding International*, Volume 4, Number 4, 2010, pp. 48-54.
- [44] **C. Quinard**, Experimentation, modelisation et simulation dans le domaine de l'elaboration de micro-composants injectes a partir de poudres, Ph.D. Thesis, University of Franche-Comté 2008.
- [45] **R.M. German**, Research productivity and the value to the P.I.M. market, P.I.M. 2000, Int. Conference on Injection Moulding of Metals and Ceramics, Ed. by German R.M., Penn States University Press, 2000.
- [46] **R.M. German**, Status of PIM Research and Development, P.I.M. 2007, Int. Conference on Injection Moulding of Metals and Ceramics, Ed. by M.P.I.F, 2007.
- [47] **R.M. German**, Sintering theory and practice, Ed. by Wiley J. & Sons, 1996.
- [48] **R.M. German**, Design and applications, published by Innovation Material Solutions, 2000.
- [49] **J. Alcock**, Co-injection promises further growth for MIM, *Metal Powder Report*, Volume 54, Issue 6, 1999, pp. 1-30.
- [50] **T. Barriere**, Expérimentations, Modélisation et Simulation Numérique du Moulage par Injection de Poudres Métalliques, Thèse de doctorat, Université de Franche-Comté 2000.

- [51] **T. Hartwig, G. Veltl, F. Petzoldt, H. Kunze, R. Scholl and B. Kieback**, Powders for metal injection molding Journal of the European Ceramic Society, Volume 18, Issue 9, 1998, pp. 1211-1216.
- [52] **L. Kowalski, J. Duszczuk and L. Katgerman**, Thermal conductivity of metal powder-polymer feedstock for powder injection molding, Journal of Materials Processing Technology, Volume 178, Issues 1-3, 2006, pp. 194-199
- [53] **J.E. Bidaux, A. Jochem and E. Carreño-Morelli**, Powder injection moulding of NiTi shape memory materials, Powder Injection Moulding International, 2008, Volume 2, Issue 1, pp. 59-62.
- [54] **F.P. Petzoldt**, General introduction to metal injection moulding, Metal injection moulding, E.P.M.A. Short Course, Ed. by E.P.M.A., I.F.A.M., 1995.
- [55] **M. Reiterer, T. Kraft, U. Janosovits and H. Riedel**, Finite element simulation of cold isostatic pressing and sintering of SiC components, Ceramics International, Volume 30, Issue 2, 2004, pp. 177-183.
- [56] **T. Kraft and H. Riedel**, Numerical simulation of solid state sintering: model and application, Journal of Europe ceramic society, Volume 24, Issue 2, 2004, pp. 345-361.
- [57] **B. Zeep, P. Norajitra, V. Piotter, J. Boehm, R. Ruprecht and J. Hausselt**, Net shaping of tungsten components by micro powder injection moulding, Fusion Engineering and Design 82, Issues 15-24, 2007, pp. 2660-2665.
- [58] **H.M. Shaw and M.J. Edirisinghe**, Shrinkage and particle packing during removal of organic vehicle from ceramic injection mouldings, Journal of the European Ceramic Society, Volume 15, Issue 2, 1995, pp. 109-116.
- [59] **L. Nyborg et al.**, Interactions between surface-active additives and 316L stainless steel powder for MIM, Metal Powder Report, Volume 53, Issue 4, 1998, pp. 38.
- [60] **A. Olevsky, G. Timmermans, B. Shtern, L. Froyen and L. Delaey**, The permeable element method for modelling of deformation processes in porous and powder materials: theoretical basis and checking by experiments, Powder Technology, Volume 93, Issue 2, 1997, pp. 127-141.
- [61] **O. Van der Biest and A.L. Maximenko**, Computer modelling and optimization of thermal debinding in powder injection moulding, Metal Powder Report, Volume 53, Issue 4, 1998, pp. 39.
- [62] **B. Levenfeld, A. Várez, L. Castro and J. M. Torralba**, Processing of P/M M2 high speed steels by mould casting using thermosetting binders, Journal of Materials Processing Technology Volume 119, Issues 1-3, 2001, pp. 1-6.
- [63] **M. Matos, J. M. Castanho and M. T. Vieira**, Composite copper/stainless steel coated powders, Journal of Alloys and Compounds Volume 483, Issues 1-2, 2009, pp. 460-463.
- [64] **Z. Y. Liu, N. H. Loh, S. B. Tor, K. A. Khor, Y. Murakoshi, R. Maeda and T. Shimizu**, Micro-powder injection molding, Journal of Materials Processing Technology, Volume 127, Issue 2, 2002, pp. 165-168.

- [65] **O. Yamamoto, T. Sasamoto and M. Inagaki**, Antioxidation of carbon-carbon composites by SiC concentration gradient and zircon overcoating, *Carbon*, Volume 33, Issue 4, 1995, pp. 359-365.
- [66] **Y. Kang and S. Kang**, The surface microstructure of TiC-(Ti,W)C-WC-Ni cermets sintered in a nitrogen atmosphere, *Materials Science and Engineering: A*, Volume 527, Issues 27-28, 2010, pp. 7241-7246.
- [67] **Y. Kang and S. Kang**, WC-reinforced (Ti,W)(CN), *Journal of the European Ceramic Society*, Volume 30, Issue 3, 2010, pp. 793-798.
- [68] **H.K. Kang and S. B. Kang**, Tungsten/copper composite deposits produced by a cold spray, *Scripta Materialia*, Volume 49, Issue 12, 2003, pp. 1169-1174.
- [69] **M. Thornagel**, MIM-Simulation: A Virtual Study on Phase Separation, *EURO PM2009 Proceedings*, Volume 2, 2009, pp. 135-140.
- [70] **F. Ilinca and J.F. Héu**, A finite element immersed boundary method for fluid flow around moving objects, *Computers & Fluids*, Volume 39, Issue 9, 2010, pp. 1656-1671.
- [71] **J.F. Hetu**, Simulation of injection moulding effects of thermal and inertial effects on flow stability, *Metal Powder Report*, Volume 56, Issue 6, 2001, pp. 40.
- [72] **J. Song, J.C. Gelin, T. Barriere and B. Liu**, Experiments and numerical modelling of solid state sintering for 316L stainless steel components, *J. of Materials Processing and Technology* 177, 2006, pp. 352-355.
- [73] **A. Poitou**, Approche mécanique du mélange par extrusion, Thèse de doctorat soutenue en 1988, Ecole des Mines de Paris, 1988, pp. 1-120.
- [74] **Manguin-Fritsch Agnès**, Modélisation et optimisation de la dégradation thermique des liants utilisés en injection de céramiques, Thèse de doctorat soutenue le 01/11/1992, Ecole des Mines de Paris, 1992, pp. 1-100.
- [75] **B. Lanteri**, Etude du comportement rhéologique d'un mélange polymère-céramique destiné à l'injection, Thèse de doctorat soutenue le 01/12/1993, Ecole des Mines de Paris, 1993, pp. 1-100.
- [76] **L. Minier, S.L. Gallet, Y. Grin and F. Bernard**, Influence of the current flow on the SPS sintering of a Ni powder, *Journal of Alloys and Compounds*, Volume 508, Issue 2, 2010, pp. 412-418.
- [77] **M. Dutilly and J.C. Gelin**, A multiphase flow approach accounting for thermo-mechanical coupling for modelling the powder injection molding, *Simulation of Materials Processing: Theory, Methods and Application*, Ed. by Shen and Dawson, 1998, pp. 635-640.
- [78] **M. Dutilly, O. Ghouati and J.C. Gelin**, Finite element analysis of the debinding and densification phenomena in the process of metal injection molding, *Materials Processing Technology*, Volume 83, Issues 1-3, 1998, pp. 170-175.

- [79] **T. Barriere, J.C. Gelin and B. Liu**, Experimental and numerical investigations on the properties and quality of parts produced by MIM, Powder Metallurgy, Ed. by Maney Publishing, Volume 44, Number 3, 2001, pp. 228-234.
- [80] **D.F. Heaney, T.J. Mueller and P A. Davies**, Mechanical properties of metal injection moulded 316L stainless steel using both prealloy and master alloy techniques, Powder Metallurgy, Volume 47, Number 4, 2004, pp. 367-373.
- [81] **M.A. Omar, R. Ibrahim, M.I. Sidik, M. Mustapha and M. Mohamad**, Rapid debinding of 316L stainless steel injection moulded component, Journal of Materials Processing Technology, Volume 140, Issues 1-3, 2003, pp. 397–400.
- [82] **C. Quinard, T. Barriere and J.C. Gelin**, Development and property identification of 316L stainless steel feedstock for PIM and  $\mu$ PIM, Powder Technology, Volume 190, Issues 1-2, 2009, pp.123–128.
- [83] **M.E. Sotomayor, A. Várez and B. Levenfeld**, Influence of powder particle size distribution on rheological properties of 316 L powder injection moulding feedstocks, Powder Technology, Volume 200, Issues 1-2, 2010, pp. 30-36.
- [84] **D.F. Bailey**, Moulding Ceramic Composition, Patent No. US3285873.
- [85] **I. Hiroshi Ono, S. Katuyoshi, Y. Haruo, S. Takeo and M. Yoshimichi**, Polyamide base binder for use in metal powder injection molding process, Patent No. US5002998.
- [86] **R.W. Ohnsorg**, Composition and process for injection molding ceramic materials, Patent No. US4144207.
- [87] **R.E. Wiech**, Manufacture of parts from particulate material, Patent No. US4197118.
- [88] **K. Roetenberg, R. Raman, C. Whitman, I. Snider and R.M. German**, “Optimization of the Mixing Process for Powder Injection Molding”, Powder Injection Molding Symposium, Princeton, NJ: Metal Powder Industries Federation, 1992, pp. 119-130.
- [89] **J.H. Song and J.R.G. Evans**, Flocculation after injection moulding in ceramic suspensions. J. Mater. Res., Volume 9, Issues 9, 1994, pp. 2386-2397.
- [90] **Liu, D.-M. and W.J. Tseng**, Influence of debinding rate, solid loading and binder formulation on the green microstructure and sintering behaviour of ceramic injection mouldings. Ceramics International, Volume 24, Issues 6, 1998, pp. 471-481.
- [91] **Zhu, B., X. Qu, and Y. Tao**, Mathematical model for condensed-solvent debinding process of PIM. Journal of Materials Processing Technology, Volume 142, Issue 2, 2003, pp. 487-492.
- [92] **Honek, T., B. Hausnerova, and P. Saha**, Relative viscosity models and their application to capillary flow data of highly filled hard-metal carbide powder compounds. Polymer Composites, Volume 26, Issue 1, 2005, pp. 29-36.

- [93] **C. Karatas, A. Kocer, H. I. Ünal and S. Saritas**, Rheological properties of feedstocks prepared with steatite powder and polyethylene-based thermoplastic binders, *Journal of Materials Processing Technology*, Volume 152, Issue 1, 2004, pp. 77-83.
- [94] **J.J. Reddy, N. Ravi and M. Vijayakumar**, A simple model for viscosity of powder injection moulding mixes with binder content above powder critical binder volume concentration, *Journal of the European Ceramic Society*, Volume 20, Issue 12, 2000, pp. 2183-2190.
- [95] **M. Khakbiz, A. Simchi and R. Bagheri**, Analysis of the rheological behavior and stability of 316L stainless steel–TiC powder injection molding feedstock, *Materials Science and Engineering: A*, Volume 407, Issues 1-2, 2005, pp. 105-113.
- [96] **X. Kong, C. Quinard, T. Barrière and J. C. Gelin**, Mixing and Characterisation of stainless steel 316L feedstock, *International Journal of Material Forming*, Volume 2, Supplement 1, 2009, pp. 709-712.
- [97] **X. Kong, T. Barriere and J. C. Gelin**, Investigations on sintering of 316L stainless steel powders and identification of physical parameters from coupling experiments and finite element simulations, *International Journal of Powder Metallurgy*, May/June, 2010, pp. 61-72.
- [98] **M. Bousmina, A. Ait-Kadi and J. B. Faisant**, Determination of shear rate and viscosity from batch mixer data, *Journal of Rheology*, Volume 43, Issue 2, 1999, pp.415-433.
- [99] **Y. Li, L. Li and K.A. Khalil**, Effect of powder loading on metal injection molding stainless steels, *Journal of Materials Processing Technology*, Volume 183, Issues 2-3, 2007, pp. 432–439.
- [100] **T. Jardiel, M.E. Sotomayor, B. Levenfeld, and A. Várez**, Optimization of the Processing of 8-YSZ Powder by Powder Injection Molding for SOFC Electrolytes, *International Journal of Applied Ceramic Technology*, Volume 5, Issue 6, 2008, pp. 574 – 581.
- [101] **G. Aggarwal, S. J. Park and I. Smid**, Development of niobium powder injection molding: Part I. Feedstock and injection molding, *International Journal of Refractory Metals & Hard Materials*, Volume 24, Issue 3, 2006, pp. 253–262.
- [102] **Y. Li, B. Huang and X. Qu**, Viscosity and melt rheology of metal injection molding feedstocks, *Powder Metall.*, Volume 42, Number 1, 1999, pp.86-90.
- [103] **X. Chen, Y. C. Lam, Z. Y. Wang and K. W. Tan**, Determination of phenomenological constant of shear-induced particle migration model, *Comput. Mater. Sci.*, Volume 30, Issues 3-4, 2004, pp.223-229.
- [104] **C.I. Chung, B.O. Rhee, M.Y. Cao and C.X. Liu**, Requirements of binder for powder injection molding. *Compend Met Inject Molding*, Volume 2, 1989, pp. 67– 72.
- [105] **V. Piottter, W. Bauer, T. Benzler and A. Emde**, Injection molding of components for microsystems. *Microsyst Technol*, Volume 7, 2001, pp. 99– 102.

- [106] **H. Berthiaux, V. Mosorov, L. Tomczak, C. Gatumel and J.F. Demeyre**, Principal component analysis for characterising homogeneity in powder mixing using image processing techniques, *Chemical Engineering and Processing*, Volume 45, Issue 5, 2006, pp. 397-403.
- [107] **W. Yang, K. Yang and M.H. Hon**, Effects of PEG molecular weights on rheological behavior of alumina injection molding feedstocks, *Materials Chemistry and Physics*, Volume 78, Issue 2, 2003, pp. 416-424.
- [108] **C.G. Kukla**, Micro injection molding, *Int. J. of Forming Processes*, Volume 4, Issues 3-4, 2001, pp. 253-269.
- [109] **T. Osada, K. Nishiyabu, Y. Karasaki, S. Tanaka and H. Miura**, Investigations on the variation of feedstock properties in Micro MIM Products, Powder injection molding, Penn State College, Ed. by R.M. German, Pennsylvania, USA, 2003, pp. 1-11.
- [110] **A.C. Rota, F. Petzoldt and P. Imgrund**, Micromolding of advanced material combinations, Powder injection molding, Penn State College, Ed. by R.M. German, Pennsylvania, USA, 2003, pp. 1-18.
- [111] **D.F. Heaney, P. Suri and R.M. German**, Defect-free sintering of two material powder injection molded components, *Journal of Materials Science*, 2003, Volume 38, Number 24, pp. 4869–4874.
- [112] **T.L. Lin and L.W. Hourng**, Investigation of wick debinding in metal injection molding: numerical simulations by the random walk approach and experiments, *Advanced Powder Technology*, Volume 16, Issue 5, 2005, pp. 495-515
- [113] **S.A. Matar, M.J. Edirisinghe**, Diffusion of degradation products in ceramic moldings during pyrolysis: Effect of Geometry, J.R.G. Evans and E.H. Twizell, *Journal of the American Ceramic Society*, Volume 79, Issue 3, 1996, pp. 749-755.
- [114] **M.J. Cima, J.A. Lewis and A.D. Devoe**, Binder Distribution in Ceramic Greenware During Thermolysis, *Journal of the American Ceramic Society*, Volume 72, Issue 7, 1989, pp. 1192–1199.
- [115] **H.H. Angermann, F.K. Yang and O.V. Biest**, Removal of low molecular weight components during thermal debinding of powder compacts, *Journal of the American Ceramic Society* Volume 72, Issue 7, 1989, pp. 1192–1199.
- [116] **R.M. German**, Theory of thermal debinding, *International Journal of Powder Metallurgy* (Princeton, New Jersey), Volume 23, Issue 4, 1987, pp. 237-245.
- [117] **Y. Li, X. Qu and B. Huang**, Thermal debinding and model for the wax-based MIM binder of multi-polymer components, *Jinshu Xuebao/Acta Metallurgica Sinica*, Volume 35, Issue 2, 1999, pp. 167-171.
- [118] **Y. Li, S. Liu, X. Qu and B. Huang**, Thermal debinding processing of 316L stainless steel powder injection molding compacts, *Journal of Materials Processing Technology*, Volume 137, Issues 1-3, 2003, pp. 65-69

- [119] **E.S. Thian, N.H. Loh, K.A. Khor and S.B. Tor**, Effects of debinding parameters on powder injection molded Ti-6Al-4V/HA composite parts, *Advanced Powder Technology*, Volume 12, Issue 3, 2001, pp. 361-370.
- [120] **D.W.V. Krevelen**, *Properties of Polymers* (Third edition), 1990, Amsterdam.
- [121] **D.F. Haeney, T.J. Mueller and P.A. Davies**, Mechanical properties of metal injection moulding 316L stainless steel using both prealloy and master alloy techniques, *Powder Metallurgy*, Volume 47, Number 4, 2004, pp. 367-373(7).
- [122] **R.M. German**, *Sintering theory and practice*, 1996, J. Wiley and Sons, New York.
- [123] **J. Rawers, F. Croydon, R. Krabbe and N. Duttlinger**, Tensile characteristics of nitrogen enhanced powder injection moulded 316L stainless steel, *Powder Metall.*, Volume 39, Number 2, 1996, pp. 125.
- [124] **R.P. Koseski, P. Suri, N.B. Earhardt, R.M. German and Y.S. Kwon**, Microstructural evolution of injection molded gas- and water-atomized 316L stainless steel powder during sintering, *Materials Science and Engineering A*, Volume 390, Issues 1-2, 2005, pp. 171-177.
- [125] **C. H. Ji, N. H. Loh, K. A. Khor and S. B. Tor**, Sintering study of 316L stainless steel metal injection molding parts using Taguchi method: final density, *Materials Science and Engineering A*, Volume 311, Issues 1-2, 2001, pp. 74-82.
- [126] **L. Cai and R.M. German**, Powder Injection Molding Using Water Atomized 316L Stainless Steel, *Int. J. of Powder Metallurgy*, Volume 31, Number 3, 1995, pp. 257-264.
- [127] **N. H. Loh and R. M. German**, Statistical analysis of shrinkage variation for powder injection molding, *Journal of Materials Processing Technology*, Volume 59, Issue 3, 1996, pp. 278-284.
- [128] **T. Kraft and H. Riedel**, Numerical simulation of solid state sintering; model and application, *Journal of the European Ceramic Society*, Volume 24, Issue 2, 2004, pp. 345-361.
- [129] **G.C. Kuczynski**, Self diffusion in sintering of metallic particles. *Met. Trans.*, 185, 1949, pp. 169–178.
- [130] **A. Luque, J. Aldazabal, J.M. Martínez-Esnaola, A. Martínez-Meizoso, J. Gil Sevillano, and R.S. Farr**, Geometrical Monte Carlo model of liquid-phase sintering, *Mathematics and Computers in Simulation*, Volume 80, Issue 7, 2010, pp. 1469-1486.
- [131] **R.L. Coble**, **Sintering of crystalline solids. I. Intermediate and final state diffusion models**, *Journal of Applied Physics*, Volume 32, Issue 5, 1961, pp. 787–792.
- [132] **W.D. Kingery, and M. Berg**, Study of the initial stages of sintering of solids by viscous flow, evaporation-condensation and self-diffusion. *Journal of Applied Physics*, Volume 26, Issue 10, 1955, pp. 1205–1212.
- [133] **J.K. Mackenzie and R. Shuttleworth**, A phenomenological theory of sintering. *Proceedings of the Physical Society. Section B*, Volume 62, Number 12, 1949, pp. 833–852.



- [134] **D.L. Johnson**, New method for obtaining volume, grainboundary, and surface diffusion coefficients from sintering data. *Journal of Applied Physics*, Volume 40, Issue 1, 1969, pp. 192-200.
- [135] **V.W. Skorokhod and S. M. Solonin**, *Sov. Powder Metall. Met. Ceram.* 1972, 141.
- [136] **M.F. Ashby**, A first report on sintering diagrams, *Acta Metallurgica*, Volume 22, Issue 3, 1974, pp. 275-289.
- [137] **W. Beere**, The second stage sintering kinetics of powder compacts, *Acta Metallurgica*, Volume 23, Issue 1, 1975, pp. 139-145.
- [138] **G.W. Scherer**, **Sintering of low-density glasses**, *Journal of the American Ceramic Society*, Volume 60, Issue 5-6, 1977, pp. 236–239.
- [139] **H.E. Exner**, Principles of single phase sintering, In *Reviews on Powder Metallurgy and Physical Ceramics*, Vol. 1., Freund Publishing House, Tel Aviv, 1979.
- [140] **H.E. Exner**, Solid-state sintering: critical assessment of theoretical concepts and experimental methods. *Powder Metall. Int.*, Volume 23, Issue 4, 1980, pp. 203–209.
- [141] **H. E. Exner and E. Arzt**, Sintering processes. In *Physical Metallurgy*, 4th edn. Vol. 3, ed. R. W. Cahn and P. Haasen. Elsevier Science, Amsterdam, 1996, pp. 2628–2662.
- [142] **H.E. Exner, and T. Kraft**, Review on computer simulations of sintering processes, In: *Powder Metallurgy World Congress 1998*, Vol. 2. EPMA, Shrewsbury, UK, 1998, pp. 278–283.
- [143] **W. Schatt**, *Sintervorgange*. VDI-Verlag, Dusseldorf, 1992.
- [144] **E.A. Olevsky**, Theory of sintering: from discrete to continuum, *Materials Science and Engineering: R: Reports*, Volume 23, Issue 2, 1998, pp. 41-100.
- [145] **W.D. Kingery**, Densification during sintering in the presence of a liquid phase. I. Theory., *Journal of Applied Physics* Volume 30, Issue 3, 1959, pp. 301–306.
- [146] **R.M. German**, *Liquid Phase Sintering*. Plenum Press, New York, 1985.
- [147] **A.P. Savitskii**, *Liquid Phase Sintering of Systems with Interacting Components*. Russian Academy of Sciences, Tomsk, 1993.
- [148] **R.P. Markondeya, A. Odulena and W.R. Cannon**, Anisotropic shrinkage during sintering of particle-oriented systems numerical simulation and experimental studies, *Acta Materialia*, Volume 50, Issue 10, 2002, pp. 2559-2570.
- [149] **H. Riedel and J. Svoboda**, Simulation of microwave sintering with advanced sintering models, *Advances in Microwave and Radio Frequency Processing* 2006, Part III, 210-216, DOI: 10.1007/978-3-540-32944-2\_23.
- [150] **A. Mawardi and R. Pitchumani**, Simulation of sintering of nanoparticulate micropreforms in a microfabrication process, *Acta Materialia*, Volume 57, Issue 6, 2009, pp. 1975-1987.
- [151] **R.M. McMeeking, and L.T. Kuhn**, A diffusional creep law for powder compacts, *Acta Metallurgica Et Materialia*, Volume 40, Issue 5, 1992, pp. 961-969.

- [152] **M. Braginsky, V. Tikare and E. Olevsky**, Numerical simulation of solid state sintering, *International Journal of Solids and Structures*, Volume 42, Issue 2, 2005, pp. 621-636.
- [153] **D. Walgraef and E.C. Aifantis**, Plastic instabilities, dislocation patterns and nonequilibrium phenomena, *Res Mechanica*, Volume 23, Issue 2-3, 1988, pp. 161-195 .
- [154] **L.P. Kubin and Y. Estrin**, Evolution of dislocation densities and the critical conditions for the Portevin–Lechatelier effect, *Acta Metallurgica et Materialia*, Volume 38, Issues 5, pp. 697–708.
- [155] **G. Ananthakrishna**, Formation, propagation of bands and chaos in Jerky flow, *Scripta Metallurgica et Materialia*, Volume 29, Issue 9, 1993, pp. 1183-1188.
- [156] **M.V. Glazov and C. Laird**, Size effects of dislocation patterning in fatigued metals, *Acta Metallurgica et Materialia*, Volume 43, Issue 7, 1995, pp. 2849-2857.
- [157] **D. Lance, F. Valdivieso and P. Goeuriot**, Correlation between densification rate and microstructural evolution for pure alpha alumina, *Journal of the European Ceramic Society*, Volume 24, Issue 9, 2004, pp. 2749-2761.
- [158] **C. Nivot and F. Valdivieso**, Microstructure refinement of alumina: Optimisation by gas pressure sintering process, *Ceramics International*, Volume 34, Issue 7, 2008, pp. 1595-1602.
- [159] **M. Gasik and B. Zhang**, A constitutive model and FE simulation for the sintering process of powder compacts, *Computational Materials Science*, Volume 18, Issue 1, 2000, pp. 93-101.
- [160] **J. Song, T. Barriere, B. Liu, J.C. Gelin and G. Michel**, Experimental and numerical analysis on sintering behaviours of injection moulded components in 316L stainless steel powders, *Powder Metallurgy*, Volume 53, Number 4, pp. 295-304.
- [161] **R.L. Coble**, A model for boundary diffusion controlled creep in polycrystalline materials, *J. Appl. Phys.*, Volume 34, Number 6, 1963, pp. 1679-1682.
- [162] **R.K. Bordia and G.W. Scherer**, On constrained sintering-I Constitutive model for a sintering body, *Acta Materialia*, Volume 36, Number 9, 1988, pp. 2393-2397.
- [163] **F.R.N. Nabarro**, Creep at very Low Rates, *Metall. Mater. Trans. A.*, Volume 33A, Number 153, 2002, pp. 213-218.
- [164] **M. Dutilly, O. Ghouati and J.C. Gelin**, Finite-element analysis of the debinding and densification phenomena in the process of metal injection molding, *Journal of Materials Processing Technology*, Volume 83, Issues 1-3, 1998, pp. 170-175.
- [165] **R. Zhang and R.S. Engel**, N.J. Salamon, R.M. German, Simulation of free sintering shrinkage and distortion behavior of stainless steel powder compacts, *Proceedings of the 2002 International Conference on Process Modeling in Powder Metallurgy&Particulate Materials*, Newport Beach, CA, October 28–29, 2002.
- [166] **R.K. Bordia and G.W. Scherer**, On constrained sintering-I Constitutive model for a sintering body, *Acta Materialia*, Volume 36, Number 9, 1988, pp. 2393-2397.

- [167] **J. Song**, Experiments, Modelling and Numerical Simulation of the Sintering Process for Metallic or Ceramic Powders, Ph.D. Thesis, University of Franche-Comté and Southwest Jiaotong University, 2007.
- [168] **A. Peterson and J. Agren**, Constitutive behavior of WC-Co materials with different grain size sintered under load, *Acta Materialia*, Volume 52, Issue 7, 2004, pp. 1847-1858.
- [169] **D.C. Blaine, R. Bollina, S.J. Park and R.M. German**, Critical use of video-imaging to rationalize computer sintering simulation, *Computers in industry*, Volume 56, Number 9, 2005, pp. 867-875.
- [170] **C. Quinard, J. Song, T. Barriere and J.C. Gelin**, Elaboration of PIM feedstocks with 316L fine stainless steel powders for the processing of micro-components, *Powder Technology*, In Press, Corrected Proof, Available online 26 August 2010.
- [171] **O. Lame, D. Bouvard and H. Wiedemann**, Anisotropic shrinkage gravity induced creep during sintering of steel powder compacts, *Powder Metall.*, Volume 45, Number 2, 2002, pp. 181-185.
- [172] **A. Vagnon, D. Bouvard and G. Kapelski**, An anisotropic constitutive model for simulating the sintering of stainless steel powders compacts, *Technology & Applications of Sintering*, Proceedings of the 4th International Conference on the Science, Grenoble, France, August 29-September 1, 2005, pp. 232-235.
- [173] **J. Svoboda, H. Riedel and H. Zipse**, Equilibrium pore surfaces, sintering stresses and constitutive equations for intermediate and late stages of sintering-Part I: Computation of equilibrium surfaces, *Acta Metallurgica et Materialia*, Volume 42, Issue 2, 1994, pp. 435-443.
- [174] **H. Riedel and J. Svoboda**, Equilibrium pore surfaces, sintering stresses and constitutive equations for intermediate and late stages of sintering-Part II: Diffusional densification and creep, *Acta Metallurgica et Materialia*, Volume 42, Issue 2, 1994, pp. 445-452.
- [175] **J.C. Lagarias, J.A. Reeds, M.H. Wright and P.E. Wright**, Convergence Properties of the Nelder-Mead Simplex Method in Low Dimensions, *SIAM Journal of Optimization*, Volume 9, Number 1, 1998, pp. 112-147.
- [176] **T. Kraft and H. Riedel**, Numerical simulation of solid state sintering; model and application, *Journal of the European Ceramic Society*, Volume 24, Issue 2, 2004, pp. 345-361.
- [177] **K. Mori**, Finite element simulation of nonuniform shrinkage in sintering of ceramic powder compact, In *Numerical Methods in Industrial Forming Processes*, Numiform 92, ed. J. L. Chenot, R. D. Wood and O. C. Zienkiewicz. A.A. Balkema, Rotterdam, 1992, pp. 69 - 78.
- [178] **K.Y. Sanliturk, I. Aydin and B.J. Briscoe**, A finite-element approach for the shape prediction of ceramic compacts during sintering, *J. Am. Ceram. Soc.*, Volume 82, Issue 7, 1999, pp. 1748-1756,
- [ 179 ] **E. Doege, A. Bagaviev and K. Hanini**, FEM Simulation der Prozessschritte Pulverpressen/Sintern. *Mat.-wiss. Werkstofftech*, Volume 32, Issue 1, 2001, pp. 57-61.

- [180] **T. Kraft, H. Riedel, P. Stingl, and F. Wittig**, Finite element simulation of die pressing and sintering, *Adv. Engng. Mater.*, Volume 1, Issue 2, 1999, pp. 107 – 109.
- [181] **T. Kraft and H. Riedel**, Numerical simulation of die compaction and sintering, *Powder Metall*, Volume 45, Number 3, 2002, pp. 227-231(5).
- [182] **J.C. Gelin, T. Barriere, J. Song and B. Liu**, Experimental Investigations and Numerical Modelling of Sintering Process for 316L Stainless Steel MIM Components, International Conference on Powder Injection Molding of Metals, Ceramics and Carbides, 20-22 March 2006, Florida, USA.
- [183] **R. Zhang, R.S. Engel, N.J. Salamon and R.M. German**, Simulation of free sintering shrinkage and distortion behavior of stainless steel powder compacts, 2002 International Conference on Process Modeling in Powder Metallurgy & Particulate Materials, Oct. 28-29, 2002, Newport Beach, CA.
- [184] **E.A. Olevsky and R.M. German**, Effect of gravity on dimensional change during sintering-I shrinkage anisotropy, *Acta Mater.*, Volume 48, Issue 5, 2000, pp. 1153-1166.
- [185] **E.A. Olevsky, R.M. German and A. Upadhyaya**, Effect of gravity on dimensional change during sintering- II shape distortion, *Acta Mater.*, Volume 48, Issue 5, 2000, pp. 1167-1180.
- [186] **R.M. German**, *Powder Injection Molding*, MPIF, 1990, Princeton, NJ.